Imperial College London

GUIDED WAVE SYNTHETIC FOCUSING IMAGING IN LIMITED ACCESS PIPES FOR IMPROVED QUANTIFICATION ACCURACY

by

Filip Szlaszynski

A thesis submitted for the degree of

Doctor of Engineering

Department of Mechanical Engineering

Imperial College London

London SW7 2AZ

March 2023

This page intentionally left blank

Declaration of Originality

The content of this thesis is my own research work, which was completed with the supervision of Professor Michael Lowe and Dr Peter Huthwaite. Wherever other work was used I clearly acknowledged, and provided references.

Filip Szlaszynski

7th March 2023

This page intentionally left blank

Copyright Declaration

This page intentionally left blank

Abstract

Routine inspection of pipelines and processing and production plants is paramount for their safe and reliable operation. Detection and criticality assessment of defects appearing in inaccessible locations in pipelines poses a great challenge for many industries. Therefore, inspection methods capable of defect detection, location and accurate characterisation in these unreachable locations from a distance away are needed.

Guided wave testing is a promising non-destructive testing technique to address inspection of such inaccessible areas. The method has been extensively deployed for rapid screening of large lengths of pipes from a single device position. Because the technique is designed for large volumetric coverage it provides very limited individual feature characterisation. The areas where potential defects are indicated are typically inspected locally using more accurate methods (e.g. phased array ultrasonic testing) to confirm defect presence and perform its characterisation. The follow-up inspections of the inaccessible locations are not possible, hence defect characterisation using guided wave testing needs to be improved. The research presented in this thesis aims to improve defect detection, location and characterisation in guided wave testing by the deployment of high resolution synthetic focusing imaging.

The common source method (CSM), total focusing method (TFM) and plane wave imaging (PWI) algorithms are adapted to guided wave testing of pipes. Their performance is evaluated and compared in terms of lateral resolution and signal-to-noise ratio (SNR) using finite element (FE) and experimental studies. The study is concerned with part-circumferential part-depth planar cracks and the fundamental shear horizontal SH0 guided wave mode is considered. It is shown that PWI achieves superior resolution compared to CSM and comparable resolution to TFM. The

techniques involving plane wave acquisition (PWI and CSM) are found to substantially outperform methods based on full matrix capture (FMC) in terms of SNR. Therefore, it is concluded that PWI which achieves good resolution and high SNR is a more attractive choice for short-range pipe guided wave testing, compared to other considered techniques. It was demonstrated that it is possible to estimate crack through wall thickness depth from the indication amplitude measured from the PWI reconstructed images. Subsequently, a novel PWI transduction setup is proposed, and it is shown to suppress the transmission of the unwanted fundamental S0 mode, which further improves SNR of PWI.

It is often the case that access to the full pipe circumference is limited in pipelines with high feature density. Therefore, the influence of limited circumferential access on the performance of SH0 guided wave PWI is investigated. A decrease in circumferential extent is analytically shown to reduce the k-space data available for imaging and impair the phased array focusing performance. This is partially balanced by a temporal bandwidth of a typical probing Hann-windowed excitation which populates some of the missing parts of the k-space. The FE and experimental studies compare the performance of PWI for a range of different array circumferential extents. The key conclusions are that array circumferential extents above 60 % are required for the reliable detection, location, and length estimation of small cracks, 50 % circumferential extent only provides sufficient detection and location of cracks above a wavelength in length and array circumferential extents below 50 % are not suitable for reliable pipe inspection.

Acknowledgements

During my journey through this Engineering Doctorate program I met many fantastic people and received a great deal of support. My experience would not have been the same without all of you.

I would like to take this opportunity to thank my academic supervisors, Professor Michael Lowe and Dr Peter Huthwaite, for their guidance, mentoring, and continuous support. I appreciate your advice, dedication of time and our countless stimulating discussions. Thank you for creating many opportunities for me and for supporting this project with your knowledge and outstanding technical expertise. I will miss your kindness, friendly attitude and great sense of humour.

I would also like to thank my industrial supervisor, Dr John Jian, for his dedication of time, support, providing useful insights into industrial needs and collaboration on the direction of the research to fulfil these needs. I am very grateful for providing me with the opportunity to experience the industrial environment during my visits at EDF Energy.

This work would not be possible without the financial support from the Research Centre in Non-Destructive Evaluation (RCNDE), the Engineering and Physical Sciences Research Council (EPSRC) and EDF Energy plc., which I am very grateful for.

I owe thanks to Guided Ultrasonics Ltd. for their help in the creation of the custom transduction ring; special thanks to Dr David Alleyne, Dr Jimmy Fong and Edmar Thompson. Thanks must be also extended to Antonio De Sanctis in the NDT group at Imperial College for his advice and help with parts of the experimental setup.

The NDT group at Imperial College London has been a truly enjoyable, friendly and

stimulating environment to work in. I am grateful to all past and present members who all contributed to the creation of such a fantastic atmosphere. It was a great pleasure to socialise with you during socials at Eastside, many courses and conferences, Christmas and Viva dinners and many other events. Special thanks to Georgios Sarris, Andreas Zimmermann, Chien An Chua, Jaime Parra Raad, Michał Kalkowski, Ming Huang, Gabor Gubicza, Wei Yi Yeoh, Mikołaj Mroszczak, Arnau Garriga Casanovas, Edmund Jones, Jerome Combaniere, Stefano Mariani, Paweł Waszczuk, Sebastian Eckel, Euan Rodgers, Pouyan Khalili, Antonio De Sanctis, Sebastian Heinlein, Joe Corcoran, Bo Lan, Yasel I Quintero Lares, George West, Yiannis Simillides, Yifeng Zhang, David Shepherd and Xiaotang Gu.

Ten doktorat dedykuję moim Rodzicom w podzięce za ich nieustające i bezgraniczne wsparcie we wszystkich aspektach życia. Dziękuję Wam za zaszczepienie we mnie ciekawości świata i umożliwienie jego odkrywania. Bez Was ten doktorat by nie powstał. Ogromne podziękowania należą się również mojej Siostrze. Dziękuje Ci, że zawsze mogę na Ciebie liczyć.

Finally, I am forever indebted to my wife Sarah for her encouragement, patience, support and unconditional love. Thank you for always being there for me.

Thank you to all and each of you!

Contents

This page intentionally left blank

Table of Figures

This page intentionally left blank

List of Tables

This page intentionally left blank

Acronyms

AGR – advanced gas-cooled reactor

ALID – absorbing layers by increasing damping

An – n^{th} order antisymmetric Lamb wave mode

ASTM – American Society for Testing and Materials

CNC – computer numerical control

CSA – cross-sectional area

CSM – common source method

EMAT – electromagnetic acoustic transducer

EngD – Engineering Doctorate

F(m,n) – flexural pipe guided wave mode of m^{th} circumferential order and n^{th} consecutive order

FE – finite element

FEM – finite element method

FMC – full matrix capture

FMCPWI – plane wave imaging with time traces synthetized from the full matrix capture data

FWHM – full width at half maximum

GWT – guided wave testing

HTHA – high temperature hydrogen attack

L(0,n) – axisymmetric longitudinal pipe guided wave mode of n^{th} consecutive order

MCX – micro coaxial connector

NDT – non-destructive testing

PMLs – perfectly matched layers

PSF – point-spread-function

PWI – plane wave imaging

RMS – root mean square

ROI – region of interest

SAE – Society of Automotive Engineers

SAFT – synthetic aperture focusing technique

SH – horizontal shear wave

SHn – n^{th} order shear horizontal guided wave mode

SLS – selective laser sintering

Sn – n^{th} order symmetric Lamb wave mode

SNR – signal-to-noise ratio

SPL – spatial pulse length

SRM – stiffness reduction method

SV – vertical shear wave

T(0,n) – axisymmetric torsional pipe guided wave mode of n^{th} consecutive order

TFM – total focusing method

1. Introduction

This chapter provides a background necessary for understanding the context of the work presented in this thesis and delivers the general review of the subject area. Section 1.1 discusses the industrial motivation of the project and explains the interest in guided wave testing and synthetic focusing imaging. Section 1.2 outlines the concept of the synthetic focusing imaging and briefly discusses the most popular imaging methods. This is followed up by a review of the relevant work in adaptation of synthetic focusing imaging to plate and pipe guided wave testing in sections 1.3 and 1.4 respectively. Section 1.5 outlines the main aims and objectives of this Engineering Doctorate project. The chapter finishes with a brief outline of the thesis structure in section 1.6.

The parts of this chapter have been adapted and extracted from publication [P1] and the 12-month Engineering Doctorate progress report submitted by the author as Early Stage Assessment (ESA) with accordance to requirements for Engineering Doctorate (EngD) at Imperial College London. The 12-month progress report has not been published in the public domain.

1.1. Motivation and research background

There are millions of kilometres of pipelines around the world [2]. There are hundreds of thousands more to enter service in the next decade, as the pipe construction market is forecasted to grow from $45 billion in 2021 to $73 billion in 2031 [3]. The majority of the existing pipelines are older than three decades and the age of some of them exceeds 50 years [4,5]. A significant proportion of these pipes carry hazardous liquids and gases, especially in petrochemical, mining, and nuclear power generation industries. Potential leaks, spills and catastrophic pipe bursts can result in loss of life, serious devastation of the natural environment, prolonged production downtimes,

damage to other structures and prohibitive economic repercussions. Hence, the integrity of these vital pipelines is of a critical importance.

Pipes can develop cracks during their intended lifetime while operating in normal design conditions, despite utilization of engineering safety factors. Crack development can be onset by the presence of stress concentrators [6-8]. These include dents, scratches, gouges, and other mechanical damage caused by environmental loads, external forces or third party interference. The stress concentration can also be caused by overlooked fabrication and installation defects (e.g. weld defects). The presence of stress concentration and wall thinning, associated with defects or damage, degrades the fatigue lifetime and reduces burst strength [9]. This ultimately leads to accelerated development of fatigue cracks under cyclic loading (e.g. due to temperature and pressure changes) and in extreme cases cracking due to regular operating pressure exceeding lowered burst strength [7].

Cracking is not limited to pipes with initial damage or defects. Pipelines operating in corrosive or chemically active environments are prone to stress corrosion cracking when subject to static stress [10,11]. A similar process called irradiation-assisted stress corrosion cracking can occur in the presence of elevated radiation in nuclear reactors [12]. Prolonged exposure of carbon steel alloys to high temperature and pressure leads to high temperature hydrogen attack (HTHA) which causes fissures and cracking [13-15]. These, and many more mechanisms cause the prevalence of cracks in pipes. Therefore, routine pipeline inspections are paramount for their safe and reliable operation in compliance with modern health and safety regulations.

While inspection of straight, easily accessible pipes with modern non-destructive testing (NDT) techniques is well-established [16-18], inspection of inaccessible locations in pipelines and other critical tubular structures presents a great challenge for many industries. Most of the existing plants and pipelines were not designed with frequent

NDT inspections in mind. Plants in chemical, process, power generation and oil and gas sectors typically contain kilometres of closely laid pipes with high density of features such as tees, bends, valves etc. Such a dense piping layout limits access to each individual pipe and as a consequence, hard to reach and hence hard to inspect structures are common on many industrial sites. Further examples of inaccessible locations include pipes that are embedded, built-in, buried or contained within the protective enclosures of hazardous environments (e.g. high ionising radiation or toxic chemicals). Inspection of all these pipes with the current state of the art NDT techniques is difficult, time consuming and expensive. It often requires the dismantling of structures which leads to prolonged downtimes and risk of complications. Therefore, an NDT technique which allows for remote defect detection, location and accurate characterisation from a distance away is needed to address inspections of tubular structures to which there is only a limited access. Research presented in this thesis is concerned with development of such a technique. Two limited access inspection scenarios are considered; one with access to the full pipe circumference and the second scenario with only partial circumferential access.

The main motivation for this project comes from EDF Energy plc., the industrial partner of this project. EDF has particular interest in inspection of some key tubular components of the United Kingdom's advanced gas-cooled reactor (AGR) nuclear power plants [19]. These critical components extend into the restricted high radiation zone of the reactor but can be partially accessed from the zones with low levels of radiation. Deployment of existing NDT techniques inside the enclosed high radiation environment is very challenging, disruptive, and it carries some inherent risks. Therefore, development of an NDT technique capable of inspection of such structures from a distance away would benefit the company and would bring a substantial reduction of their nuclear assets inspection costs.

Figure 1.1: A snapshot of pipe GWT inspection of industrial pipelines. [1]

Guided wave testing (GWT) is a promising candidate for the inspection of inaccessible tubular structures. This relatively new NDT method is commercially used for long range screening of pipelines [1,20,21]. A snapshot of examination of industrial pipework using GWT is presented in Figure 1.1. GWT inspection typically covers tens of metres of pipes from a single device position, depending on pipe condition, its layout and presence of pipe features (i.e. infrequent welds, tees, bends etc.) [20]. The information about a defect obtained from GWT inspection can give some indication of severity, since, in the simplest sense, a larger defect will cause a larger reflection amplitude [22,23]. However, for defect circumferential extents smaller than $10 - 15$ %, it is difficult to distinguish a defect which is narrow and deep from that which is wider and shallow [24]. This makes it challenging to assess whether the defect is critical or not [25]. The desired large volumetric coverage of GWT comes at the price of decreased sensitivity and very limited individual defect characterisation capabilities. Therefore, follow-up inspections on areas where potential defects are indicated are usually carried out locally using more quantitative methods e.g. phased array ultrasonic testing [24]. As discussed earlier, inspections of inaccessible locations with localised NDT techniques are

troublesome, hence they are not desired in such inspection settings. GWT with improved defect characterisation would be an attractive technique for stand-alone inspection of hard-to-reach structures. There is a great potential for achieving that by deployment of high resolution synthetic focusing imaging to pipe GWT.

1.2. Synthetic focusing imaging methods

In bulk wave ultrasonic testing, defect detection, location and individual characterisation is often based on phased array synthetic focusing imaging [26-30]. Synthetic focusing algorithms reconstruct the region of interest (ROI) in post processing, applying focusing on every point (pixel) in the image using previously acquired ultrasonic data. The focusing is achieved by synthetic application of delay laws and linear superposition to the recorded ultrasonic waves which mimics the physical focusing using a transducer phased array. The main advantage of performing focusing post-acquisition is the significant reduction of inspection time, since data acquisition is only performed once to produce a fully focused image. Thanks to recent advances in computing processing power, in some phased array imaging setups, acquisition and reconstruction processes can be repeated multiple times per second allowing quasi real time imaging during inspection [31-33]. The obtained fully focused image is essentially a reflectivity map of the ROI. In continuous, homogeneous material there are no ultrasonic reflections. In principle, indications in the reconstructed image reveal the presences of material discontinuities which are either known features of the object or undesired defects. The reconstruction provides a location for the detected discontinuity and often allows for an estimate of its size, provided the size is larger than the resolution [34,35].

In recent years, the three most popular high resolution synthetic focusing imaging algorithms are synthetic aperture focusing technique (SAFT) [26,36,37], total focusing

method (TFM) [26,38,39] and plane wave imaging (PWI) [40-42]. Their corresponding transmit-receive element configurations are outlined in Figure 1.2.

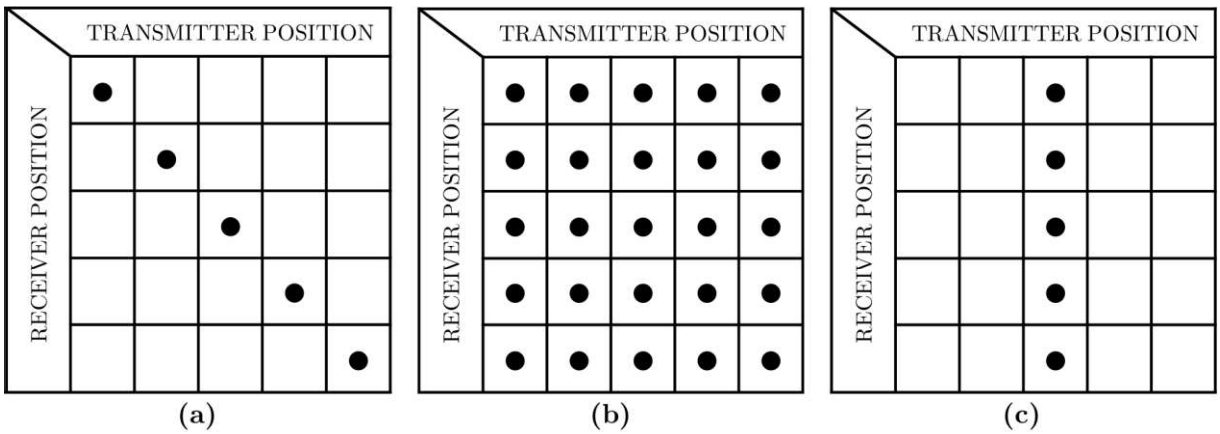

Figure 1.2: Transmit-receive element configuration matrices for (a) SAFT, (b) TFM, and (c) PWI imaging algorithms. A mark indicates transmitter-receiver pairs for which time traces are recorded.

In SAFT the source position is the same as the receiver position for each acquisition event. The technique reconstructs the image from the pulse-echo data collected from each array element in turn. It performs synthetic focusing on transmission and reception achieving high spatial resolution.

A TFM image is reconstructed from a full matrix of time domain signals (A-scans) recorded for every possible transmitter-receiver phased array element pair called full matrix capture (FMC). By focusing both on transmission and reception for each pixel of the image, good reconstruction quality and high spatial resolution are achieved. The performance advantages of TFM come at the price of acquisition time and a large amount of data to process – the technique requires N transmission-reception cycles, during each of which N time domain signals are collected, where N is the number of elements in the array.

Lately, plane wave imaging (PWI) has been the subject of increasing research interest in NDT [41-45]. The concept was first introduced in the medical field [46-48] and then improved and adapted to the field of NDT [41,42]. The technique reconstructs the region of interest from signals backscattered after insonification of the inspected area with

the plane waves sent at a chosen range of angles using all array elements. The final compounded image is obtained by coherent addition of the images reconstructed by applying focusing on reception for each plane wave angle. Le Jeune, et al. (2016) [41] and Velichko & Croxford (2018) [49] have shown that TFM and PWI methods produce images of comparable resolution and quality, with fewer transmission-reception cycles required for PWI. Fewer transmissions means shorter acquisition time and less data to process. Hence, PWI is a very attractive method for fast and accurate high resolution imaging. Excitation of the probing plane wave using all the array elements per each emission provides much higher acoustic power compared to SAFT and TFM. Consequently, the inspection range in attenuating materials is better, and the method is less sensitive to incoherent noise, assuming no averaging or other incoherent noise mitigation method is used [41]. Additionally, contrary to TFM, the number of transmission-reception cycles does not depend on the number of elements in the array. In fact, the increase in the number of array elements and consequent wider aperture results in the decrease in the number of transmission-reception cycles required to obtain the optimal image resolution which makes PWI particularly attractive for large phased arrays [49].

The Common Source Method (CSM) [26] is a special case of PWI with only a single 0° plane wave used for reconstruction. In CSM the ROI is illuminated from a single angle and focusing is performed only on reception hence its resolution is inferior to TFM and standard PWI which illuminates the ROI with a wide range of plane wave angles.

1.3. Synthetic focusing imaging in plate guided wave testing

The concept of synthetic focusing imaging can be applied to GWT. The first adaptations of imaging methods to reconstruct defects in plates from backscattered

Lamb waves were proposed in [50-52]. Davies, et al. (2006) [53] implemented CSM, SAFT and TFM to GWT of plates. The numerical and experimental study reviewed and compared the performance of these techniques in terms of point-spread-function (PSF) and Sparrow separation, the two popular criteria used for evaluation of imaging systems resolution. The PSF [54,55] is a spatial impulse response of the imaging system, hence it corresponds to an indication of the infinitesimal point scatterer in the reconstructed image. The Sparrow separation [56] is the minimum distance between the two point scatterers at which they can be distinguished from one another. Both the PSF and the Sparrow separation were of interest because the former is a major factor determining the resolution of an imaging system, whereas the latter measures the distance at which two neighbouring PSFs can be resolved (i.e., distinguished), essentially directly measuring the resolution. The research concluded that SAFT has the narrowest PSF and the smallest Sparrow separation, followed closely by TFM. CSM's PSF was shown to be double compared to SAFT which implies substantially inferior resolution. TFM was found to have significantly lower side lobe amplitude compared to the other two methods, producing much cleaner images with less coherent noise. Because TFM receives on all array elements per each acquisition, in contrast to only one receiver in SAFT, it has inherent redundancy in recorded data [26]. This redundancy has a similar effect to averaging and hence results in significantly better incoherent signal-to-noise ratio (SNR) of TFM. Moreover, TFM insonifies the ROI from a range of different angles and receives the backscattered waves on all the array elements after each transmission, with each array element in a different lateral position. In general, the wider the range of insonification and reception angles, the more spatial frequencies can be retrieved through the imaging process, provided the angular, temporal, and spatial samplings are sufficient. Therefore, TFM retrieves more spatial frequencies compared to SAFT and CSM. In SAFT, only one element records the backscattered waves after each transmission, while CSM only insonifies the ROI from

a single 0° angle. In theory, a wider spatial frequency range acquired through TFM means that this method should reproduce the ROI more accurately. However, in practice, when real life excitation with finite bandwidth is used, SAFT and TFM record a comparable range of spatial frequencies leading to similar resolution [26]. Comparable or marginally better SAFT resolution comes at the price of inferior coherent (due to side lobes [53]) and incoherent noise in reconstructed images. SNR is a key factor influencing detectability of small defects. In some cases, poor SNR can lead to insensitivity to defects that are larger than resolution limit, therefore SNR is as equally important as resolution.

In [57], SAFT was reported to only perform well in reconstructing the region directly ahead of the array aperture, its performance beyond the array aperture drastically decreases compared to TFM, which would be problematic for limited circumferential access applications considered in this project.

Taking into account all the above facts, TFM was deemed a more attractive option for guided wave imaging [53,58], compared to SAFT, and hence SAFT will not be considered in this thesis.

1.4. Synthetic focusing imaging in pipe guided wave testing

Synthetic focusing was first introduced to pipe GWT by Hayashi et al. (2005)[59]. Subsequently, the performance of CSM, SAFT and TFM was evaluated and compared for short range pipe guided wave imaging applications [25,58,60,61]. SAFT and TFM were expected to outperform CSM in terms of reconstructed image quality, however, images of both of these methods were corrupted with coherent noise bands due to the S0 mode which is excited simultaneously with the desired fundamental shear horizontal SH0 mode. The S0 mode is generated by the transducers when they are excited in the

circumferential direction to produce the SH0 mode. The unwanted S0 mode travels circumferentially and is received by the other transducers around the circumference, and these receptions are treated by the imaging algorithms as if they were SH0 reflections from features, resulting in strong artefacts, as described in [60]. Consequently, CSM was deemed the most suitable for pipe GWT applications due to its excitation of a pure torsional T(0,1) mode. Its performance was evaluated in [25] and these results will be used in this thesis for cross validation.

Despite the great potential for GWT, both SAFT and TFM suffer from coherent noise issues which significantly decrease their SNR. Furthermore, both techniques use a single insonifying element per acquisition resulting in a probing wave of low acoustic power, hence reducing the effective inspection range in real-world applications, where high attenuation is often a problem. While CSM provides superior coherent SNR and higher acoustic power, its maximum achievable resolution is significantly lower than TFM due to focusing performed only on reception. Consequently, it provides inferior defect characterisation compared to TFM which hinders limited access applications. Therefore, a technique capable of achieving high resolution while maintaining good SNR is needed.

Adaptation of PWI to pipe GWT has a potential to address the current limitations of guided wave synthetic focusing imaging mentioned above. PWI combines high resolution, comparable to TFM, with good SNR and high acoustic power. Therefore, the research presented in this thesis has particular interest in adaptation of PWI to pipe GWT.

1.5. Aims

The main objective of this Engineering Doctorate (EngD) is to improve defect detection, location and characterisation (i.e. size and maximum depth) using GWT to

allow for more quantitative and reliable inspection of inaccessible steel tubular structures from a single device position. The main focus here is adaptation of high resolution synthetic focusing imaging methods such as TFM and PWI to pipe GWT, evaluation of their performance and comparison to CSM, which is the current state-of-the-art technique. The influence of limiting array circumferential extent on imaging capabilities will also be investigated to address inspection scenarios where there is only partial circumferential access.

1.6. Thesis outline

This thesis is structured as follows.

Chapter 2 outlines basics of elastic wave propagation in solids with the main focus on guided wave theory. This chapter discusses implementation of pipe guided waves to NDT and briefly summarises the current GWT capabilities.

In Chapter 3 two dimensional CSM, TFM, PWI and FMCPWI (PWI with time traces synthetized from FMC data) algorithms are revised and their adaptation to pipe GWT is presented. The spatial Fourier domain filter removing undesired coherent noise from the FMC data is proposed to improve coherent SNR of FMC based methods. The chapter discusses the spatial resolution of the reconstruction algorithms and its limitations. A novel transduction set-up is proposed for deployment of guided wave PWI in pipes. It achieves suppression of the unwanted fundamental S0 mode hence it improves coherent SNR.

Chapter 4 introduces the methodology used for the lateral resolution and SNR measurements from the reconstructed images and describes the FE model and experimental setup used in this EngD project. Then, the selection of optimal imaging parameters for the best image quality and fair comparison of imaging methods is discussed. Subsequently, the performance of imaging methods in terms of lateral defect

sizing and SNR is evaluated and compared. This is followed by the investigation of crack through wall thickness depth estimation using PWI. Next, the performance of the transduction setup suppressing the unwanted S0 mode is evaluated. Finally, a discussion on generalisation of the presented results for different axial positions of a crack, different frequencies and pipe diameters is conducted.

Synthetic focusing imaging with limited circumferential array is discussed in Chapter 5. The theoretical discussion is followed by FE and experimental studies. The performance of PWI with a range of array circumferential extents is evaluated in terms of resolution and SNR.

Chapter 6 summarises the key findings and contributions of the thesis and discusses the potential for future work.

2. Theoretical background

2.1. Introduction

Guided waves are the result of the bulk wave interactions occurring at the interface between the two different media. Therefore, for sake of completeness, a short introduction to elastic bulk wave theory is given in this chapter. This is followed by the outline of guided wave theory. The second part of this chapter discusses the concept of NDT using guided waves and outlines the current state of the art in the field of GWT. The chapter provides merely enough background needed to attain the objectives of this thesis. The bulk wave and guided wave theory has been studied in greater depths in numerous textbooks (e.g. [62-66]); please refer to these for more in-depth treatment of the subject. The following theory is valid for linearly elastic, homogenous, isotropic solid material. The extension of the theory to anisotropic materials can be readily found in textbooks including [65].

Parts of this chapter have been adapted and extracted from the 12-month Engineering Doctorate progress report submitted by the author as Early Stage Assessment (ESA) in accordance with requirements for the Engineering Doctorate (EngD) at Imperial College London. The report has not been published in the public domain.

2.2. Bulk wave equations of motion

Elasticity is a property of solids that allow restoration of their original shape and volume after the external forces causing deformation are removed [63]. The elastic waves are time-varying deformations (vibrations) propagating in an elastic medium as a result of applied forces associated with volume deformation (compression or tension) and shape deformation (shear) of the material [62,67]. The motion of these disturbances

in the isotropic, homogeneous, linearly elastic medium in the absence of the body forces and away from the medium boundaries can be described by the equation (2.1) derived by Navier (1821) [68] from generalised Hooke's law and Newton's second law:

$$(\lambda + \mu)\nabla\nabla \cdot \boldsymbol{u} + \mu\nabla^2\boldsymbol{u} = \rho\frac{\partial^2\boldsymbol{u}}{\partial t^2}, \tag{2.1}$$

where λ and μ are two elastic constants known as Lamé constants, $\boldsymbol{u}$ is three dimensional displacement vector ($\boldsymbol{u} = (u_x, u_y, u_z)$), ρ is material density, ∇ is the vector differential operator ($\nabla = \boldsymbol{i}\frac{\partial}{\partial x} + \boldsymbol{j}\frac{\partial}{\partial y} + \boldsymbol{k}\frac{\partial}{\partial z}$), with i, j, k as unit vectors in x, y and z directions respectively and ∇^2 is the three dimensional Laplace operator ($\nabla^2 = \frac{\partial^2}{\partial x^2} + \frac{\partial^2}{\partial y^2} + \frac{\partial^2}{\partial z^2}$). The Lamé constants are related to the readily measurable quantities – the modulus of elasticity E, and the Poisson's ratio ν, via the following relationships [69]:

$$E = \frac{\mu(3\lambda+2\mu)}{\lambda+\mu} \quad \text{and} \tag{2.2}$$

$$\nu = \frac{\lambda}{2(\lambda+\mu)}. \tag{2.3}$$

To unveil the types of waves propagating in the bulk of the material (i.e. away from the boundaries) one has to find the solution(s) of equation (2.1). It is a partial differential equation that cannot be directly integrated, therefore an appropriate application-dependent solutions must be presumed.

According to the Helmholtz Decomposition Theorem [70] any vector field can be decomposed into the sum of rotational and irrotational components. Hence, displacement $\boldsymbol{u}$ can be written as follows [71]:

$$\boldsymbol{u} = \nabla\Phi + \nabla \times \boldsymbol{\psi}, \tag{2.4}$$

where Φ is a scalar potential (also known as compression wave potential), and $\boldsymbol{\psi}$ is vector potential (often called shear wave potential) with $\nabla \cdot \boldsymbol{\psi} = 0$ known as zero divergence (sometimes referred to as gauge condition) [72]. By substituting (2.4) into

Navier's equation of motion (2.1) and using the following identities $\nabla \cdot \nabla \Phi = \nabla^2 \Phi$, $\nabla \times \nabla \times \nabla \Phi = 0$ and $\nabla \cdot \nabla \times \boldsymbol{\psi} = 0$ the equation (2.5) is obtained [65]:

$$\nabla \left[(\lambda + 2\mu) \nabla^2 \Phi - \rho \frac{\partial^2 \Phi}{\partial t^2} \right] + \nabla \times \left[\mu \nabla^2 \psi - \frac{\partial^2 \boldsymbol{\psi}}{\partial t^2} \right] = 0 \tag{2.5}$$

which is satisfied when both terms in the square brackets are zero. This leads to Helmholtz differential equations:

$$\nabla^2 \Phi = \frac{1}{c_L^2} \frac{\partial^2 \Phi}{\partial t^2} \text{ and} \tag{2.6}$$

$$\nabla^2 \boldsymbol{\psi} = \frac{1}{c_T^2} \frac{\partial^2 \boldsymbol{\psi}}{\partial t^2}, \text{ where} \tag{2.7}$$

$$c_L^2 = \frac{\lambda + 2\mu}{\rho} \text{ and } c_T^2 = \frac{\mu}{\rho} \tag{2.8}$$

are velocities of longitudinal (also known as compressional or P) waves and shear (also referred to as transverse or S) waves respectively.

Consequently, the two independent general solutions for the propagation of the waves governed by equation (2.1) in the z-direction are expressed by:

$$\Phi = \Phi_0 e^{i(k_L z - \omega t)} \text{ and} \tag{2.9}$$

$$\boldsymbol{\psi} = \psi_0 e^{i(k_T z - \omega t)}, \tag{2.10}$$

where Φ_0 and ψ_0 are the initial wave amplitudes, i is the imaginary unit ($i = \sqrt{-1}$), ω is the angular frequency ($\omega = 2\pi f$), f is temporal frequency and k_L and k_T are the wavenumbers of longitudinal and shear waves respectively ($k_L = \frac{\omega}{c_L}$ and $k_T = \frac{\omega}{c_T}$), t is the time variable and z is the spatial coordinate in the direction of propagation of the wave.

The above derivation reveals that there are only two types of elastic waves propagating in an unbounded, isotropic, elastic, three-dimensional, solid medium. These waves are known as bulk waves. The particle motion of longitudinal bulk waves is in the direction

of the wave propagation, and of the shear bulk waves is in the direction perpendicular to the wave propagation [73]. Transverse motion of shear bulk waves can occur horizontally (horizontal shear wave, SH) and vertically (vertical shear wave, SV) [67]. The ratio of velocities of longitudinal and transversal waves depends on the Poisson's ratio of the material [74]. The total wave field is the superposition of longitudinal and shear waves propagating in all directions at all frequencies.

2.3. Plate guided waves

Guided waves are waves which are guided by the structure (waveguide) or sometimes the layer in which they propagate. Energy of these waves is trapped between the material boundaries [72]. Guided waves are the result of the interactions occurring at the interface between two different media. These interactions produce reflections, refractions and mode conversions between longitudinal and shear waves. Superposition of incident, reflected and mode converted partial waves leads to the emergence of guided waves. The structure through which guided waves are propagating is called a waveguide. In the literature, different shapes of waveguides have been discussed [62,64-66,72].

A plate can act as a waveguide, provided it is not too thick in relation to the wavelength. For example, Viktorov [75] suggests a practical upper limit for the plate thickness of 5 wavelengths. Plate guided wave theory is important in the context of guided waves in pipes which are the main focus in this thesis. Pipe can be considered as a plate wrapped into a cylinder, and hence plate guided wave analysis is often used to simplify the analysis of more complex pipe guided waves [25,58,76,77]. The plate-pipe analogy and its validity will be discussed in greater detail in section 2.4.4; here, plate guided wave theory is briefly outlined.

Plate guided wave theory is based on consideration of an infinite free plate problem.

It is rather a theoretical concept, than physically-realisable structure, however it serves as a good approximation for most of real-life plate-like structures [66].

The main difference between the bulk waves and plate guided waves is that the first ones propagate in the bulk of the material, away from the boundaries and the latter ones propagate between the boundaries. Despite this difference, the two types of waves are governed by the same set of Helmholtz differential equations (2.6) and (2.7). In the case of bulk waves, there are no boundary conditions that need to be satisfied by the proposed solution, whereas the solution to a guided wave problem must satisfy the governing equations as well as the boundary conditions [65]. In the case of the free plate problem, boundary conditions are traction free surfaces i.e. there is no stress present on the surfaces.

Different approaches can be used to find the solutions to the free plate problem, among which the most popular ones are displacement potential method (presented in [64]) and the partial wave technique (outlined in [66]). The former one is outlined below, because it is conceptually simpler and more elegant, however it has to be noted that its validity is limited to only isotropic material [65].

2.3.1 Lamb waves

Lamb waves [78] are one family of solutions to the free plate problem. Vertically polarized shear waves (SV) and longitudinal waves do not exist individually in the free plate but are coupled at a free boundary to cancel out stresses, ensuring that the traction-free conditions on both surfaces are fulfilled [66]. Consequently, both longitudinal and SV waves have equal wave vector components, $k_{zL} = k_{zT}$, in the z-direction along the plate, and therefore, both waves have the same velocity component in the z-direction. The result of the superposition of the longitudinal and SV partial waves is a Lamb wave mode, which is a traveling wave along the z-direction of the

plate and a resonant standing wave in the transverse y-direction.

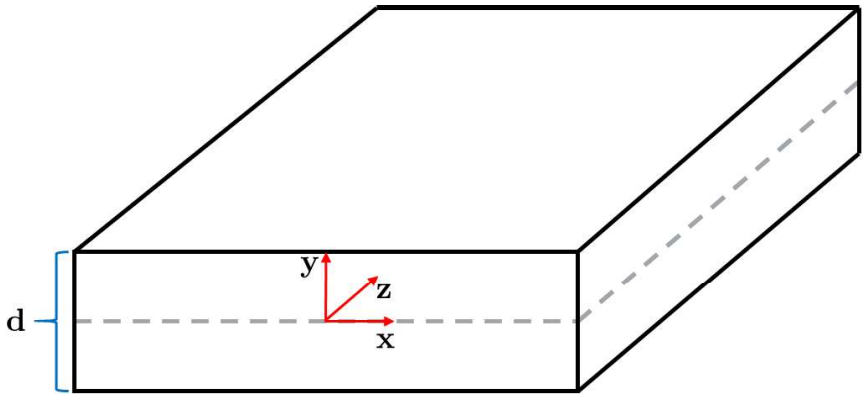

Figure 2.1: Schematic outline of a free plate problem.

A schematic of a plate in a Cartesian coordinate system is presented in Figure 2.1. The plate is infinite in x- and z-directions and plate free surfaces are at $y = -d/2$ and $y = d/2$. Let us consider a plane wave propagating in the z-direction. The problem can be simplified assuming a plain strain condition [65]. Consequently, particle displacement in the x-direction is assumed zero ($u_x = 0$), implying $\frac{\partial}{\partial x} = 0$ and the rotation only occurs about the x-axis, implying $\psi_y = \psi_z = 0$. Applying the above assumptions, to equations (2.6) and (2.7), they reduce to:

$$\frac{\partial^2 \Phi}{\partial y^2} + \frac{\partial^2 \Phi}{\partial z^2} = \frac{1}{c_L^2}\frac{\partial^2 \Phi}{\partial t^2} \quad \text{and} \tag{2.11}$$

$$\frac{\partial^2 \boldsymbol{\psi}}{\partial y^2} + \frac{\partial^2 \boldsymbol{\psi}}{\partial z^2} = \frac{1}{c_T^2}\frac{\partial^2 \boldsymbol{\psi}}{\partial t^2} \; . \tag{2.12}$$

Equations (2.11) and (2.12) govern the propagation of Lamb waves in plates. These waves exist as an infinite number of symmetrical (sometimes referred to as compressional) and asymmetrical (sometimes called flexural) modes. This classification depends on the distribution of displacements on the top and bottom bounding surfaces with respect to the mid surface ($y = 0$) [67]. For symmetric modes, the displacements on the top and bottom surfaces are symmetric and for antisymmetric modes they are antisymmetric.

From equations (2.11) and (2.12) the characteristic equations, known as Rayleigh-

Lamb frequency equations, can be derived by applying the traction free boundary conditions as shown for example in [65] or [79]:

$$\frac{\tan\left(k_{yT}\frac{d}{2}\right)}{\tan\left(k_{yL}\frac{d}{2}\right)} = -\frac{4k_z^2 k_{yT}^2 k_{yL}}{\left(k_{yT}^2 - k_z^2\right)^2} \text{ for symmetric modes, and} \tag{2.13}$$

$$\frac{\tan\left(k_{yT}\frac{d}{2}\right)}{\tan\left(k_{yL}\frac{d}{2}\right)} = -\frac{\left(k_{yT}^2 - k_z^2\right)^2}{4k_z^2 k_{yT}^2 k_{yL}} \text{ for antisymmetric modes,} \tag{2.14}$$

where k_{yL} and k_{yT} are the magnitudes of the transverse (in the y-direction) wave vector components for the longitudinal and shear partial waves, d is the plate thickness, and k_z is the wave number in the propagation direction [66]. The wavenumber k_z can be expressed as:

$$k_z = \frac{\omega}{c_p}, \tag{2.15}$$

where c_p is the phase velocity of the Lamb wave mode and ω is the angular frequency. The transverse wave components are related to ω, and the z-direction wavenumber via [79]:

$$k_{yL}^2 = k_L^2 - k_z^2 = \left(\frac{\omega}{c_L}\right)^2 - k_z^2 \text{ and} \tag{2.16}$$

$$k_{yT}^2 = k_T^2 - k_z^2 = \left(\frac{\omega}{c_T}\right)^2 - k_z^2. \tag{2.17}$$

By substituting equations (2.16) and (2.17) into (2.13) and (2.14) the equations relating the Lamb wave number to frequency and plate thickness d can be derived. For any given frequency ω and plate thickness d, there is an infinite number of wavenumbers that will satisfy the Rayleigh-Lamb frequency equations [65]. A finite number of these wavenumbers will be real or purely imaginary, whereas infinitely many will be complex. Only the real wavenumbers correspond to modes propagating in a free plate [66,67]. The Rayleigh-Lamb frequency equations are transcendental, and they can only be solved numerically [63], using for example the procedure outlined in [65,67] or the DISPERSE software developed at Imperial College London [80].

The Lamb wave phase velocity can be readily calculated from the wave number using relationship (2.15). The real solutions to Rayleigh-Lamb frequency equations are typically plotted in the two-dimensional plot of wave velocity against frequency or more commonly frequency-thickness product. They appear in the plot as curves which are called dispersion curves.

Dispersion is the dependence of phase velocity, on the temporal frequency of the propagating waves [67]. The dispersion phenomenon manifests as distortion of the wavepacket shape as it propagates through the material. The wavepacket elongates and its maximum amplitude decreases as its 'faster' frequency components propagate ahead of the 'slower' ones. Dispersion is discussed in greater detail, for example, in [65].

Dispersion is generally not desired in guided wave testing and structural imaging, with exception to quantitative thickness mapping using guided wave tomography which is outside the scope here and is discussed elsewhere e.g. [81-83]. It is typically avoided by use of non-dispersive modes, dispersive modes in their non-dispersive frequency range [84,85] or by deployment of dispersion compensation algorithms [86,87].

Figure 2.2 presents the Lamb wave dispersion curves in 10 mm mild steel plate between 0 and 1 MHz, obtained using DISPERSE [80]. Symmetric Lamb wave mode curves (red), solutions to (2.13), are denoted as (Sn), and antisymmetric Lamb wave curves (blue), solutions to (2.14), are denoted as (An), where n is the order of the mode. While the number of plate guided wave modes is infinite, the number of propagating modes depends on the frequency thickness product [73,85]. Only fundamental modes, S0 and A0, propagate for all frequencies. For higher order modes, dispersion curve cut-off points occur at specific frequency-thickness product values, where wavenumber k_z changes from imaginary or complex to real value. At low frequencies, below cut-off frequencies of higher order modes, only one symmetric and one antisymmetric fundamental mode exist. As frequency-thickness product increases, new modes appear

labelled with ascending numbers with accordance to order of appearance with increase in ωd (i.e. S1, S2, S3, etc. and A1, A2, A3, etc.). At cut-off points, phase velocities of the modes approach infinity, indicating that at these points longitudinal or shear waves reverberate across the thickness of the plate [62,65].

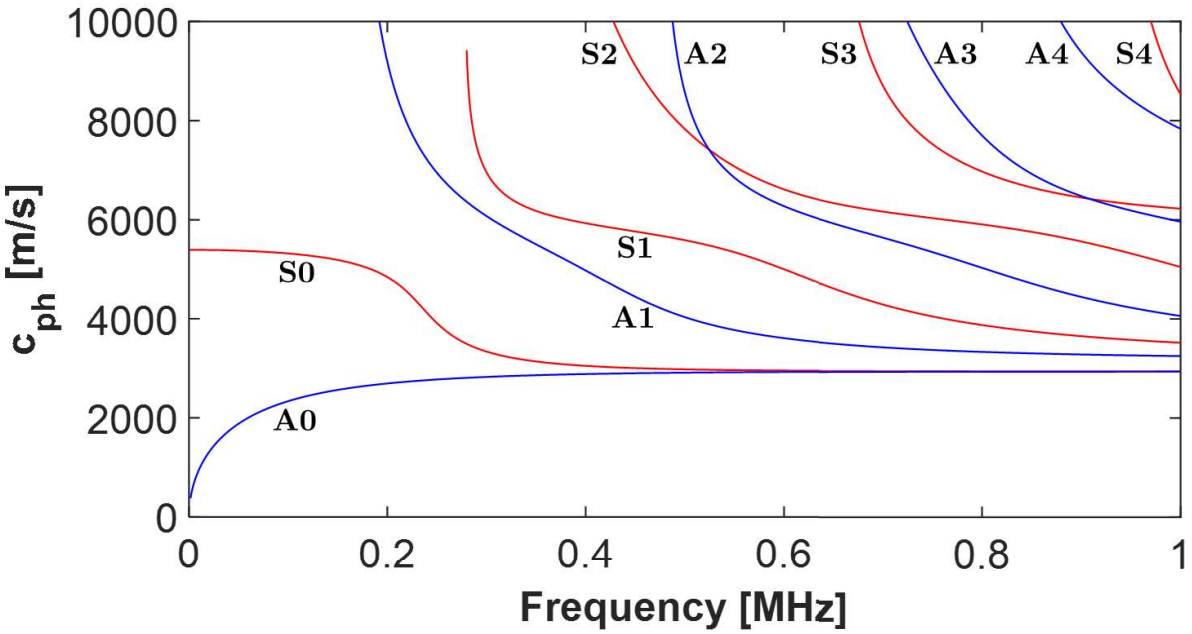

Figure 2.2: Lamb wave dispersion curves in 10 mm mild steel plate obtained using DISPERSE [80]. Symmetric modes are marked with red and antisymmetric modes are marked with blue.

Lord Rayleigh (1877) [88] and Stokes (1876) [89] observed that the velocity of a group of waves (i.e. wave packet) can be different than phase velocities of individual spectral components of the packet. This led to the concept of group and phase velocities. The group velocity is the velocity with which the modulation or envelope of the wave packet propagates and is the rate of energy transport for harmonic wave fields [90]. The phase velocity is the speed at which the individual peaks (spectral components) within that packet travel. For non-dispersive modes, these two velocities are equal. For dispersive modes, group velocity is given by:

$$c_g = \frac{d\omega}{dk} = \frac{c_p^2}{c_p - (fd)\frac{dc_p}{d(fd)}}, \tag{2.18}$$

where fd is the frequency-thickness product. When the derivative of c_p with respect to fd tends to infinity (at cut-off frequency), c_g tends to zero [65].

2.3.2 Shear horizontal waves

Shear horizontal (SH) waves are the second family of solutions to the free plate problem. They are the result of superposition of up and down-reflecting bulk shear waves, which are polarised along the x-direction, with wave vectors lying in the z-x-plane and inclined at such an angle that the system of waves satisfies traction-free boundary conditions on the surfaces of the plate [65,67]. A detailed geometrical analysis of partial wave interactions giving an origin to SH guided waves is presented in [64].

In section 2.3.1, plain strain was assumed to derive Lamb wave solutions. This assumption, however, does not account for infinite free plate problem solutions corresponding to SH waves. Therefore, here, for the complete set of solutions, an opposite assumption is made i.e. displacements only in x-direction are assumed, implying $u_z(x,y,z,t) = u_y(x,y,z,t) = 0$ [71]. Additionally, only solutions for which the scalar potential Φ vanishes are assumed [66]. Since wave fronts extend to infinity in the x-direction, the displacement u_x can be assumed to be independent of x. Applying the above assumptions to equations (2.6) and (2.7), they reduce to a single equation:

$$\frac{\partial^2 \boldsymbol{\psi}}{\partial x^2} = \frac{1}{c_T^2}\frac{\partial^2 \boldsymbol{\psi}}{\partial t^2}. \tag{2.19}$$

The general solution to (2.19) can be assumed to be of a form [62]:

$$\boldsymbol{\psi} = \psi_0(y)e^{i(k_z z - \omega t)}. \tag{2.20}$$

Substituting (2.20) into (2.19) and solving for $\psi_0(y)$ yields the general solution of a form [64]:

$$\psi_0(y) = A\,sin\left(k_{yT}y\right) + B\,cos\left(k_{yT}y\right) \text{ , where} \tag{2.21}$$

$$k_{yT} = \sqrt{\left(\frac{\omega}{c_T}\right)^2 - k_z^2} \tag{2.22}$$

is the through thickness transverse wavenumber component and A, B are the arbitrary constants.

In the case of SH waves, the free plate problem traction free boundary conditions ($\sigma_{yy}\big|_{y=\pm\frac{d}{2}} = \tau_{zy}\big|_{y=\pm\frac{d}{2}} = \tau_{xy}\big|_{y=\pm\frac{d}{2}} = 0$) reduce to only one non-trivial condition $\tau_{xy}\big|_{y=\pm\frac{d}{2}} = 0$, which implies $\frac{\partial \psi_x}{\partial y} = 0$ at $y = \pm\frac{d}{2}$. Substituting (2.21) into (2.20) and applying boundary conditions leads to:

$$A\cos\left(k_{yT}\frac{d}{2}\right) - B\sin\left(k_{yT}\frac{d}{2}\right) = 0 \text{ and} \tag{2.23}$$

$$A\cos\left(k_{yT}\frac{d}{2}\right) + B\sin\left(k_{yT}\frac{d}{2}\right) = 0, \tag{2.24}$$

Equations (2.23) and (2.24) are satisfied when [65]:

$$\sin\left(k_{yT}\frac{d}{2}\right) = 0, \text{ or} \tag{2.25}$$

$$\cos\left(k_{yT}\frac{d}{2}\right) = 0, \tag{2.26}$$

corresponding to symmetric and antisymmetric displacements (with respect to mid-plane $y = 0$) respectively. The above is only true when:

$$k_{yT} = \frac{n\pi}{d}, \text{ where} \tag{2.27}$$

n = *0, 1, 2, 3, 4, …* is a whole number and determines the mode order. The notation of modes has a form of SHn, where odd n values correspond to antisymmetric SH modes and the even values correspond to symmetric ones. Equation (2.27) is known as the dispersion equation.

By substituting (2.15) and (2.22) into (2.27) and rearranging, the expression for the phase velocity as a function of frequency-thickness product is obtained:

$$c_p(fd) = \pm 2c_T\left(\frac{fd}{\sqrt{4(fd)^2 - n^2c_T^2}}\right). \tag{2.28}$$

In contrast to Lamb waves, the above expression is explicit and does not have to be solved numerically. When $n = 0$, the phase velocity is constant with frequency-thickness product and is equal to the bulk shear wave velocity c_T. Hence, the

fundamental mode SH0 is non-dispersive. For all other higher order SH modes with $n \neq 0$ the phase velocity changes with frequency-thickness product which makes them dispersive. The SH wave dispersion curves resulting from (2.28) are plotted in Figure 2.3 using DISPERSE [80], for a mild steel plate and the frequency range between 0 and 1 MHz.

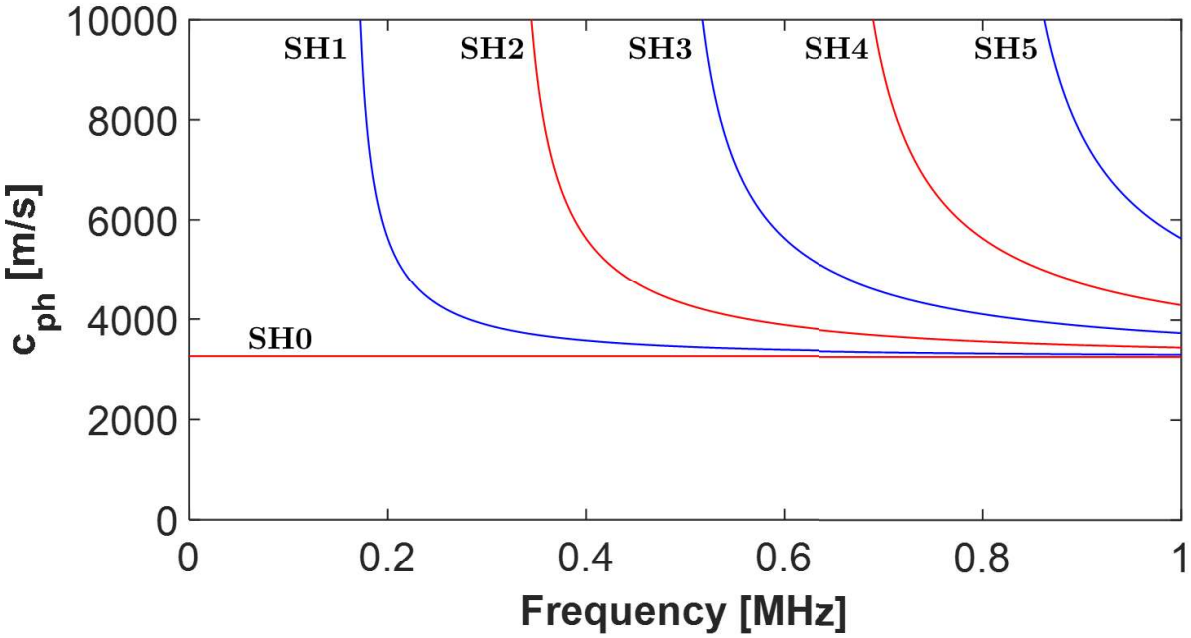

Figure 2.3: Phase velocity dispersion curves for SH guided wave modes in 10 mm mild steel traction free plate. Symmetric modes are marked with red and antisymmetric modes are marked with blue. The curves were plotted using DISPERSE software [80].

Like in the case of Lamb waves, higher order SH wave modes have cut-off frequencies, which are the frequencies at which the mode changes from propagating to non-propagating [66]. Only the fundamental SH0 mode propagates at the full range of the frequency spectrum. The analytical expression for the cut-off frequency of the n^{th} SH mode can be established from equation (2.28) by setting the denominator to zero [65].

The explicit expression for SH waves group velocity can be easily derived from equation (2.27) as shown in [65], and it is:

$$c_g = c_T \sqrt{1 - \frac{(n/2)^2}{(fd/c_T)^2}} \,. \tag{2.29}$$

2.4. Pipe guided waves

Pipes and other similar tubular structures can also act as waveguides for elastic waves. Guided waves in pipes can be categorised based on the direction of propagation into circumferential pipe guided waves, propagating in the circumferential θ-direction, and axial pipe guided waves propagating in the axial z-direction. The research presented in this thesis is concerned with axial guided waves which from here onwards will be referred to as pipe guided waves. The circumferential pipe guided waves are outside the scope here and are discussed elsewhere e.g. [65,75,91-93].

Propagation of axial pipe guided waves has been the subject of research interest for over a century. The propagation of harmonic elastic waves in an infinite full solid cylinders was first discussed by Pochhammer (1876) [94] and Chree (1886)(1889) [95,96]. The first solution to symmetric wave propagation in hollow cylinders was presented by Ghosh (1923) [97] and the full set of pipe guided wave solutions was analitically derived by Gazis (1958)(1959) [98,99].

The pipe guided wave theory briefly outlined in this section follows derivation presented in [99]. The pipe is approximated with an infinite elastic isotropic free hollow cylinder to avoid additional boundary conditions at both ends of the pipe. The problem geometry is presented in Figure 2.4, for convenience it is defined in the cylindrical coordinate system.

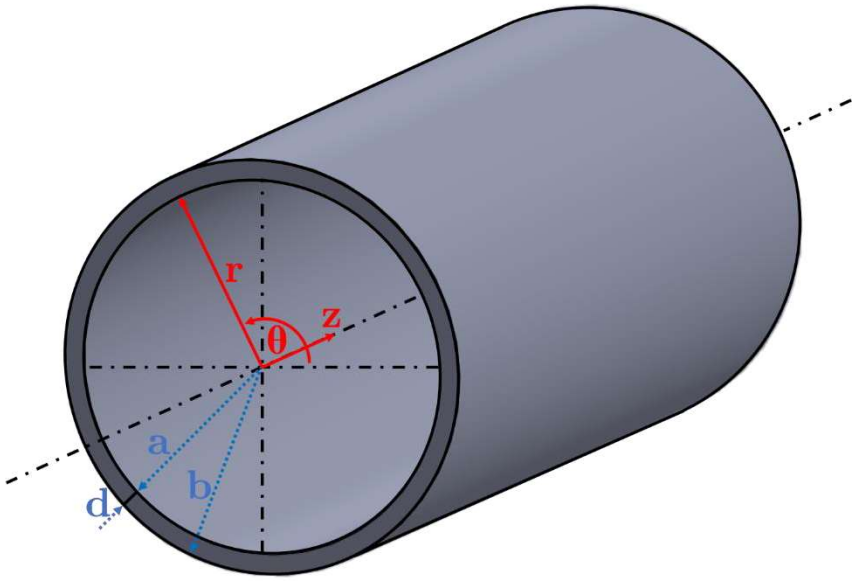

Figure 2.4: A schematic outline of traction free, isotropic, infinitely long hollow cylinder with inner radius a, outer radius b and wall thickness d.

Propagation of pipe guided waves is governed by Navier's equation of motion (2.1) which can be decomposed into the Helmholtz differential equations (2.6) and (2.7) as it was the case for bulk waves and plate guided waves. Taking advantage of the fact that Helmholtz differential equations can be divided into the products of functions of each of the spatial dimensions [100], Gazis (1959) [99] proposed the following expressions for the scalar potential Φ and directional components of the vector potential $\boldsymbol{\psi}$:

$$\begin{aligned} \Phi &= f(r)\cos m\theta \cos(\omega t + k_z z), \\ \boldsymbol{\psi_r} &= g_r(r)\sin m\theta \sin(\omega t + k_z z), \\ \boldsymbol{\psi_\theta} &= g_\theta(r)\cos m\theta \sin(\omega t + k_z z), \\ \boldsymbol{\psi_z} &= g_z(r)\sin m\theta \cos(\omega t + k_z z), \end{aligned} \tag{2.30}$$

where k_z is the axial wavenumber and m is the whole number denoting the circumferential order.

Substituting, in turn, expressions for the scalar potential and vector potential from (2.30) into (2.6) and (2.7) respectively and using the differential operator notation:

$$\mathcal{B}_{\mathrm{p},r} = \left[\frac{\partial^2}{\partial r^2} + \frac{1}{r}\frac{\partial}{\partial r} - \left(\frac{p^2}{r^2} - 1\right)\right], \tag{2.31}$$

yields the following valid solution for Φ:

$$\mathcal{B}_{\mathrm{p},\, k_{rL}r}[f] = 0, \tag{2.32}$$

and the following solutions for $\boldsymbol{\psi}$:

$$\begin{aligned} \mathcal{B}_{p,\, k_{rT}r}[g_3] &= 0, \\ \mathcal{B}_{p+1,\, k_{rT}r}[g_r - g_\theta] &= 0, \\ \mathcal{B}_{p+1,\, k_{rT}r}[g_r + g_\theta] &= 0, \end{aligned} \tag{2.33}$$

where $k_{rL}^2 = \frac{\omega^2}{c_L^2} - k_z^2$ and $k_{rT}^2 = \frac{\omega^2}{c_T^2} - k_z^2$ are the radial components of the wave number vectors, which describe the radial variation of the potential functions [99].

The general solutions of equations (2.32) and (2.33) are [65]:

$$\begin{aligned} f(r) &= AZ_p(\alpha_1 r) + BW_p(\alpha_1 r), \\ g_3(r) &= A_3 Z_p(\beta_1 r) + B_3 W_p(\beta_1 r), \\ 2g_1(r) = (g_r(r) - g_\theta(r)) &= 2A_1 Z_{p+1}(\beta_1 r) + 2B_1 W_{p+1}(\beta_1 r), \\ 2g_2(r) = \big(g_r(r) + g_\theta(r)\big) &= 2A_2 Z_{p-1}(\beta_1 r) + 2B_2 W_{p-1}(\beta_1 r), \end{aligned} \tag{2.34}$$

where $\alpha_1 r = |k_{rL} r|$, $\beta_1 r = |k_{rT} r|$, $g_3 = g_z$, A, B, A_1, B_1, A_3, B_3 are arbitrary amplitudes, and Z_p, W_p denote the p$^{\text{th}}$ order of Bessel functions, modified Bessel functions or Hankel functions (depending on whether k_{rL} and k_{rT} are real or imaginary). For an in-depth discussion on selection of appropriate Bessel functions please refer to [65,101].

Gauge invariance allows elimination of one of the potentials without loss of generality of the solution [99,101]. Setting $g_2 = 0$, implies:

$$g_r = -g_\theta = g_1, \tag{2.35}$$

which changes equations (2.34) into three independent potential functions, $f(r)$, $g_1(r)$ and $g_3(r)$.

By substitution of equation (2.34) into the cylindrical coordinate version of equation (2.4) the displacement field can be expressed as:

$$u_r = [f' + (m/r)g_3 + k_z g_1]\cos m\theta \cos(\omega t + k_z z),$$
$$u_\theta = [-(m/r)f + k_z g_1 - g_3']\sin m\theta \cos(\omega t + k_z z), \quad (2.36)$$
$$u_z = \left[-k_z f - g_1' - (m+1)\left(g_1/r\right)\right]\cos m\theta \sin(\omega t + k_z z),$$

where primes denote differentiation with respect to coordinate r.

Using elasticity theory, and applying traction free boundary conditions, $\sigma_{rr} = \tau_{rz} = \tau_{r\theta} = 0$, at inner and outer surfaces of hollow cylinder ($r = a, b$), leads to the following system of eigenvalue equations:

$$c_{ij}\boldsymbol{Q} = 0 \quad (i, j = 1, 2, 3, \ldots, 6), \quad (2.37)$$

where c_{ij} is a six by six matrix, i is the row index, j is the column index, and $\boldsymbol{Q}$ is a vector $[A, B, A_1, B_1, A_3, B_3]$ containing the unknown amplitudes from (2.34). For non-trivial solutions, the determinant of the coefficient matrix c_{ij} must vanish, implying:

$$\left|c_{ij}\right| = 0. \quad (2.38)$$

The above characteristic equation is known as the dispersion equation. The expressions for each c_{ij} coefficient are given in for example [65] and [62].

For known dimensions of the hollow cylinder and fixed elastic constants, the characteristic equation (2.38) is an implicit transcendental function of d/λ and fd/c_T, where λ is the wavelength, f is a frequency, d is the wall thickness and c_T is the bulk shear velocity [99]. The roots of this equation can be computed numerically by fixing d/λ or fd/c_T and using iterative techniques as presented in [80,101,102]. The DISPERSE software mentioned previously is also capable of finding the solutions to (2.38) for an arbitrary cylinder. The results are typically presented in the form of a dispersion curve plot of wavenumber or phase velocity versus frequency, in which each curve corresponds to a specific pipe guided wave mode.

There are two special cases when (2.38) simplifies to a product of two sub-determinants of four by four and two by two dimensions [99]. This happens when the wavenumber

k_z is equal to zero or when the number of waves around the circumference, given by circumferential order m, is equal to zero. The former case implies infinite axial wavelength, since $\lambda_z = {}^{2\pi}/_{k_z}$, which means the motion is independent of z. This case corresponds to either plain-strain motion discussed in detail in [98] or longitudinal shear vibrations involving only longitudinal displacements u_z, discussed in [62,99].

In the second degenerate case, with $m = 0$, motion is independent of the angular coordinate θ. This case corresponds to the two pipe guided wave mode families that are of particular importance in GWT. These are axially symmetric longitudinal and torsional modes and they are discussed below.

The notation of guided wave modes used in this thesis follows the convention established in [103]. The letter denoting mode family (i.e. longitudinal (L), torsional (T) and flexural (F)) is followed by indices (m,n). Index m is the mode circumferential order, i.e. number of harmonic displacement and stress variations around the pipe circumference. Modes with $m = 0$ are axisymmetric. Index n is a consecutive order in which modes are appearing with the increase in the frequency. It is also associated with complexity of the mode shapes through the wall thickness (analogically to plate guided wave mode numbers, although here numbering starts from 1, not 0).

2.4.1 Longitudinal pipe modes

The motion of the longitudinal pipe modes occurs in the r-z-plane, and the circumferential particle displacement component u_θ is zero. As mentioned before, since the circumferential order m is zero, the displacements u_r and u_z are independent of circumferential position θ. The family of longitudinal modes, sometimes called breathing modes [104], involves both dilatational and equivoluminal waves through the potentials f and g_1 defined in (2.34). The longitudinal modes are denoted by L(0,n), for example the fundamental mode is L(0,1).

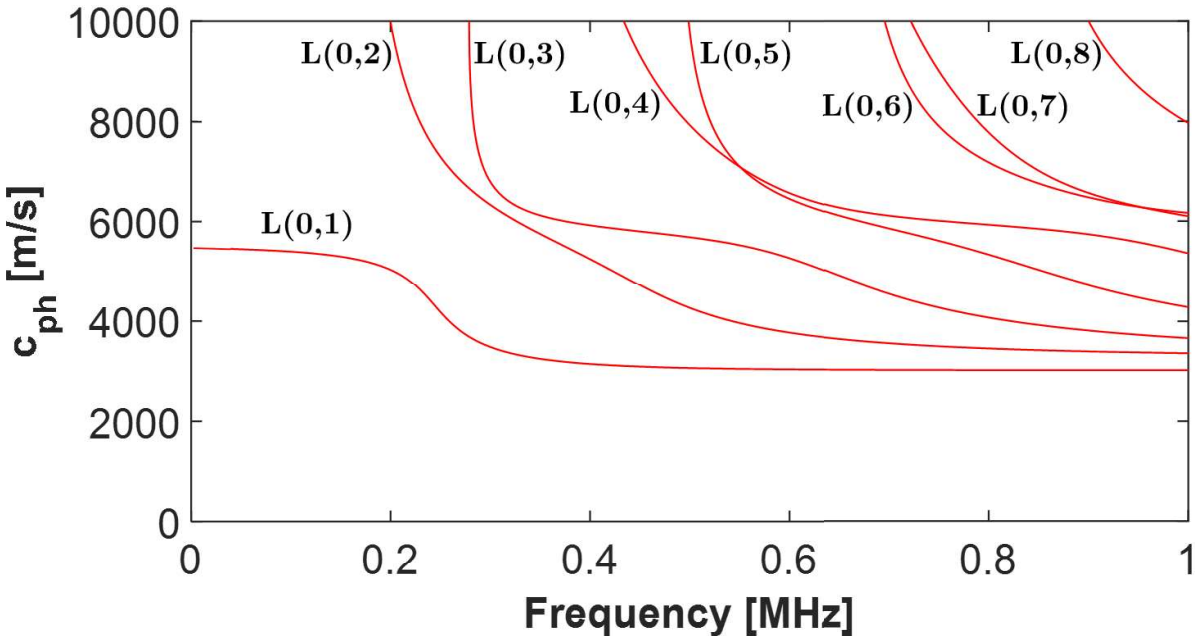

Figure 2.5: Phase velocity dispersion curves of longitudinal pipe guided wave modes in a mild steel 8 inch pipe with 10 mm wall thickness. The curves were obtained using DISPERSE software [80].

Figure 2.5 presents the phase velocity dispersion curves of longitudinal pipe modes. Analogically to plate guided waves, only the real solutions of (2.38) are plotted, which correspond to propagating modes. The higher order longitudinal wave modes also have cut-off frequencies at which the modes change from propagating to non-propagating ones [66]. Only the fundamental L(0,1) mode propagates through the full range of the frequency spectrum. It is worth noting that dispersion curves of longitudinal pipe modes are almost identical to the dispersion curves of Lamb waves in the free plate made of the same material and with the same thickness as the hollow cylinder wall thickness. The dispersion curves of the longitudinal pipe modes only deviate from the plate Lamb mode curves at low frequencies as the curvature becomes more significant. The similarity between plate and pipe guided wave modes has been discussed in greater detail in [76,77,104].

2.4.2 Torsional pipe modes

The motion of the torsional pipe modes consists of only circumferential displacement component u_θ [65]. It can be thought of as a 'twisting' motion in a pipe. The

displacement components u_r and u_z are both equal to zero. The torsional pipe mode displacement is axially symmetric and independent of circumferential position θ. This family of modes is denoted by T(0,n), for example, the fundamental mode is T(0,1).

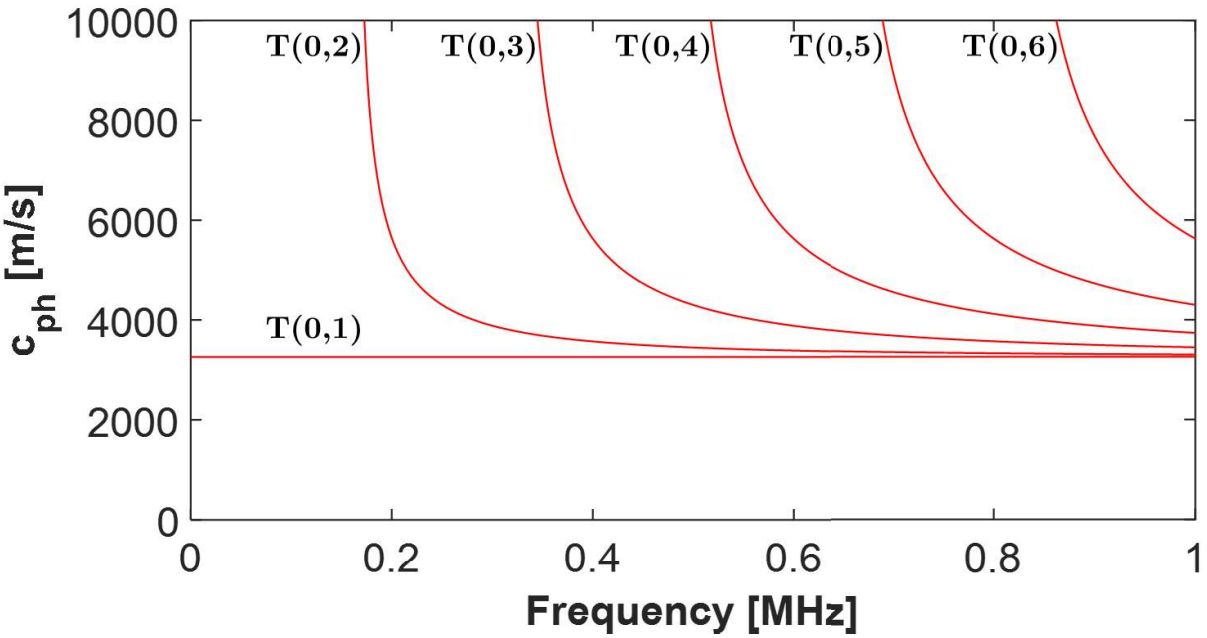

Figure 2.6: Phase velocity dispersion curves of torsional pipe guided wave modes in a mild steel 8 inch pipe with 10 mm wall thickness. The curves were obtained using DISPERSE software [80].

Figure 2.6 presents the phase velocity dispersion curves of propagating torsional pipe modes. The fundamental T(0,1) mode propagates at full frequency spectrum and is non-dispersive. All higher order modes are dispersive, and they have cut-off frequencies below which they do not propagate. The phase velocities of all the torsional modes decrease monotonically from infinity and tend to shear bulk wave velocity c_T as the frequency increases. As was the case for longitudinal modes, dispersion curves of torsional modes strongly resemble the ones of the SH plate modes when material and plate/wall thicknesses match. The resemblance is associated with the similarity of displacement mechanisms between these two guided wave families. The analogy between plate and pipe guided waves is discussed in greater detail in section 2.4.4.

2.4.3 Flexural pipe modes

When $k_z \neq 0$ and $m \neq 0$, the equation (2.38) does not degenerate to simple cases and

hence the solution involves the full six dimensional determinant. This means that motion comprises all three displacement components u_θ, u_r and u_z, which are coupled together through the boundary conditions giving rise to the last family of wave modes existing in pipes called flexural modes [99]. Since $m \neq 0$, the displacement of these modes varies around the circumference and hence they are non-axisymmetric. The flexural pipe modes are denoted by F(m,n).

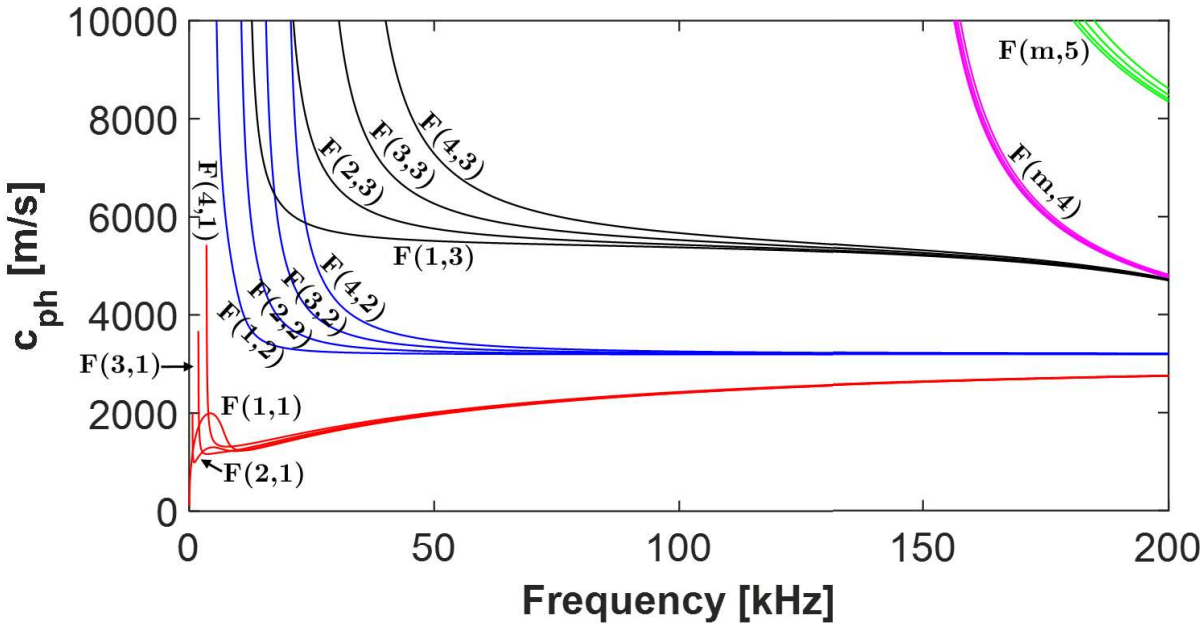

Figure 2.7: Phase velocity dispersion curves of flexural pipe guided wave modes in a mild steel 8 inch pipe with 10 mm wall thickness. Modes of the same consecutive order n are marked with the same colour. Only flexural modes up to fourth circumferential order m are plotted. Red curves mark F(m,1), blue mark F(m,2), black mark F(m,3), magenta mark F(m,4) and green mark F(m,5) modes. The curves representing modes of different circumferential orders which belong to F(m,4) and F(m,5) flexural mode families are not labelled separately in the plot. Instead they are denoted with F(m,4) and F(m,5) labels indicating multiple curves that are too close together to label individually.

The dispersion relationships of flexural pipe modes are presented in Figure 2.7. There is an infinite number of flexural mode circumferential orders, here only flexural modes up to the fourth circumferential order are plotted. Only the lowest F(1,1) mode propagates at all frequencies. As it was the case for the two other pipe mode families, all higher flexural modes have cut-off frequencies. As the frequency increases and consequently the wavelength to radius ratio decreases, the velocity of flexural modes converges to either a longitudinal or torsional mode. For example, F(m,1) modes (red

curves) converge to L(0,1), F(m,2) modes (blue curves) converge to T(0,1), F(m,3) modes (black curves) converge to L(0,2) and so on [104]. The torsional and flexural modes converging to T(0,1) are sometimes referred to as the torsional-flexural pipe mode family [25].

2.4.4 Plate pipe analogy

Similarity of dispersion curves and particle motion of pipe guided waves and plate guided waves led to discovery of the analogy between these guided waves which was first described in [104,105]. It was shown in [25,58,76,77] that pipe guided wave modes can be approximated by plate guided wave modes. Such approximation involves virtual 'unwrapping' of the pipe and treating it as a flat infinite isotropic periodic plate as presented in Figure 2.8.

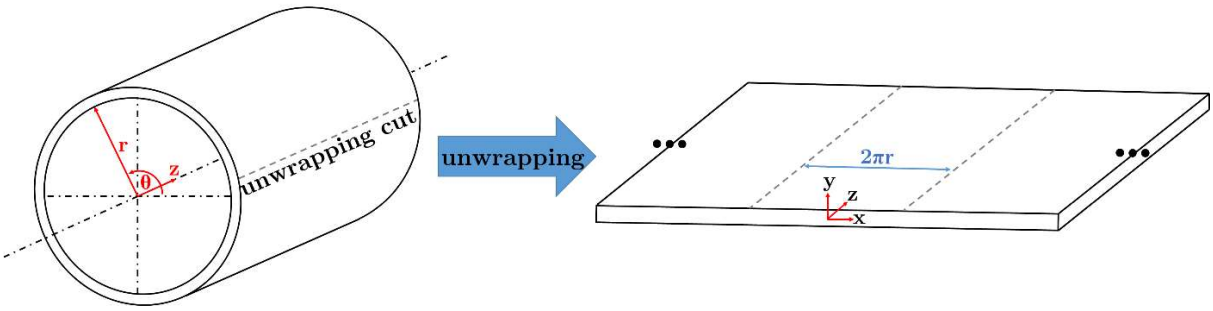

Figure 2.8: Schematic presenting the pipe and its periodic unwrapped plate analogy.

Since pipe guided wave modes are 'global' solutions to the wave equation in a pipe, they must be continuous around the pipe circumference. To account for that, to the classic free plate problem an extra boundary condition is added which states that the two solutions on either side of the axial cut have to match [25]. This is satisfied when there is an integer number of wavelengths $n\lambda$ between the matching wave fronts. As a consequence, pipe guided wave modes can be approximately considered as plate guided waves travelling at specific discrete helical directions in a pipe, with each discrete propagation angle corresponding to a different pipe mode. The approximation leads to

simplification of the full 6-dimensional pipe mode dispersion relationships to the much simpler plate mode dispersion relationships.

The approximation of pipe guided wave modes with the plate modes is based on an assumption that the pipe wall curvature has negligible effect on wave propagation. As shown in [76,77], the assumption is accurate when pipe wall thickness is much less than the pipe radius and the wavelength is much less than the pipe circumference. In most of the large diameter industrial pipes the wall thickness is far less than their radius, fulfilling the first condition. While there are no strict rules determining an acceptable frequency-radius ratio for the approximation, it is possible to estimate the error associated with treating pipe guided waves as analogical plate guided wave modes. Davies and Cawley (2009) [25] proposed an empirical formula for calculation of maximum phase velocity error due to approximation of the torsional flexural pipe mode family (T(0,1), F(1,2), ..., F(m,2)) with SH0 plate guided wave mode, which is as follows:

$$err\% = \left(\frac{7c_T}{2\pi f r_m}\right)^2 \approx \left(\frac{c_T}{f r_m}\right)^2, \tag{2.39}$$

where c_T is the shear wave bulk velocity, f is temporal frequency and r_m is the mean pipe radius. Similar approximation error estimates together with more thorough discussion on plate-pipe guided wave analogy can be found in [77] and [76].

Thanks to the plate pipe analogy, the extensive studies on guided wave scattering from defects in plates [106-115] can be applied to pipe guided wave scattering from defects, which significantly simplifies the analysis.

2.5. Implementation of pipe guided waves to non-destructive testing

The concept of pipe guided waves as means of damage detection in pipes and tubes

was investigated in the second half of the last century [23,103,116-122]. The first two commercial implementations of pipe guided waves to non-destructive testing were Teletest by TWI subsidiary Plant Integrity Ltd. [123] and Wavemaker by Guided Ultrasonics Ltd. [21]. The technology has evolved and matured over three decades since commercialisation. It is now established in a number of national and international standards as a screening method (e.g. BS ISO 18211:2016, BS 9690:2011, ASTM E2775-2011, ISO/DIS 18211.2). GWT is routinely deployed in various inspection scenarios including road crossings, corrosion under insulation, buried pipes, offshore risers, non-piggable pipes and many more. The main advantages of pipe GWT include:

- large volumetric coverage from a single device position,
- ability to inspect hard to reach pipes including embedded and buried pipes [124,125],
- ability to inspect long lengths of pipes covered with insulation from only a small section where insulation is removed,
- ability to inspect pipes while they are in service, filled with and/or submerged in fluid, even when their surface temperature is high (up to 350°C)[1],
- ability to detect inner and outer surface breaking defects as well as subsurface defects [84],
- no requirement for special surface preparation other than wire brushing to remove any loose coatings and corrosion products on the pipe, and
- capability to inspect a wide range of pipe sizes, from as small as 0.75 inch to as large as 60 inches [1].

This section briefly outlines the recent advances in GWT and its state-of-the-art commercial implementations.

2.5.1 Mode selection

The choice of appropriate pipe guided wave mode is paramount for successful NDT inspection. In the early days of pipe GWT development, it was established that the inspection pipe mode should possess the following characteristics [119,120].

The desired mode should be axially symmetric and have uniform displacement across the pipe wall to provide equal sensitivity throughout the pipe cross section. A symmetric mode is also easier to selectively excite in a pure form [22]. Moreover, such a mode has another advantage when it comes to defect characterisation. It will produce a symmetric reflection from a symmetric feature e.g. uniform welds or flanges. Defects are usually non-axisymmetric hence reflection from them will introduce non-axisymmetric modes. The presence of non-axisymmetric modes allows the distinction of non-axisymmetric feature indications (e.g. defects or supports) from reflections from known symmetric features [126]. In fact, as discussed in the subsequent section, the ratio of symmetric to non-axisymmetric mode amplitudes is useful in defect circumferential extent estimation.

The mode of choice should also be non-dispersive. Dispersion leads to elongation and consequent decrease in amplitude of the probing wave packet as it propagates along the pipe, leading to a decrease in SNR and spatial resolution [20,85].

The last requirement is the ability to selectively excite only the desired mode. As shown in section 2.4, there are infinitely many guided wave modes that exist in the pipe. Propagation of additional undesired modes during inspection leads to high coherent noise which significantly reduces the SNR and hence the sensitivity to defects [127]. Therefore, it is preferred to limit the number of transmitted probing pipe modes to a single mode to simplify analysis of the recorded data so that indications from defects and pipe features are easily distinguishable.

There are only two pipe guided wave modes that meet the above criteria. These are longitudinal L(0,2) and torsional T(0,1) modes. Thanks to their simple axisymmetric mode shapes, both can be easily transmitted without excitation of flexural pipe modes via application of uniform excitation around the entire pipe circumference.

The L(0,2) mode was initially used in the first commercial implementations of pipe GWT systems [21,123]. It is practically non-dispersive over a wide range of frequencies and its displacement through the pipe wall can be assumed uniform. Selective excitation of only the L(0,2) mode is possible through the adequate design of the transduction system allowing suppression of the unwanted, highly dispersive L(0,1) mode as discussed in [128]. Furthermore, the frequency range used during inspection has to be below the cut-off frequency of the higher order L(0,3) mode to avoid its excitation. The capability to inspect up to 100 m of chemical plant pipeline with butt welds and supporting brackets using L(0,2) mode was confirmed in [121].

At present, most GWT is undertaken using the fundamental torsional mode rather than the L(0,2) mode [20]. The T(0,1) mode offers a range of advantages over the L(0,2). It propagates at all frequencies, allowing suppression of the other undesired modes by simply using the frequency range below the cut off frequencies of higher order modes. Thanks to that, the torsional transduction system is simpler, more compact and hence more practical and cheaper to manufacture compared to similar systems transmitting the L(0,2) mode. In the case of the T(0,1) mode there is no need for extra mode suppression that needs to be incorporated in the longitudinal mode transduction design. The fundamental torsional mode is non-dispersive at all frequencies and has practically a uniform displacement through the pipe wall thickness providing a full volumetric coverage. The key advantage of the torsional mode over the longitudinal one is that the former is not affected by low-viscosity liquid present inside or outside the pipe. This is because the low-viscosity liquids do not support

shear waves, hence there is no coupling nor energy leakage into the liquids. In the case of higher-viscosity liquids the energy leakage remains low. On the other hand, the motion of the L(0,2) mode (and other longitudinal modes) comprises some radial displacements which couple into liquids. This leads to substantial alteration of dispersion relationships in presence of liquid inside or outside the pipe [129,130] as well as energy leakage and resulting significant attenuation.

While the T(0,1) mode performs well in most inspection scenarios, there is a limited number of cases when the longitudinal L(0,2) pipe mode is preferred, for example, it has lower attenuation in some coated [131] and buried [124] pipe cases. These, and other cases are outlined in [84].

2.5.2 Practical implementation of pipe guided wave testing in commercial systems

Most modern GWT systems perform inspection in pulse echo configuration. The tests are usually performed in the low frequency regime (i.e. <100 kHz). GWT uses tone burst excitation in the form of wave packets, consisting of a number of sine function cycles modulated with a time window (e.g. a Gauss or Hann window). Such excitation provides narrow frequency band, minimising the dispersion effects while maintaining a relatively short excitation time to minimise the dead zone immediately after the transducer and maximise axial resolution.

The inspection setup typically consists of a transduction ring connected to an electronic unit with a graphical display as presented in Figure 2.9. The ring incorporates an array of equally spaced transducers. During an inspection, it is attached around the outer pipe circumference. The transduction ring can be either mounted for a one off inspection after which it is removed, or it can be permanently installed on the pipe for structural health monitoring [132,133]. Depending on the intended application, there is

a wide range of transduction ring designs including inflatable, solid, claw, permanent, low profile and specialist subsea rings [1]. One of the main objectives in the ring design is to provide an even coupling of transducer energy into the pipe which is crucial for excitation of symmetric modes without simultaneous excitation of non-axisymmetric flexural modes.

Figure 2.9: An example of guided wave testing inspection setup [19].

A variety of transducers based on piezoelectricity, electromagnetism, and laser pulses can be used in pipe GWT, depending on the application needs with respect to environment, coupling, and size. The two most popular types of transducers are the contact shear wave piezoelectric transducers [119] and the electromagnetic acoustic transducers (EMATs) [134-139]. The piezoelectric transducers are typically dry coupled to the pipe surface because at low frequencies, which are used in GWT, this type of coupling performs comparably to liquid coupling [119].

Most commercially available transduction rings consist of two rows of transducers for the purpose of directional control [20]. The rows are separated by a precise distance (typically quarter of the wavelength), so that application of phase shift to excitation

using one ring leads to constructive wave interaction with the excitation from the second ring in the direction of propagation and destructive interference in the opposite direction. This results in waves propagating only in the desired direction. While in the past directional control was physically preformed during the inspection, currently, it is typically performed in post processing where the phase shift can be adjusted more accurately for a better result.

Another important consideration in ring design is circumferential pitch distance between the equally spaced transducer array elements. The spacing around the pipe must satisfy the Nyquist-Shannon sampling criterion for the highest frequency of the transmitted wave packet frequency bandwidth to allow excitation of a pure symmetric pipe guided wave mode. Therefore, to satisfy the sampling criterion, the pitch distance must be less or equal to half of the smallest probing wavelength.

The electronic control unit with graphical display is the key system component that generates the waveforms, amplifies the transmitted and acquired signals, acts as analogue to digital converter and records the ultrasonic data. It performs hardware checks, calibrates the system and allows the adjustment of inspection parameters. Some more advanced units are capable of displaying the results and aiding in their analysis.

An example result of modern GWT inspection of a defective pipe (two internal pitting corrosion defects) performed using an EFC Solid Ring paired with Wavemaker® G3 by Guided Ultrasonics Ltd. [1] is presented in Figure 2.10. It consists of an A-scan with the amplitudes of torsional and flexural mode reflections from features in the pipe. The A-scan is accompanied by the C-scan image in a form of an unwrapped pipe display.

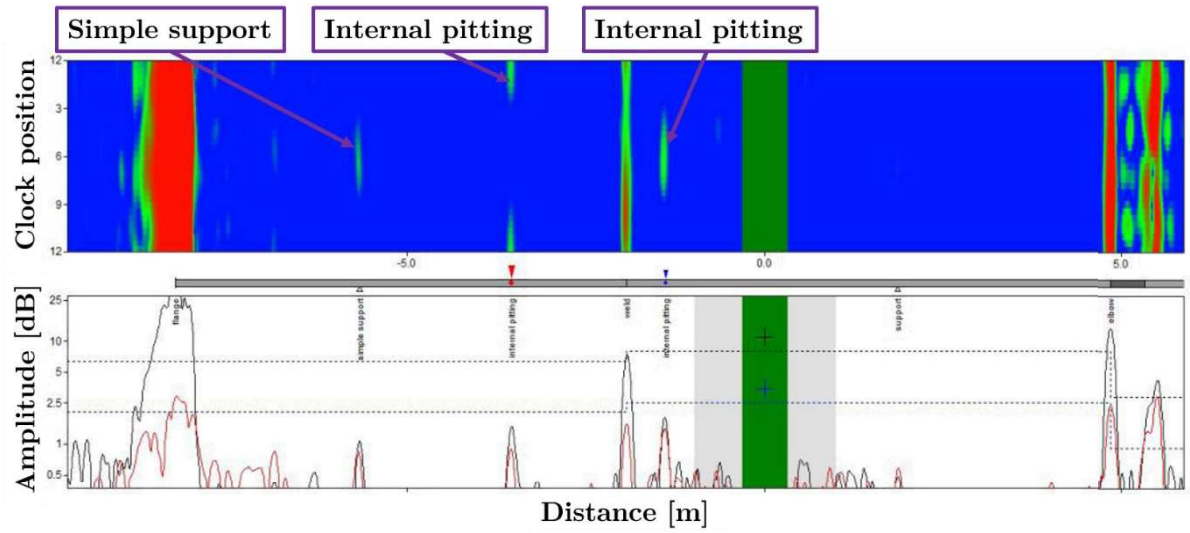

Figure 2.10: Example of modern GWT inspection of pipe with two defects using Guided Ultrasonics Ltd. [19] system. In the A-scan the T(0,1) mode reflections are marked with black, and the flexural wave reflections are marked with red. The transduction ring is at 0 m.

The C-scan is a synthetic focusing imaging reconstruction. Typically CSM or FMC based algorithms are used. It is important to note that the current GWT system design does not allow for high resolution imaging. The neighbouring array elements in the transduction ring are wired together essentially forming large elements referred to as channels. Therefore, in practice, a GWT ring contains two arrays (transducer rows) of six to eight elements. Each element consists of two or more neighbouring transducers which transmit and receive as one. Therefore, the unwrapped pipe display helps to visualise the axial and circumferential position of defects and pipe features, however its resolution is not sufficient for reliable defect sizing. The main interest of the project presented in this thesis is to substantially improve the resolution of guided wave imaging, to allow defect size estimation from the reconstructed image.

2.5.3 Capabilities of modern guided waves systems

At present, GWT using the fundamental torsional guided wave mode is capable of detection of defects of around 3 % to 5 % of cross-sectional area (CSA) in a one off inspection [133,140] and less than 1 % CSA in the case of permanently installed

monitoring with frequent collection of data [141,142]. The sensitivity, however, greatly depends on the condition of the pipe and presence of pipe features such as welds, supports, bends, etc. [20,133,143]. The highest sensitivity is usually achieved in straight sections of pipes in good condition with low density of pipe features. The sensitivity in older pipes with higher density of features, general corrosion or bonded coatings (e.g. bitumen) is typically lower [20,144].

The reflection coefficient of the T(0,1) mode is approximately linearly dependent on defect CSA [22]. Therefore, it is possible to roughly estimate CSA of a defect via GWT inspection [24]. The same CSA can correspond to a defect that is narrow and deep or a defect that is wider and shallow. Hence, knowledge of defect circumferential extent is very useful in defect criticality assessment.

As mentioned earlier in this section, it is possible to estimate the circumferential extent of the detected defect. This is based on the fact that the amount of mode conversion of the axisymmetric T(0,1) mode to non-axisymmetric F(m,2) modes depends on the circumferential extent of a defect. Hence, it is possible to relate the ratio of reflected amplitudes of flexural and torsional modes, to the percentage circumferential extent of a defect, as was shown in [22]. However, this method is insensitive to small circumferential extent changes in the case of small defects. Only circumferential extents of defects larger than around $10 - 15$ % of the circumference can be reliably estimated [24].

The work presented in this thesis aims to improve defect sensitivity and circumferential extent estimation capabilities using one off GWT inspection, to address current limitations of this technique.

2.6. Summary

This chapter outlined the fundamentals of bulk waves and guided waves in plates and

pipes. The analogy between the plate and pipe guided wave solutions was discussed. The practical implementation of pipe guided waves to NDT was explained and current capabilities of state-of-the-art GWT systems were briefly outlined.

This page intentionally left blank

3. Adaptation of synthetic focusing imaging to SH0 pipe guided wave testing

3.1. Introduction

The phased array synthetic focusing imaging methods reconstruct the interrogated area from the ultrasonic data recorded after the insonification of the ROI with the unfocused probing waves. The reconstruction methods considered in this thesis use a simple wave propagation model assuming a constant wave velocity and associating a distance with a time-of-flight measurement. The aim of the algorithm is to map the scattering indications from the recorded waves onto the image space using time-of-flight so that the final reconstruction represents the structure of the ROI.

The scattering is a result of interactions of waves propagating through the medium with the local acoustic impedance changes, e.g. density or compressibility changes [100]. An impedance change can be due to a known benign feature or a sought defect. For example, cracks, which are the main interest of this thesis, are breaks or fissures in the material. Therefore, cracks cause a sudden localised change in density from that of the structure's material to that of the surrounding medium (e.g. air, water), which is typically significantly lower. By recording waves scattered from defects, information about them can be retrieved from the ultrasonic data through the reconstruction procedure [145,146].

The final image reconstructed using synthetic focusing imaging is essentially a scattering map of the interrogated area. It is not a perfect representation of the ROI. As will be discussed in section 3.6, the resolution of the classic ultrasonic imaging is diffraction limited [147], therefore some information about the inspected area is inevitably lost during the acquisition and reconstruction. Nevertheless, the

reconstructed image contains the information on location and approximate size (provided it is larger than the resolution) of the material discontinuities. The image together with a prior knowledge of the geometry of the inspected structure allows distinction of the potential defect indications from the known benign features. The size of detected defects can then be estimated from their indications in the image [25,34,58].

As discussed in chapter 1, the phased array synthetic focusing imaging methods achieve synthetic focusing on every point (pixel) in the image by application of delay laws and linear superposition to the previously acquired ultrasonic data in post processing. The focusing is possible when waves are recorded from a range of different angles. This allows the application of delays to signals recorded at each angular position (array element) so that indications in the time traces corresponding to a particular arbitrary point P in the image domain can be coherently added. Coherent summation of all the waves scattered by a point is essentially equivalent to physical focusing at this location. The same operation is performed for all points in the ROI creating an image that is fully focused on reception.

To further improve the resolution, additional synthetic focusing can also be performed on transmission. When the interrogated area is illuminated with unfocused waves transmitted from the range of different angles (e.g. FMC or PWI acquisition schemes), for each illumination angle the image focused on reception is reconstructed. In each of these images, the delays applied to synthetically focus at an arbitrary point P take into account the length of the path through which the transmitted wave travelled to this point P. For the same point P, this path is different for each illumination angle with unfocused waves. Hence, to focus at point P during each reconstruction a different delay accounting for the transmission angle is applied in post processing. When images obtained through synthetic focusing on reception, using a range of different insonification angles, are coherently added, each pixel P represents the sum of

contributions from all insonification angles. Consequently, the delays accounting for different incident wave travel times are incorporated into the compound image. This process is analogous to synthetic focusing on reception, where contributions from all array elements—each positioned at a different angle with respect to pixel P—are coherently added to obtain the intensity of pixel P. As a result, the delays accounting for different scattered wave travel times are incorporated into the reception-focused image. By coherently summing the reception-focused images obtained for a range of different transmission angles, a compound image is achieved. This compound image is focused on both transmission and reception because each pixel incorporates delays corresponding to different insonification and reception angles.

Therefore, when the ROI is illuminated from a single angle, the focusing is only possible on reception (e.g. CSM). However, when unfocused waves are transmitted at the range of different angles, the focusing can be performed on transmission and reception (e.g. TFM or PWI), to achieve better representation of the ROI. In general, as will be apparent in section 3.6, the wider the range of the transmitted/recorded angles, the better the focusing.

The aim of this chapter is to present the adaptation of the phased array synthetic focusing imaging to pipe GWT together with the necessary theoretical background. Section 3.2 discusses the choice between the time domain and frequency-wavenumber domain. This is followed by the revision of the three chosen classic two-dimensional synthetic focusing imaging algorithms: CSM, PWI and TFM in sections 3.3 and 3.4. Subsequently, the theoretical framework for adaptation of these imaging algorithms to pipe GWT is laid out in section 3.5. The spatial resolution of the reconstruction algorithms and its limitations are discussed in section 3.6. Sections 3.7 and 3.8 present the adaptation of CSM, PWI and TFM to guided waves in pipes. The novel guided wave PWI transduction setup suppressing transmission of the unwanted S0 guided

wave mode in the circumferential direction is introduced in section 3.9. Finally, section 3.10 presents an algorithm to synthesize PWI ultrasonic data from the data collected using the FMC acquisition scheme.

Parts of this chapter have been adapted and extracted from publication [P1], which is available under an open access Creative Common CC BY license hence any part of the article may be reused without permission and publication [P2] which was submitted to IEEE® Transactions on Ultrasonics, Ferroelectrics, and Frequency Control but has not been published at the time of writing this thesis.

3.2. Domain selection

The synthetic focusing imaging techniques can be implemented in either time domain [38,41] or wavenumber–frequency (f-k) domain [43,148-150]. In the time domain imaging, the contributions from each recorded temporal signal are directly mapped to the image domain by the application of delay laws and coherent summation. Hence, the time domain implementations are often referred to as delay-and-sum methods. In the case of f-k imaging, the recorded temporal signals are first transformed to frequency-wavenumber domain using Fourier transform, then the resulting f-k ultrasonic data is mapped (migrated) to the spatial Fourier transform of an object by the application of different mapping methods (e.g. [151,152]). Subsequently the final reconstructed image is obtained using an inverse Fourier Transform [43,153].

The Fourier domain approaches are mathematically more rigorous and, in some cases, offer slight image quality improvement with the computational speed advantage, however, they are much more complex. Their performance depends on selection of an appropriate Fourier interpolator and other imaging parameters [43]. The time domain algorithms offer better stability, flexibility to arbitrary geometries and better performance against material inhomogeneities [149]. Therefore, for the sake of

simplicity, ease, and relevance of comparison of synthetic focusing imaging techniques, the research presented in this thesis uses the time domain heuristic delay-and-sum beamforming implementations of imaging algorithms.

A more in-depth discussion and comparison of time domain and f-k domain approaches can be found in for example [43,149,150].

3.3. Plane wave imaging and common source method in plates

Classic two-dimensional PWI, outlined in Figure 3.1, reconstructs images from the $Q \times N$ matrix of backscattered signals $m_{qj}(t)$ recorded on all the elements of the N transducer array during Q transmission events. In a single transmission event q, all the array elements are excited to generate a plane wave propagating at an angle α_q.

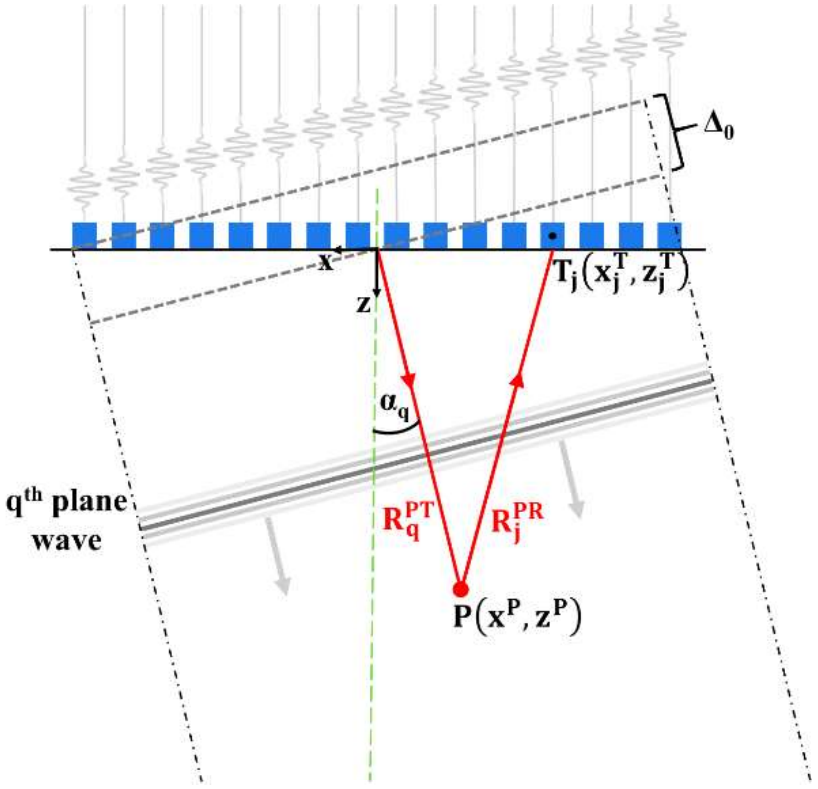

Figure 3.1: The conceptual outline of classic two-dimensional PWI method. R_q^{PT} is the q^{th} incident plane wave travel path to the focus point P, R_j^{PR} is the travel path on reception from P to j^{th} array element T_j, α_q is the plane wave angle and Δ_0 is the correction factor offsetting the excitation to begin at $t = 0$. [P1]

The desired angle of propagation is achieved via application of appropriate delay laws to the transmitted signals. The response recorded after insonification of the region of interest with the q^{th} plane wave is used for synthetic focusing on each pixel of the image on the reception, in the same manner as in the TFM algorithm discussed in the next section. The reconstructions obtained for a range of Q angles are then coherently added to create the final PWI compound image. The intensity of the reconstructed pixel $P(x^P, z^P)$ can be mathematically expressed as [41]:

$$I(P) = \left| \sum_{q=1}^{Q} \sum_{j=1}^{N} h_{qj}^{PWI} \left(\frac{R_q^{PT} + R_j^{PR}}{c} \right) \right|, \tag{3.1}$$

where R_q^{PT} is the q^{th} incident plane wave travel path from the transducer array to the arbitrary focus point P, $R_j^{PR}$is the travel path on reception from the arbitrary focus point to the j^{th} receiving element of the transducer array, h_{qj}^{PWI} is the Hilbert envelope of the $m_{qj}(t)$ signals and c is the wave velocity in the material. The length of the R_q^{PT} path can be found as z' after rotation of the coordinate system by an angle α_q, and the R_j^{PR} as a distance in the Cartesian coordinate system, therefore these are given by:

$$R_q^{PT} = x^P \sin \alpha_q + z^P \cos \alpha_q + \Delta_0, \text{ and} \tag{3.2}$$

$$R_j^{PR} = \sqrt{\left(x^P - x_j^T\right)^2 + \left(z^P - z_j^T\right)^2}, \tag{3.3}$$

where (x_j^T, z_j^T) are the coordinates of j^{th} array element T_j, and Δ_0 is the correction factor offsetting the plane wave excitation to begin at $t = 0$. The Δ_0 can be found geometrically (Figure 3.1) to be:

$$\Delta_0 = \frac{N-1}{2} d_p \sin\left|\alpha_q\right|, \tag{3.4}$$

where d_p is the array pitch distance.

CSM is a special case of PWI with only a single 0° plane wave used for reconstruction and focusing performed only on reception. Hence equation (3.1) applies to CSM.

3.4. Total focusing method in plates

Classic two-dimensional TFM, outlined in Figure 3.2, reconstructs images from an $N \times N$ matrix of backscattered signals $m_{ij}(t)$ recorded for every possible transmitter-receiver pair of the N element phased array. Data acquisition is performed by excitation of a single element at a time and collection of data on all the array elements simultaneously. Such a method of acquisition is referred to as full matrix capture (FMC). In practice, due to reciprocity, the FMC matrix is symmetric, therefore only the lower or upper triangular part of the matrix presented earlier in Figure 1.2(b) needs to be recorded [26].

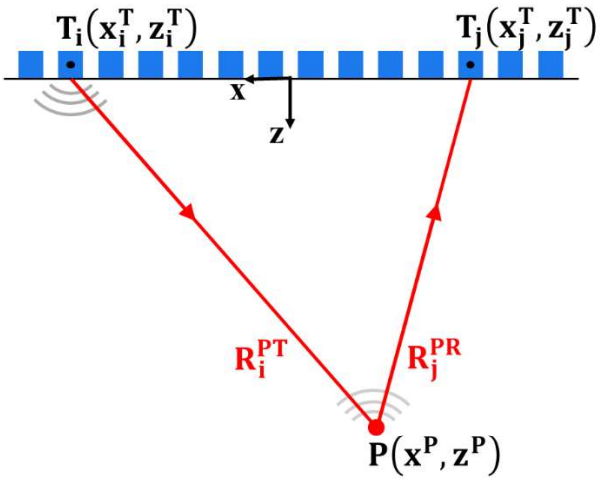

Figure 3.2: The conceptual outline of classic two-dimensional TFM method. R_i^{PT}, R_j^{RT} are the transmission and reception travel paths from the i^{th} transducer T_i to the arbitrary focus point P and from P to j^{th} transducer T_j respectively.

The response recorded during each acquisition event is used for synthetic focusing on each pixel of the image on the reception. Reconstructions obtained for all N acquisition events are then coherently added to create the final TFM image achieving focusing on transmission. The intensity of the reconstructed pixel $P(x^P, z^P)$ is given by:

$$I(P) = \left| \sum_{i=1}^{N} \sum_{j=1}^{N} h_{ij}^{FMC} \left(\frac{R_i^{PT} + R_j^{PR}}{c} \right) \right|, \tag{3.5}$$

where h_{ij}^{FMC} is the Hilbert envelope of the $m_{ij}(t)$ FMC matrix of signals, R_i^{PT}, R_j^{PR} are

the transmission and reception travel paths from the i^{th} transducer to the arbitrary focus point (pixel) $P(x^P, z^P)$ and from pixel P to j^{th} transducer respectively. The lengths of R_i^{PT}, R_j^{PR} paths are distances in the Cartesian coordinate system and they are given by:

$$R_i^{PT} = \sqrt{(x^P - x_i^T)^2 + (z^P - z_i^T)^2}, \text{ and} \tag{3.6}$$

$$R_j^{PR} = \sqrt{\left(x^P - x_j^T\right)^2 + \left(z^P - z_j^T\right)^2}, \tag{3.7}$$

where (x_i^T, z_i^T), (x_j^T, z_j^T) are the coordinates of i^{th} and j^{th} transducers respectively.

3.5. Framework for adaptation of synthetic focusing imaging to pipe guided wave testing

The adaptation of synthetic focusing imaging techniques to pipe GWT is traditionally based on simplification of the analysis of the pipe guided waves to the analogical analysis of plate guided waves in an unwrapped periodic plate [25,58]. As mentioned in section 2.4.4, approximating torsional-flexural pipe guided waves with the SH0 plate guided wave mode requires the continuity of the solution around the pipe circumference, and hence it implies an integer number of wavelengths between the matching wave fronts. As a consequence, at each frequency, plate guided waves corresponding to the pipe guided wave modes are considered to travel at specific discrete helical directions [154] in the pipe with each discrete propagation angle corresponding to a different pipe mode. These angles vary with the wavelength (frequency) to satisfy the continuity boundary condition. The pipe guided wave wavenumber is simply the projection of the SH0 wavenumber in the axial z-direction. Therefore, when the frequency changes, the SH0 angle satisfying the boundary condition changes, and hence, due to trigonometry, the wavenumber in the axial direction corresponding to a pipe guided wave mode also changes. This is the essence

of pipe guided wave dispersion.

Because energy is not created nor destroyed, the SH0 waves transmitted or scattered in the pipe at angles different than those corresponding to pipe guided waves also propagate. Pipe guided wave solutions assume motion of the pipe as a whole, and they do not account for local waves i.e. plate guided waves that exist in the pipe which is a plate-like structure.

This thesis proposes a new, different approach to guided wave synthetic focusing imaging. The focus here is on short range GWT, which allows further simplification of the guided wave problem by looking at local (plate) solutions, instead of global (pipe) solutions. The proposed adaptation is also based on plate/pipe guided wave analogy. However, here the solutions do not have to be continuous around the pipe circumference, and hence there is no need for the extra boundary condition. The pipe is treated as a continuous infinite plate in which the angles for transmission and back propagation of SH0 mode are not restricted to discrete pipe guided wave mode angles. This reduces the number of modes considered for imaging to a single fundamental shear horizontal mode, and hence it simplifies the algorithm. The broader range of transmission/reception angles allows for utilisation of a wider range of spatial frequencies for imaging, which is advantageous, as will be discussed in the subsequent section. Furthermore, the dispersion does not have to be accounted for as only the non-dispersive SH0 mode in the direction of its propagation is considered.

Therefore, the adaptation of synthetic focusing imaging techniques presented in this chapter follows the approach proposed in this section.

3.6. Spatial resolution and its limitations

The key performance indicators typically used to assess imaging methods include spatial resolution and SNR. The spatial resolution is defined as the minimum distance at which the two neighbouring features can be resolved (i.e. distinguished) in the reconstructed image [155].

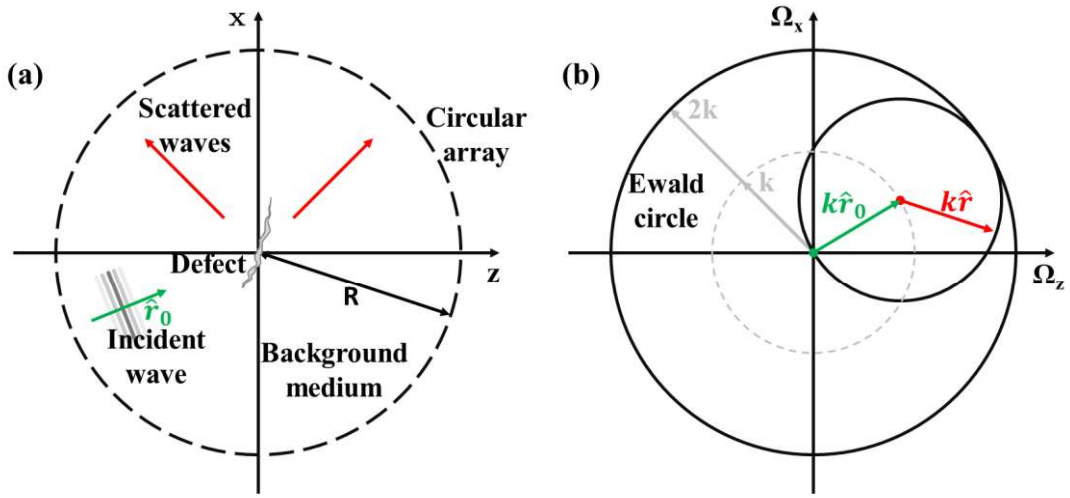

Figure 3.3: (a) Outline of a full-view ultrasonic array configuration allowing illumination of the ROI from all angles around 360° and reception of scattered waves in all directions; (b) Diagram showing how the scattered field measured in the direction $\hat{\mathbf{r}}$ after illumination of the ROI with an incident plane wave from direction $\hat{\mathbf{r}}_0$ is mapped onto the two-dimensional k-space. $k = \frac{2\pi f}{c}$ is a wave number, where f is temporal frequency and c is wave velocity in the material.

In the ideal case of the two-dimensional ultrasonic imaging setup, all the points contained within the ROI are illuminated with waves transmitted from all the angles around 360° and scattered waves are also recorded in all directions [156-159]. An example of such imaging setup with a circular array fully encircling the ROI is presented in Figure 3.3(a). The transmission and reception angles together with the frequency of the probing waves determine which spatial frequencies are available for imaging of each point within the ROI. The spatial frequency components available for imaging are typically plotted in the two dimensional Fourier space referred to as k-space [160]. Figure 3.3(b) outlines how recorded data is mapped onto the k-space diagram with the incident wavenumber and direction represented by a green arrow and direction and

wavenumber of the recorded scattered wave represented by a red arrow. The perfect imaging system transmitting and recording waves in all directions allows population of the entire spatial frequency domain within the Ewald limiting circle [147], assuming the system provides sufficient temporal and spatial sampling. Therefore, only spatial frequencies up to $2k_0$ where k_0 is the wavenumber of the probing wave can be retrieved through ultrasonic imaging [147,161].

As shown in [162], this leads to the classical resolution limit of $\lambda_0/2$, known as the diffraction limit [157,162,163]. According to this limit, details smaller than half the smallest probing wavelength cannot be retrieved during reconstruction. This exhibits in the reconstructed image as blurring because details finer than the resolution cannot be resolved.

During the reconstruction process, the ROI is discretised into the grid of points (pixels). Each point is treated as an infinitesimal scatterer. The synthetic focusing algorithms considered in this thesis neglect any interactions of the propagating waves with other scatterers present in the medium. Such an approach is based on the Born approximation [147,164] which is typically used in most of the synthetic focusing and tomographic reconstructions [26,38,41,83,161,165-167]. This approximation assumes that the distortion of waves propagating through the domain is negligible and hence it is not accounted for. The pipes considered in this thesis are homogenous and isotropic, therefore such an assumption is valid.

The Born approximation assumes an acoustic scattering model, in which the scattering is omnidirectional. However, as shown in [168], guided waves scatter in an elastic fashion. The elastic scattering of the SH0 wave mode was shown to have a directional profile [113-115]. While the elastic scattering regime does not match the acoustic scattering model assumed in the Born approximation, the mismatch does not make imaging using Born approximation invalid. It does, however, lead to limited scattering

angular range and consequently to retrieval of a reduced range of spatial frequencies from each acquisition event. This in turn translates to a reduced resolution in the reconstructed image beyond the fundamental diffraction limit.

Therefore, the half a wavelength resolution limit is a theoretical limit rather than a practically attainable resolution. In practice, besides the limited scattering angles, the resolution is further reduced by many practical aspects such as limited view array geometry, which is typical in most practical guided wave testing implementations, limited transducer transmission/reception angles and coherent noise considerations.

A typical pipe guided wave inspection is a limited view problem i.e. the linear array of elements, in the form of a fully circumferential ring of transducers, transmits and receives waves only on one side of the ROI as outlined in Figure 3.4. In this setup, only backscattered waves are readily available for imaging and the domain is illuminated with a limited range of angles. As a consequence, as shown in [147,169], only high frequency parts of the k-space are available for imaging. These encode edges and relatively small, sharp material discontinuities such as for example cracks, which are the main concern in this thesis. The unavailable low frequency components, which are located in the central region of the k-space plot, can only be recorded from the waves transmitted through the ROI [147,169,170] or using highly broadband excitation [26] (which is problematic in practical implementations). These frequencies encode information on gradual geometrical changes and large, smoothly varying features, which are of lesser importance in structural imaging and hence they are not of interest here. The lack of lower frequencies does not have a negative impact on the maximum achievable resolution, as in the simple sense, the higher the spatial frequencies are available for imaging, the better the spatial resolution of the final image. Therefore, reconstructions based on backscattered waves can achieve high resolution close to the theoretical diffraction limit [38,58].

The pipe is a closed geometry hence a fully circumferential transducer array acts as a virtually infinite aperture [58]. Consequently, the ROI can be illuminated with a wide angular range of waves up to +/- 90°, and all the backscattered waves will eventually reach the array. Therefore, in theory, it is possible to populate half of the Ewald limiting circle in k-space without the low frequency part (the lowest frequencies in the half-circle could only be populated using a broadband excitation in this configuration). However, as discussed earlier, the angular range of the transmitted and the recorded waves has some practical limitations, hence only limited sections of the half disc can be determined from the measurements.

In the case of the limited-view linear phased arrays, the two orthogonal directions of spatial resolution are typically considered separately. These are axial resolution, in the z-direction perpendicular to the array and the lateral resolution, in the x-direction parallel to the array. The distinction is performed because the resolution in each of these directions depends on the different parameters of the linear phased array imaging system.

The axial resolution is primarily dependent on spatial pulse length (SPL) [155], which is the length that the pulse occupies in space and hence it is the product of the probing wavelength and the number of cycles in the pulse. In pipe GWT a narrowband excitation is desired to achieve high centre frequency of the probing wave without the excitation of the unwanted higher order guided wave modes. Such narrowband excitation is achieved by the use of a larger number of cycles in the tone burst excitation compared to conventional bulk wave ultrasonic testing. In the project presented in this thesis, a 5-cycle Hann windowed tone burst excitation is used as a compromise between the reasonably short SPL and the narrow frequency bandwidth. Because SPL is fixed here, the axial resolution is the same for all the considered imaging algorithms, hence it is of lesser interest in this thesis. This project focuses on

the lateral resolution because the application interest is the length of circumferentially oriented cracks. The lateral resolution greatly depends on the insonification and the reception angular ranges, and hence it is a good indication of the performance of the imaging methods.

3.7. Adaptation of plane wave imaging and common source method to pipe guided wave testing

The main difference between the classic two-dimensional PWI and its pipe adaptation is that the pipe wall is a closed geometry. The waves on transmission and reception travel around the pipe in helical paths as presented in Figure 3.4. The concept of helical travel paths was introduced in [154].

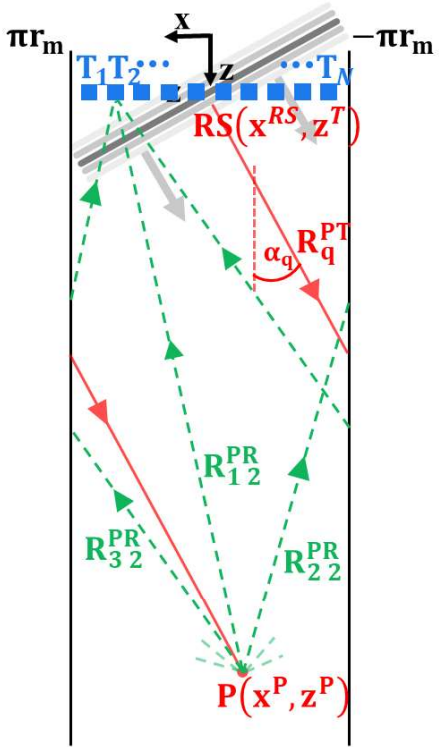

Figure 3.4: Schematic diagram of pipe PWI showing helical paths along which guided waves are travelling to and from a focusing point P for a q^{th} plane wave sent at an angle α_q. RS is the start of the incident wave travel path to the arbitrary point P, r_m is the mean radius of the pipe, R_{mj}^{PR} is the travel path from P to the j^{th} transducer T_j via m^{th} order helical path and R_q^{PT} is the q^{th} incident plane wave travel path to the focus point P. [P1]

As a consequence of using signal contributions that have travelled through the pipe

via different helical paths, the final reconstructed image in the pipe implementation of PWI is a coherent summation of reconstructions assuming each helical path. Therefore, an additional summation has to be added to the classic PWI equation (3.1) to describe image intensity of pixel P in pipe guided wave PWI, as follows:

$$I(P) = \left| \sum_{m=1}^{M} \sum_{q=1}^{Q} \sum_{j=1}^{N} h_{qj}^{PWI}\left(\frac{R_q^{PT} + R_{mj}^{PR}}{c}\right) \right|, \tag{3.8}$$

where M is the number of helical paths used for reconstruction and R_{mj}^{PR} is the travel path from the focus point to the j^{th} transducer via m^{th} order helical path (see Figure 3.4 for helical path numbering). R_{mj}^{PR} is given by:

$$R_{mj}^{PR} = \sqrt{\left(-(-1)^m \times \left|x^P - x_j^T\right| + \left\lfloor \frac{m}{2} \right\rfloor \times circ_m\right)^2 + \left(z^P - z_j^T\right)^2}, \tag{3.9}$$

where (x_j^T, z_j^T) are the coordinates of j^{th} array element T_j, (x^P, z^P) are the coordinates of an arbitrary focusing point P, $circ_m = 2\pi r_m$ is the mean circumference of the pipe, r_m is the mean radius of the pipe and m is the order of the helical path.

Similarly to the travel paths on reception, the incident plane waves on transmission travel in the helical paths along the pipe as outlined in Figure 3.4. The helical path angle with the axis of the pipe depends on the plane wave angle α_q. The incident wave travel path R_q^{PT} to point P can be expressed as:

$$R_q^{PT} = \frac{z^P - z^T}{\cos \alpha_q} + \Delta_0, \tag{3.10}$$

where z^T is the axial position of the transducers ($z^T = z_1^T = z_2^T = \cdots = z_N^T$) and Δ_0 is the correction factor offsetting the plane wave excitation to begin at $t = 0$. Δ_0 can be geometrically found as:

$$\Delta_0 = \begin{cases} (x^{RS} - x_N^T) \sin \alpha_q & for \quad \alpha_q < 0 \\ (x^{RS} - x_1^T) \sin \alpha_q & for \quad \alpha_q \geq 0 \end{cases}, \tag{3.11}$$

where x^{RS} is the x coordinate of the start of the incident wave travel path to the

focusing point. For the ease of calculation, it is assumed that a continuous plane wave forms immediately at the transducer array. x^{RS} can be expressed as:

$$x^{RS} = \begin{cases} sgn(\alpha_q)\,(2\pi r_m - X_E) + x^P & when \quad X_E > \pi r_m + sgn(\alpha_q)\,x^P \\ x^P - sgn(\alpha_q)\,X_E & when \quad X_E \leq \pi r_m + sgn(\alpha_q)\,x^P, \end{cases} \tag{3.12}$$

where X_E is the relative position in the x (circumferential) direction of the pixel P with respect to the starting position of the incident ray path (RS in Figure 3.4) through which the incident wave travels to this point P. Therefore, X_E is effectively the length of the incident travel path projection in the circumferential direction minus the full pipe circumference repetitions. This accounts for the number of times the signal travelled around the pipe before reaching pixel P. There are two possible cases of X_E outlined in Figure 3.5 with red and green colours. Mathematically X_E can be expressed as:

$$X_E = \left|(z^P - z^T)\,tan\,\alpha_q\right| - f_c, \tag{3.13}$$

where $f_c = \left\lfloor \frac{\left|\tan\alpha_q(z^P - z^T)\right|}{2\pi r_m} \right\rfloor 2\pi r_m$ subtracts full pipe circumference repetitions.

Unlike classic two-dimensional PWI where only a single direct ray path on reception from the focus point to the j^{th} receiving element of the transducer array needs to be considered, here, in theory, there are infinitely many direct ray paths. All the backscattered signals from any point in the pipe will eventually reach the fully circumferential transducer array. This results in a virtually infinite aperture of the fully circumferential array. Additionally, each incident plane wave covers the entire interrogated area. This prevents the situation where the steering angle of a plane wave is out of range of the geometrical angles between the end array elements and an arbitrary reconstruction point which could lead to artefacts in the final image [43,49]. All this makes the pipe a powerful platform for performance comparison of synthetic focusing imaging techniques, as recording the full angular range of backscattered waves allows the highest possible resolution to be achieved [49]. In practice, as discussed in

the previous section, SH0 has limited scattering angles [58] and higher order helical path signals tend to contain more coherent and incoherent noise with respect to potential defect signals. Higher noise degrades the image quality. Therefore, the selection of a maximum helical path order used for reconstruction is a fine balance between the increase in resolution and decrease in SNR. Finding the optimal imaging parameters for the best image quality and fair comparison of imaging methods will be covered later in section 4.5.

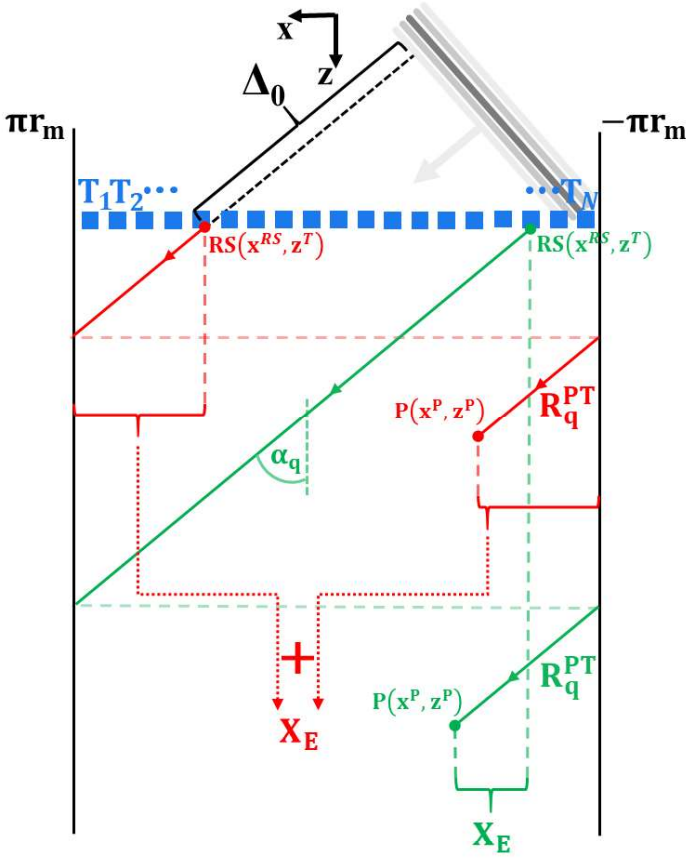

Figure 3.5: Outline of two cases of incident plane wave travel paths to focusing point P for a q^{th} plane wave sent at an angle α_q. R_q^{PT} is the incident wave travel path to P, RS is the start of this path at the array, array element T_j is j^{th} array element, r_m is the mean radius of the pipe, X_E is the length of the incident travel path projection in the circumferential direction minus the full pipe circumference repetitions accounting for the number of times the signal travelled around the pipe before reaching pixel P, and Δ_0 is the correction factor offsetting the excitation to begin at t = 0. [P1]

As mentioned earlier, CSM is a special case of PWI with only a single 0° plane wave transmission, therefore equation (3.8) is also used for CSM reconstructions. It is currently the most popular technique for pipe guided wave synthetic focusing imaging,

because of its simplicity, short acquisition with only one transmission event and great coherent and incoherent SNR in GWT applications [60]. Hence, CSM results will be treated as a baseline for the comparison of other synthetic focusing imaging methods in the present study.

3.8. Adaptation of total focusing to pipe guided wave testing

TFM can also be adapted to pipe GWT using the simplified plate/pipe analogy. In the FMC acquisition, array elements are typically treated as omnidirectional point sources for simplicity. This means that the incident wave propagates in a wide range of angles forming a circular pattern around the source element. Signals travel via different helical paths inclined at a range of angles between arbitrary point P and i^{th} transmitting and j^{th} receiving array elements. The intensity of the reconstructed pixel $P(x^P, z^P)$ can be calculated using the following equation:

$$I(P) = \left| \sum_{m_T=1}^{M} \sum_{m_R=1}^{M} \sum_{i=1}^{N} \sum_{j=1}^{N} h_{ij}^{FMC} \left(\frac{R_{m_T i}^{PT} + R_{m_R j}^{PR}}{c} \right) \right|, \tag{3.14}$$

where $R_{m_T i}^{PT}$, $R_{m_R j}^{PR}$ are transmission/reception travel paths from i^{th} transducer to the reconstructed pixel P and from P to j^{th} transducer respectively, and m_T and m_R are helical path orders on transmission/reception respectively. The incident and scattered wave travel paths can be calculated using equation (3.9) and their geometrical representation is analogical to the helical paths on reception in PWI marked with a green colour in Figure 3.4.

Analogically to PWI, in theory, there are infinitely many helical paths to consider in TFM. However, practically, the SH0 scattering angles are limited, and the transducers are not omnidirectional and their true angular transmission/reception range is typically

around $-\pi/4$ to $\pi/4$ [58]. This limits the number of helical paths usable for reconstruction. This results in the same trade-off between the resolution and the SNR, as was discussed in the case of PWI. Therefore, the optimal number of helical paths providing the best image quality will be investigated in section 4.5 to provide a fair comparison of the imaging methods.

Unlike PWI, in TFM the angular range of transmitted waves cannot be conveniently controlled. To achieve comparable resolution and SNR to PWI, and to remove the circumferential guided wave artefacts mentioned in [60] and [171], the waves travelling at angles higher than the desired angular range need to be filtered out in the two-dimensional spatial frequency domain from the recorded FMC time traces, prior to performing reconstruction. This can be achieved using the frequency mask removing spatial components of waves at angles larger than the desired cut-off angle α_{cf} as outlined in Figure 3.6. A gradual transition region between the full pass and the total removal of the spatial frequency components is introduced to avoid sharp changes leading to strong 'ringing' artefacts [172].

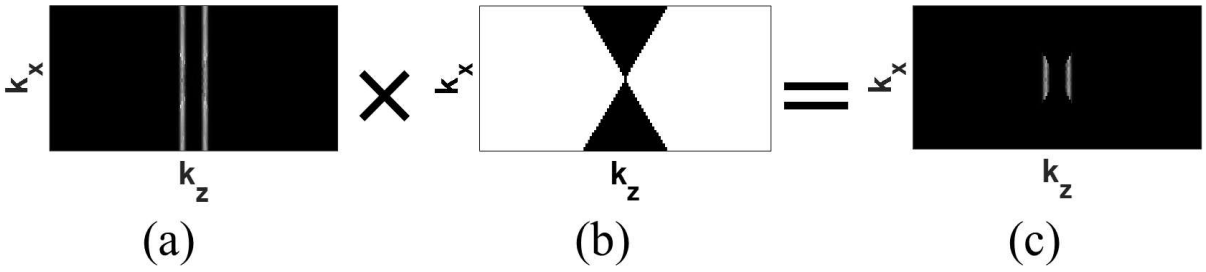

Figure 3.6: Spatial filtering of recorded time traces which removes waves travelling at higher angles; (a) original signal after two-dimensional FFT, (b) spatial frequency mask removing waves at angles larger than α_{cf} and (c) Fourier domain signal after filtering. [P1]

The selection of appropriate cut-off angle α_{cf} will be discussed in section 4.5 alongside a discussion on selection of other imaging parameters.

3.9. S0-cancelling guided wave PWI transduction setup

The project presented in this thesis is concerned with imaging using SH0 waves. In pipe guided wave testing these waves are typically excited using shear contact transducers [119]. This type of transducer simultaneously excites two modes – the desired SH0 mode, and the unwanted S0 guided wave mode in the direction parallel to the SH0 particle motion [58,60]. Unwanted modes are a form of coherent noise. Their presence can result in artefacts and decreased SNR in the reconstructed images.

Generation of the incident wave containing only a single desired wave mode is very challenging. This is overcome in the CSM method by using a single SH0 plane wave at 0° (T(0,1) mode), but at the cost of decreased resolution to around 1.5 wavelengths [25], compared to the 0.5 wavelengths theoretically achievable by TFM and PWI. While research attention has been devoted to the suppression of the resulting coherent noise in pipe guided wave TFM (e.g. [171]), PWI has not yet been implemented in pipe GWT. Here the focus is on development of a novel PWI transduction setup which allows unwanted S0 mode suppression.

Simple application of delay laws to excite the SH0 plane wave at an angle α using array elements oriented in the circumferential direction inevitably creates an additional unwanted S0 plane wave at angle β as illustrated in Figure 3.7(a). The unwanted plane wave can result in artefacts in the reconstructed images because the S0 mode travels around 70 % faster than SH0 mode. Adding a second array in which elements oriented in the axial direction are positioned between the elements of the primary transducer array, as outlined in Figure 3.7(b), provides capability for modal control. The secondary array which transmits signals 180° out of phase with respect to the primary array elements is used to excite the S0 wave. When the appropriate amplitude weighting coefficient is established for the secondary array the destructive interference

between the transmitted S0 wave from the primary array and the phase-inverted wave transmitted by the secondary array can be achieved to cancel out the unwanted S0 plane wave inevitably excited by the primary array.

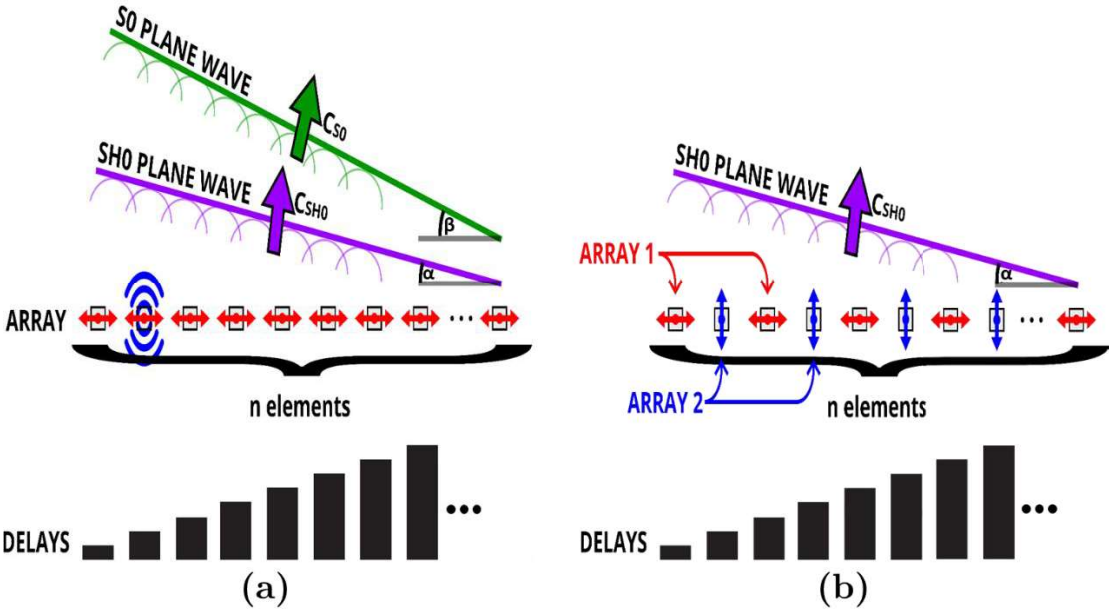

Figure 3.7: SH0 guided wave mode plane wave excitation using (a) classic transduction setup, and (b) S0 mode cancelling transduction setup. α, β are SH0 and S0 plane wave angles respectively, c_{SH0} and c_{S0} are SH0 and S0 wave mode velocities respectively. [P1]

This weighting coefficient can be found by the simplified vector analysis presented in Figure 3.8, where the $S0_{PW}$ vector represents the resulting S0 plane wave which will be suppressed, $S0_{Arr.1}$ is the contribution from the circumferentially oriented primary array and $S0_{Arr.2}$ is the contribution from the axially oriented cancelling array. $S0_{Arr.2}$ is defined as:

$$|S0_{Arr.2}| = w \times |S0_{Arr.1}|, \tag{3.15}$$

where w is the amplitude weighting coefficient. To suppress the unwanted S0 plane wave, contributions from two arrays have to cancel out. Since signals excited on both arrays are 180° out of phase with respect to each other, their contributions in direction β of the S0 plane wave have to be identical i.e.

$$\cos(90° - \beta) \times |S0_{Arr.1}| - w \times \cos(\beta) \times |S0_{Arr.1}| = 0, \tag{3.16}$$

Hence, this weighting coefficient is:

$$w = \tan\beta, \tag{3.17}$$

where the angle of the S0 plane wave is given as:

$$\beta = arcsin\left(\frac{\Delta t\, c_{S0}}{d_p}\right), \tag{3.18}$$

Δt is the time between excitation of the consecutive array elements given by delay laws, d_p is pitch distance and c_{S0} is the S0 wave speed. The SH0 mode excited in the circumferential direction by the secondary array does not constructively interact to create the shock wave within the array angular transmission range nor can it be received on elements of the primary array oriented circumferentially. The S0 suppression algorithm is only needed for an SH0 angular range between –36.6° and 36.6° because beyond this angle range the real part of β is 90° and hence the weighting coefficient is zero.

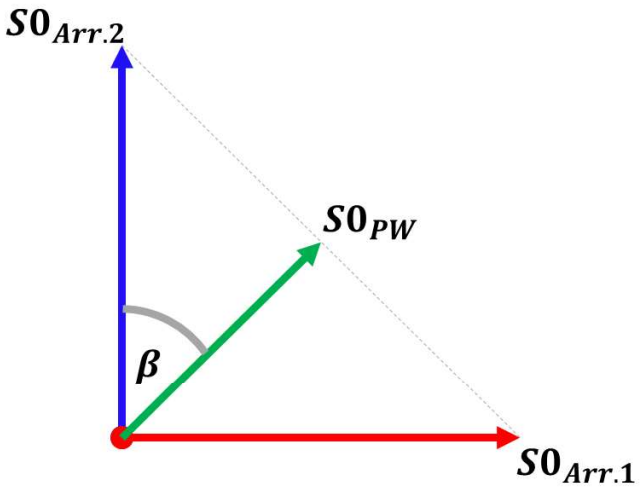

Figure 3.8: Simplified vector analysis of S0 contributions from primary and secondary phased arrays.

3.10. Plane wave imaging using full matrix capture data

Classic PWI is a method of data acquisition and a reconstruction algorithm. It is possible to synthesize ultrasonic datasets for PWI reconstruction algorithm from the data acquired using FMC acquisition by application of appropriate delays to each response matrix constituting the FMC dataset [43]. This can be achieved via the

following transformation:

$$h_{qj}^{FMCPWI} = \begin{cases} \sum_{i}^{N} h_{ij}^{FMC}\left(t - \frac{(i-1)d_p}{c} sin|\alpha_q|\right) & when \quad \alpha_q \geq 0 \\ \sum_{i}^{N} h_{ij}^{FMC}\left(t - \frac{(N-i)d_p}{c} sin|\alpha_q|\right) & when \quad \alpha_q < 0 \end{cases} . \tag{3.19}$$

In this thesis, the PWI algorithm applied to a plane wave response dataset synthesised from the FMC data is referred to as FMCPWI to distinguish from the classic PWI implementation. It provides a convenient platform for the comparison of TFM and PWI reconstruction algorithms as well as FMC and PWI data acquisition schemes. The reconstruction algorithm in FMCPWI remains unchanged from that of the pipe guided wave PWI and is given in equation (3.8).

3.11. Summary

In this chapter phased array synthetic focusing imaging algorithms, CSM, TFM and PWI, which will be used throughout this thesis, were adapted to pipe GWT using the fundamental SH0 guided wave mode. The adaptation was based on the plate-pipe analogy in which analysis of guided waves in pipe is approximated by analogical analysis of guided waves in an unwrapped infinite periodic plate. The proposed adaptation of the imaging algorithms uses the local plate guided wave solutions instead of typically used global pipe guided wave solutions. This allowed for simplification of the imaging algorithms. The chapter discussed spatial resolution and its limitations in the context of guided wave phased array synthetic focusing imaging. The k-space filtering scheme was proposed to eliminate the coherent noise caused by the presence of the S0 guided wave mode in the FMC ultrasonic data, which was reported in the literature to corrupt the TFM reconstructions. Subsequently, the novel PWI transduction setup was introduced to suppress the transmission of the unwanted S0 mode during PWI acquisition, to improve coherent SNR. Finally, an algorithm

transforming FMC data into ultrasonic data corresponding to PWI acquisition was presented.

4. Comparison and evaluation of the performance of the SH0 guided wave synthetic focusing imaging methods in pipes

4.1. Introduction

The previous chapter adapted four common synthetic focusing imaging methods, CSM, PWI, FMCPWI and TFM to pipe GWT using the fundamental SH0 mode. The aim of this chapter is to establish their optimal implementation to inspection of pipes and to present the proof of concept that TFM, FMCPWI and PWI can be deployed in similar fashion to state-of-the-art CSM. The objective is to evaluate and compare their performance using FE and experimental studies.

Section 4.2 introduces methodology used for the lateral resolution and SNR measurements from the reconstructed images. The FE model used for numerical simulations is described in section 4.3. This is followed by a discussion on the experimental setup in section 4.4. Subsequently, section 4.5 presents the FE study on selection of the optimal imaging parameters used in the remainder of this thesis. The resolution and defect sizing accuracy of considered imaging methods are evaluated and compared in section 4.6. This is followed by the analysis of SNR of all the considered methods in section 4.7. Next, section 4.8 discusses the potential for crack through wall thickness depth estimation from the PWI reconstructions. In section 4.9 the performance of the transduction setup suppressing the unwanted S0 mode is evaluated. A discussion on generalisation of the presented results for different axial positions of a crack, different frequencies and pipe diameters is conducted in section 4.10. Finally, the chapter is summarised in section 4.11.

Parts of this chapter have been adapted and extracted from publication [P1], which is available under an open access Creative Common CC BY license hence any part of the article may be reused without the need for permission.

4.2. Methodology of resolution and SNR measurements

As was mentioned in section 3.6, the key performance indicators for imaging methods include spatial resolution and SNR, and these are of interest here.

Ability to correctly size the defect is tightly related to the resolution. When the crack is small with relation to the wavelength, it acts as a point scatterer and its indication is essentially a PSF, which is often used to assess the resolution [33,38]. By measuring the lateral size of the known defect from the reconstructed image and comparing results with true dimensions lateral resolution can be estimated. Here, crack lateral sizes were estimated using a full width at half maximum (FWHM) method, i.e. taking the size as being the distance between the two points where the image intensity has dropped to

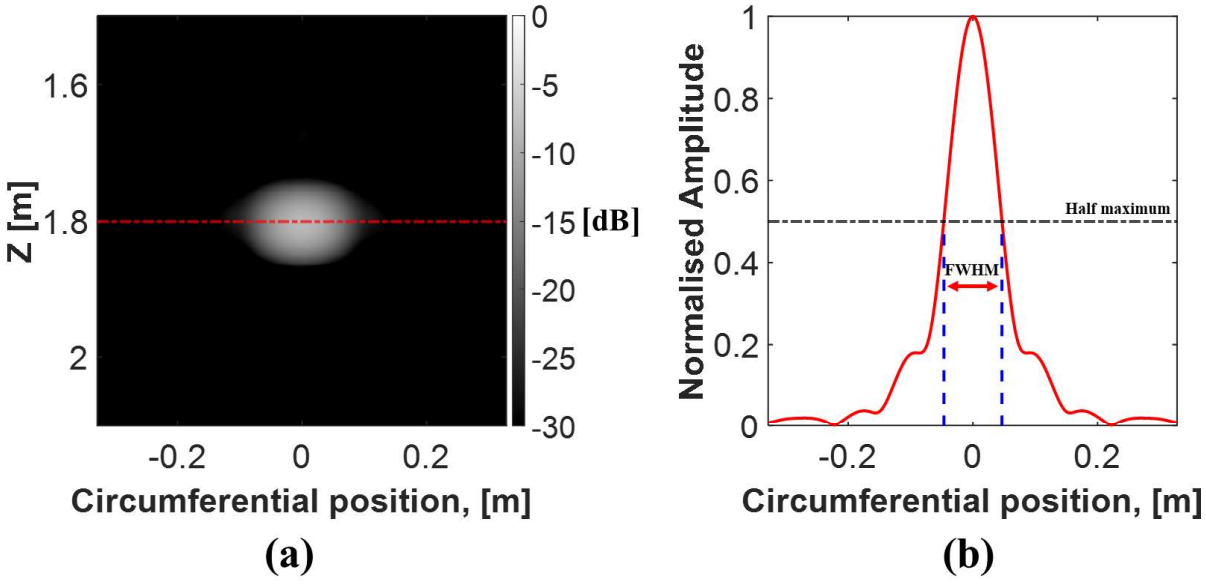

Figure 4.1: (a) An example CSM reconstruction of zero volume outer surface breaking 2.1 λ_{SH0} long 75 % through wall thickness deep planar crack oriented perpendicular to the axial z-direction at 1.8 m away from the ring transduction array. Reconstruction was based on the FE data. (b) Circumferential amplitude distribution along the dashed red line in (a) at crack position. The red arrow presents the measured crack length using FWHM method.

50 % of the peak [25,34,55]. The method is outlined in Figure 4.1. The defect lateral size at which its indication in the reconstructed image starts to resemble a point scatterer, i.e. indication size stops decreasing with further decrease of the lateral extent of a defect, reveals the maximum achievable resolution.

In the presented study SNR is defined as the ratio of the peak defect indication (I_{PDI}) to the root mean square (RMS) of the background noise (I_{NRMS}) in the section of the pipe preceding a defect between 1.1 m and 1.4 m (see Figure 4.2 in section 4.3) with respect to axial position of an array (see equation (4.1)). This specific area was chosen because it does not include any artefacts caused by reflections of other modes from a defect and does not include dead zone artefacts near the transduction array in the experiments.

$$SNR = 20\, log_{10} \frac{I_{PDI}}{I_{NRMS}} \tag{4.1}$$

4.3. Finite element model

The finite element method (FEM) is a well-established numerical method for approximate solution of boundary value problems in engineering [173]. The FEM discretises a model representing the structure into small finite elements. Each individual element can be treated as a small piece of the structure in which a field quantity (e.g. displacement, acceleration, stress etc.) is allowed to have a simple spatial variation. This spatial variation is represented by a simple equation. By assembling all the elementary equations into a system of equations and by solving this system of equations, an approximation of the physical phenomena in the entire structure is achieved [65]. The accuracy of the approximation can be conveniently increased by the increase in number of the finite elements used in the model.

Finding an exact closed form solution to the elastic wave propagation problem in

complex geometries is difficult and often impossible, hence numerical methods are typically employed to find approximate solutions [65]. Since elastic wave propagation is a boundary value problem, the FEM is well-suited for numerically solving these types of problems. The FEM has been widely used in modelling of guided wave propagation and the agreement of the approximate results with experimental data have been successfully validated for a large number of guided wave problems [22,23,81,106,113,120,126,143,174-180]. Therefore, this method was also chosen for numerical modelling in the project presented in this thesis.

The FEM time domain solution can be achieved with implicit or explicit solving schemes. In implicit schemes the field variables at each subsequent time step are calculated from their values at the current step and the subsequent step via coupled equations [181-183]. Therefore, each time step requires solving a matrix equation. For linear problems, this is simply performed via matrix inversion which is memory and computationally intensive for larger models. Solving the non-linear problems requires an iterative time integration scheme which further decreases the computational efficiency.

On the other hand, in the explicit schemes the field variables of each subsequent step are explicitly calculated from their known values at previous time steps [182], which is more computationally efficient. Therefore, for time domain wave propagation problems, the explicit solving schemes are preferred. Implicit schemes were rendered unattractive for solving time domain wave propagation problems due to their inefficiency [182,184]. Although it is important to note that implicit schemes are unconditionally stable, which means that the accuracy of the solution does not depend on the time step (though time step has to be sufficiently small to provide sufficient temporal sampling in the considered bandwidth) [183]. In contrast, stability of explicit schemes depends on the size of the selected time step in relation to the smallest element

size in the model. The stability criterion for explicit schemes is given by [183]:

$$\Delta t \leq \Delta t_{cr} = \frac{\Delta L_{min}}{c_0}, \tag{4.2}$$

where Δt is selected time step, Δt_{cr} is the critical time step above which the scheme becomes unstable, ΔL_{min} is the smallest nodal distance in the mesh and c_0 is the velocity of the fastest propagating wave. Hence, the selected time step must be smaller than the critical time step given by (4.2) to maintain stability. For a broader discussion on implicit and explicit schemes please refer to [181,182].

To reduce computational times, it is often possible to reduce the size of the three dimensional model by using a symmetric boundary condition or by simplifying the problem into an analogical quasi two dimensional model (e.g. simulation of Lamb wave interaction with defects using simplified two dimensional models with the assumption of plane strain [23,174,185,186], representing the pipe as a three-dimensional membrane FE model with a symmetric boundary [126]). However, in this thesis, part-circumferential part-depth cracks in pipes are of interest and non-axisymmetric excitation is investigated, therefore, a full three dimensional model needs to be utilised. The three dimensional models are substantially larger compared to similar two dimensional ones, therefore an efficient FE software is desired. Here, Pogo, the explicit time domain finite element (FE) solver developed at Imperial College London [187], was used for solving the FE models. The Pogo software was chosen because it utilises parallelisation and graphical processing unit (GPU) acceleration to achieve solving times around 100 – 200 times faster (depending on the hardware configuration) compared to the popular commercial software, Abaqus, which only uses a central processing unit (CPU).

The three dimensional FE model (see Figure 4.2) used in the EngD project represented a standard 8 inch nominal diameter schedule 60 ASTM A106-B steel pipe later used

in the laboratory experiment. The pipe had wall thickness of 10.8 mm and mean diameter of 209.1 mm. The material properties in the model were set as follows: Young's modulus, $E = 210$ GPa, shear modulus, $G = 80$ GPa and density, $\rho = 7932$ kg/m^3. The selected element type was a general purpose linear brick element, C3D8R, with reduced integration and three translational degrees of freedom per node. The FE model had a structured mesh with a minimum of 30 elements per SH0 wavelength ($\lambda_{SH0} \approx 63.5$ mm) in any direction. The 30 elements per wavelength was chosen because in the comprehensive study on FE modelling of ultrasonic waves in elastic media [184], Drozdz, showed that such dense element mesh results in phase velocity errors close to zero percent regardless of the selected time step, provided it is smaller than the critical time step required for stability of the model. According to the same study, mesh density of at least 25 elements per wavelength is required for accurate modelling of ultrasonic wave reflection from subwavelength cracks which will be investigated in this project. The denser the mesh, the more accurate the FEM approximation, and therefore the mesh density used in this study with 30 elements per wavelength provides negligible errors of the approximation.

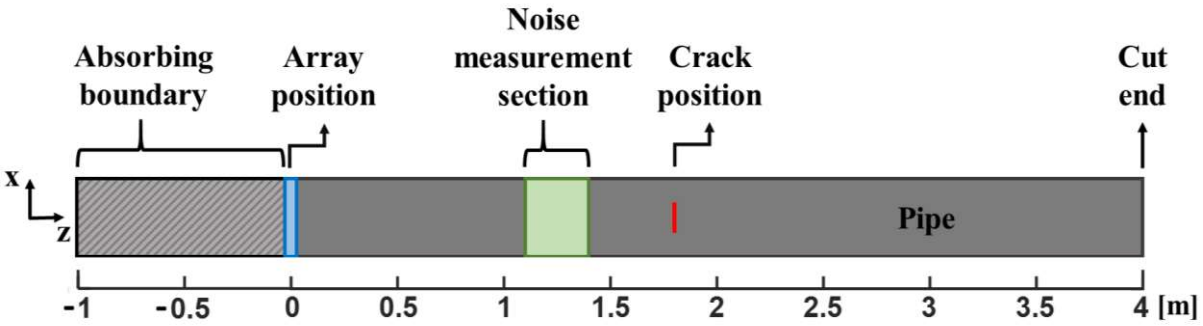

Figure 4.2: FE pipe model layout.

There were 328 elements modelled around the pipe circumference with the average element length of 2.0 mm (32 elements per wavelength), 12 elements through the wall thickness resulting in the element length of 0.9 mm (71 elements per wavelength) in the radial direction and the element length in the axial direction was also 2.0 mm (32

elements per wavelength).

As discussed, the model used an explicit solving scheme, hence the time step was dictated by the critical time step requirement. Here, a conservative time step of 7.3615×10^{-8} s was used, which is a half of the required critical time step.

The pipe was modelled to be 5 m long with the phased array position offset from the pipe end by 1 m. The area between the array position and the closest cut end of the pipe acted as an absorbing boundary. The stiffness reduction method (SRM) [188] was used in this section of the pipe. It was implemented by increasing the mass proportional damping coefficient from 0 to 314159.3 according to a cubic power law. Simultaneously, the stiffness of the subsequent elements towards the cut-end of the pipe in the negative z-direction was reduced by decreasing the Young's modulus from $E = 210$ GPa (parent material) to $E = 2.1$ GPa using an exponential decay function containing a variable attenuation factor as described in [188]. This resulted in the suppression of waves propagating in the negative axial direction so that there were no spurious reflections introducing unwanted features into the reconstructed image. The SRM was chosen because it outperforms absorbing layers by increasing damping (ALID) method [189-192] and it does not require specific programming and functionality of the FE package as the perfectly matched layers (PMLs) method does [193-195]. At least 1.5 wavelengths of the probing wave is required for the SRM to perform sufficiently, and the performance of the method increases with the length of the absorbing section of the model. In the model, an overly conservative 15.8 wavelength (1 m) long absorbing layer was used so that residual signals reflected from the cut-end on the negative z-direction side of the pipe are negligible.

The 40 element fully circumferential ring phased array of equally spaced shear contact transducers was modelled by selecting nodes on the outer surface of the pipe which lie within the area approximately equal to the real contact area of the transducers in the

experiments. The ultrasonic waves were excited by application of force to these nodes in the tangential direction. The circumferential pitch distance on the surface was 17.3 mm which is well below $\lambda_{SH0}/2$ to ensure it is fully sampled to avoid grating artefacts.

One of the main aims of this project is to evaluate and compare the lateral resolution and the accuracy of the lateral crack size representation in the images reconstructed using different synthetic focusing imaging methods. Therefore, zero volume outer surface breaking planar cracks extending in the circumferential direction were modelled by disconnecting the adjacent elements in the pipe wall at 1.8 m away from the phased array position as presented in Figure 4.3. Because the study is concerned with zero volume cracks, the crack width w was set to zero. Simulations of cracks by disconnecting adjacent elements were widely studied, used and experimentally validated in a wide range of publications (e.g. [23,25,185,186,196]).

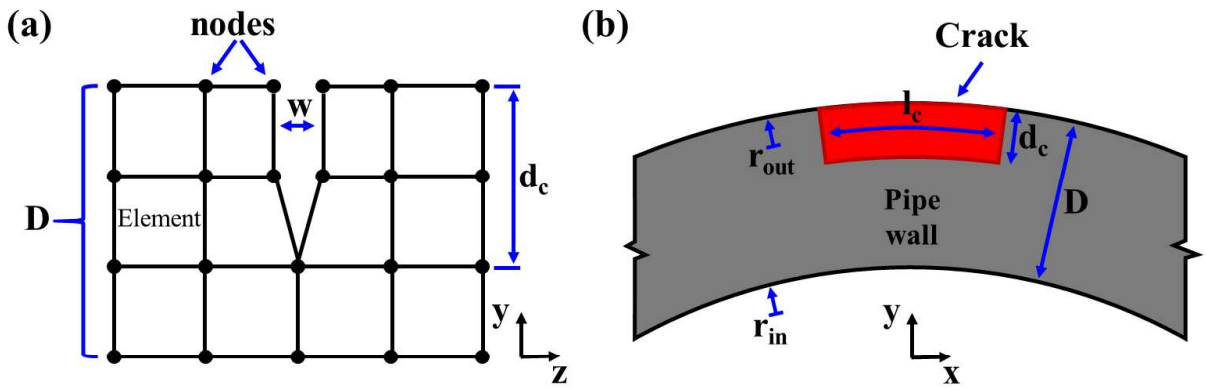

Figure 4.3: (a) Schematic diagram of outer surface breaking planar crack FE modelling by disconnecting adjacent elements in the pipe wall; (b) Cross sectional outline of the crack geometry in the plane perpendicular to the axial z-direction. D is wall thickness, w is crack width, d_c is crack through thickness depth, l_c is crack length, r_{in} and r_{out} are inner and outer pipe radii respectively.

Crack lengths from 2 % to 40 % (0.2 λ_{SH0} to 4.1 λ_{SH0}) of the pipe circumference were simulated (see Table 4.1) to capture the relationship between crack size and accuracy of crack length estimation from the reconstructed images. Smaller increments between the crack sizes were used for the lengths around the resolution limit to allow more accurate estimation, and larger steps in crack sizes were used elsewhere. The study

was repeated for 25 %, 50 %, 75 % and 100 % crack through wall thickness depths.

Table 4.1: Crack lengths used in the FE study.

Crack length as % of the mean circumf.	2	3	4	5	6	7	8	9	10	11	13	15	17	20	25	30	40
Crack length in wavelengths	0.2	0.3	0.4	0.5	0.6	0.7	0.8	0.9	1.0	1.1	1.3	1.6	1.8	2.1	2.6	3.1	4.1

As was discussed in section 3.6, the excitation signal was a 5-cycle Hann windowed tone burst with centre frequency of 50 kHz. The same excitation signal was later used in the experiments.

The FE model included coherent noise due to excitation of the unwanted modes, assuming a perfect transducer. It did not include the coherent noise resulting from the real transducer elements being imperfect nor incoherent noise.

4.4. Experimental setup

The 4 m long, 8 inch nominal diameter, schedule 60 ASTM A106-B steel industrial pipe with 10.8 mm wall thickness used in the experiments (see section 4.3 for pipe details) was chosen based on similarity to the pipe used in [25,58]. This allowed the convenient comparison and cross validation of some of the results.

As was discussed in section 2.5, in the current state-of-the-art pipe GWT systems, only the low resolution synthetic focusing imaging can be achieved. This is because the neighbouring transducers in the ring array are wired together resulting in only six to eight large elements around the pipe circumference. Therefore, for the purpose of this project, a prototype inspection tool allowing individual transducer control had to be developed to facilitate high resolution imaging.

The design of the SH0 guided wave phased array transduction ring was created by the

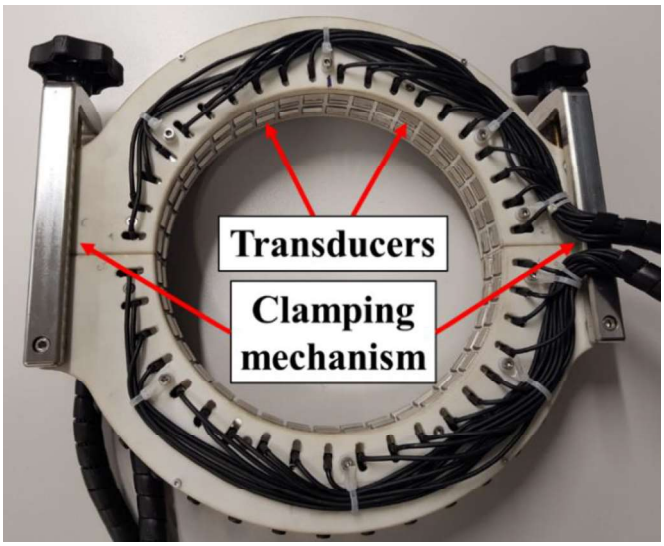

Figure 4.4: Transduction ring used in the experiments.

adaptation of the design of the commercially available Guided Ultrasonics Ltd. solid transduction ring [1]. The ring array, presented in Figure 4.4, consisted of two parts to allow for easy attachment onto the pipe. The main structural chassis of both halves of the ring array were made from a block of Aluminium 6061-T6 milled using a 5-axis CNC machine. The face cover plates were 3D printed from the polyamide (PA12) with 40 % glass fibre reinforcement using selective laser sintering (SLS) technique. The yoke arms used for clamping the ring onto the pipe were milled out of a SAE 304 stainless steel using a 3-axis CNC machine. The developed prototype tool had narrower spacing between the elements compared to the commercial transduction ring, to provide sufficient spatial sampling for the imaging applications. The transduction device consisted of two rows of circumferentially oriented shear contact transducers each containing 40 elements. In the experiment, only a single row was used for transmission and reception as there was no need for directional control. The design allowed for transducer elements to be inserted independently in different orientations. The connection to each individual element was provided via a shielded coaxial cable ending with an MCX connector so that all transducer elements were individually addressable by the electronic instrumentation. The MCX connectors were chosen because they are very compact and they connect/disconnect with a simple push/pull, which is

convenient for large number of elements (i.e. here 80 transducers in total). The author adapted the design provided by Guided Ultrasonics Ltd., and assembled and wired the prototype of the transduction ring.

The experimental setup is presented in Figure 4.5. Two parts of the ring were screwed together on the top and bottom of the pipe to clamp it firmly onto the sample. The ring was placed at the cut end of the pipe so that the active row of transducers is placed right at the edge to suppress any waves travelling in the negative z-direction. An even contact between the transducers and pipe surface was provided by a spring loaded mechanism at each element. The pipe was supported by two wooden blocks to minimise the guided wave reflections from the supports [197]. The connection between the transducer elements and the phased array was provided via a custom made 80×MCX to 2×160 pin Hypertronics adapter.

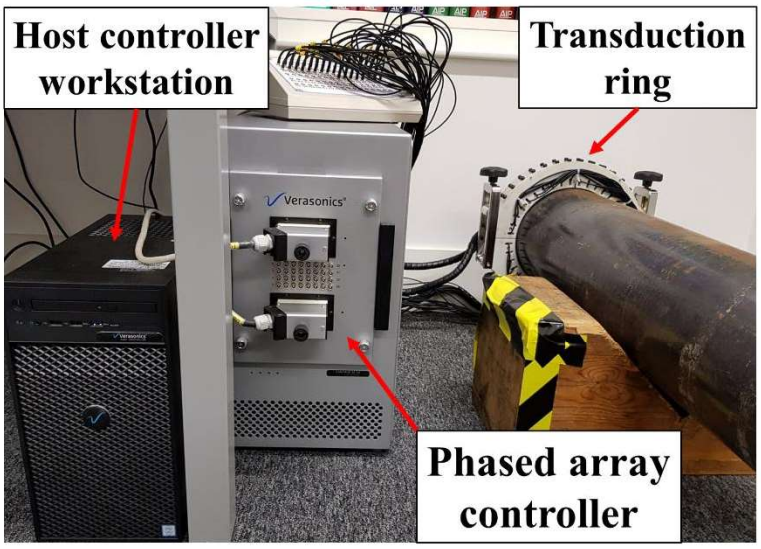

Figure 4.5: Experimental setup.

A Verasonics Vantage™ 32LE phased array controller in a low frequency configuration was used for transmitting and recording the ultrasonic waves via the transduction ring. The sampling frequency on reception was 2.5 MHz. The recorded signals were filtered using a digital bandpass filter with lower limit of 35 kHz and upper limit of 65 kHz. No averaging was used and 42 dB amplification was applied to the recorded signals

through the low-noise built-in amplifiers of the Verasonics phased array controller.

It is often the case that there are variations in the amplitudes of the recorded signals between the transducers in the array. This can be due to, for example, uneven coupling or variation in transducer characteristics. The uneven performance of the array elements can lead to additional coherent noise in the recorded data. Therefore, to compensate for the variations in the transducer performance, a balancing procedure was developed to obtain the balancing coefficients for each array element. First, a fully circumferential 0° SH0 plane wave (essentially T(0,1) pipe guided wave mode) was sent through the undamaged pipe and the cut-end reflection was recorded. The amplitude variations in the recorded echo around the circumference were used to calculate the balancing coefficients B_c for each transducer, as follows:

$$B_c(n) = \frac{\min(A_R)}{A_R(n)}, \tag{4.3}$$

where B_c is a vector of $N = 40$ balancing coefficients for all array elements and A_R is a vector containing peak amplitudes of the cut-end reflection recorded around the pipe circumference.

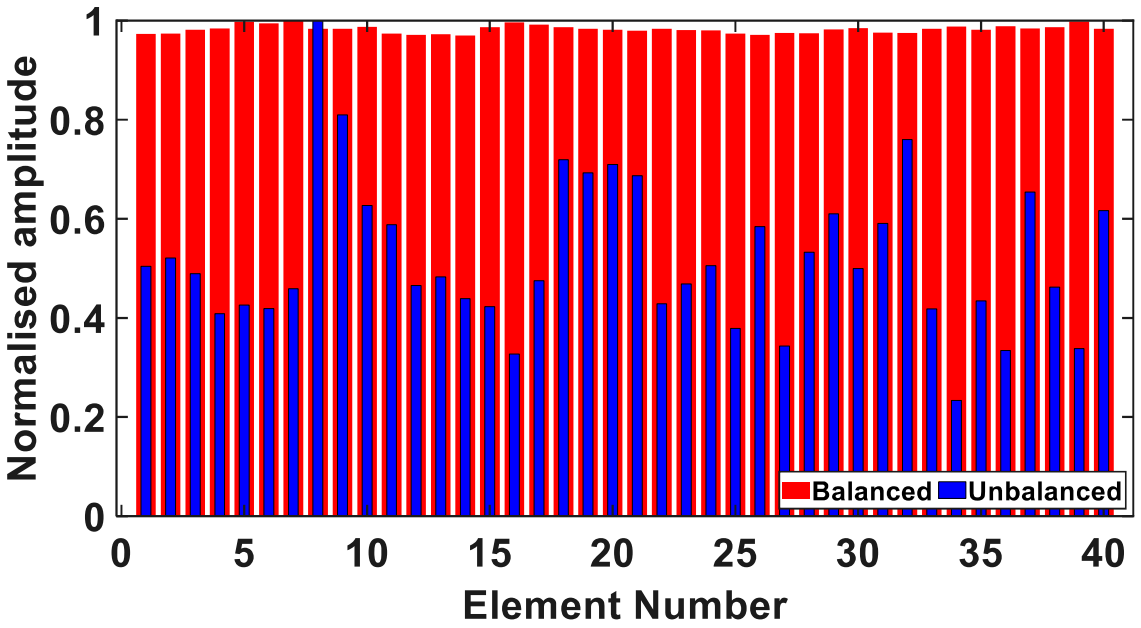

Figure 4.6: Normalised amplitude of T(0,1) guided wave mode cut-end reflection recorded with (red) and without (blue) the use of the transducer balancing coefficients.

Subsequently, the performance of the balancing method was evaluated by exciting again the incident 0° SH0 plane wave and recording the cut-end echo with application of the previously obtained balancing coefficients. A comparison of the normalised T(0,1) echo recorded on each transducer with and without balancing coefficients is presented in Figure 4.6. The amplitude variations between the balanced transducers were within 3 %, which is perfectly acceptable for imaging applications. The experimental results presented in the remainder of this thesis are acquired with the use of balancing coefficients.

The cracks are typically simulated in experiments by the introduction of notches using a CNC milling machine, e.g. [25,185,186,196]. However, the pipe sample was too bulky to use the CNC machines available on site and there was no off-the-shelf portable devices for notch introduction in pipes available in the market. Therefore, a custom made portable solution for circumferential notch introduction was developed in-house by the author. The notching device, presented in Figure 4.7, consisted of a Dremel® 3000 Rotary Tool attached to a mobile aluminium platform via a threaded connection. The platform was fitted with four metal angular contact ball bearings acting as wheels.

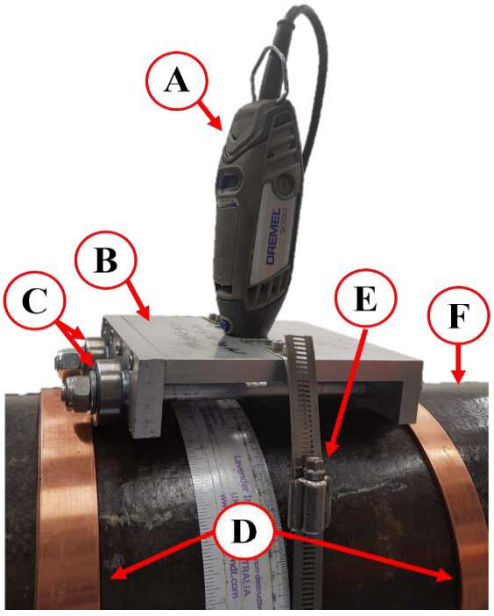

Figure 4.7: The notch milling setup which consisted of: A. Dremel rotary tool; B. aluminium platform; C. angular contact ball bearings; D. guiding rails; E. stainless steel hex screw worm drive band; F. pipe.

They provided a stiff connection between the platform and the pipe surface. The notching device was secured onto the pipe with the stainless steel hex screw worm drive band, as it is shown in Figure 4.7. Such attachment method of the Dremel® to the pipe kept the tool perpendicular to the surface at any circumferential position and provided a fixed distance between the Dremel® chuck and the pipe surface. This was essential for maintaining the constant depth of the introduced notch. The notching tool was guided by the copper rails clamped onto the pipe with the toggle latches. The rail-pipe contact areas were isolated by a layer of felt to prevent transmission of ultrasonic waves to the copper. The propulsion of the rig in the circumferential direction along the rails was provided via the aforementioned stainless steel band which was woven through an additional hex screw worm drive (identical to the one visible in Figure 4.7) glued to the pipe at 180° around the circumference with respect to the notch centre. The worm drive allowed for uniform motion of the notching device around the pipe and accurate position control while milling the notch. The worm drive was relatively small compared to the wavelength and it was only attached at its both ends via epoxy glue to minimise the adhesion area at the pipe surface to reduce its interactions with the ultrasonic waves. The reflections from the drive were not observed in the recorded signals, therefore its influence on the experimental results was concluded to be negligible. Because there was metal to metal contact between the bearings and pipe surface, the notching device was removed from the pipe before each data acquisition to avoid interactions of the ultrasonic waves with the rig.

Circumferential cracks were simulated via introduction of a 3 mm wide and 5.4 mm deep notch (50 % of the wall thickness) at 1.8 m away from the array (see Figure 4.8 for the layout of the experimental setup.). This was done by drilling a 3 mm pilot hole, followed by milling in the circumferential direction using a 3 mm diameter standard milling bit fitted into the Dremel® jig. Figure 4.9 shows a picture of the smallest notch.

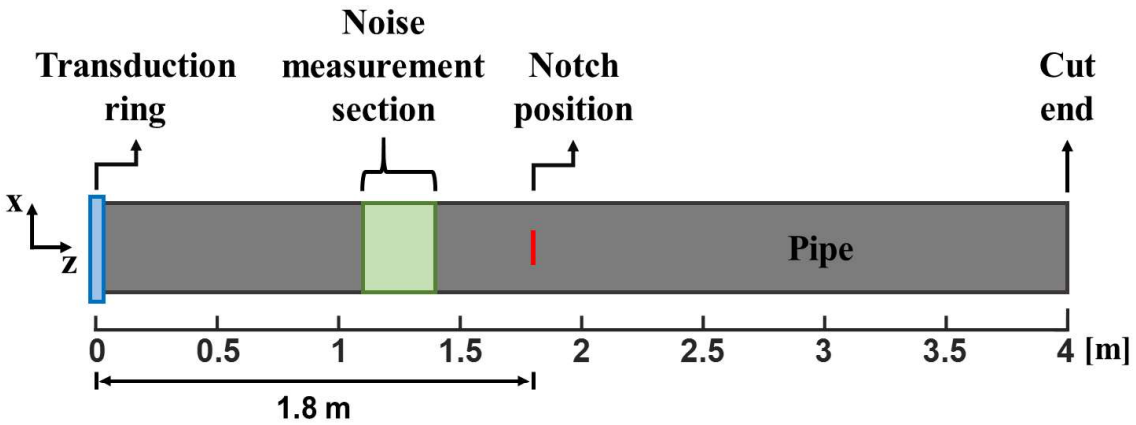

Figure 4.8: The schematic outline of the experimental setup.

To validate the FE study, the circumferential length of the notch was progressively grown in small increments from 2 % to 40 % of the pipe circumference (0.2 λ_{SH0} to 4.1 λ_{SH0}) while the width and depth of the notch were kept constant. This way the FE findings on the relationship between crack length and sizing accuracy (resolution) could be validated experimentally by recreating the FE results for a 50 % through thickness deep crack. To reduce the duration of the experimental study, the number of notch sizes considered was slightly reduced in comparison to the FE study (see Table 4.1). Smaller increments between the notch sizes were used for the lengths around the resolution limit to allow more accurate estimation, and larger steps in notch sizes were

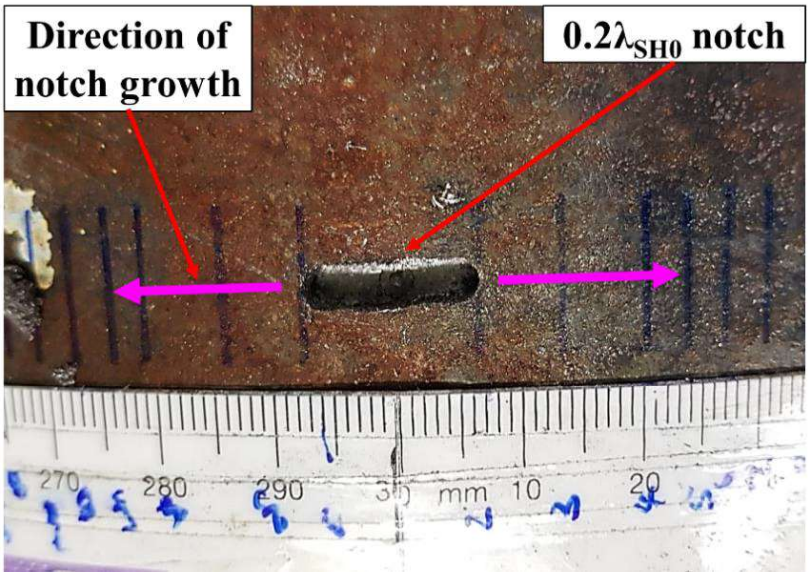

Figure 4.9: The smallest circumferential notch used in the experiments measuring 13.5 mm (0.2 λ_{SH0}) in length, 5.4 mm in through wall thickness depth and 3 mm in width.

used elsewhere. The list of introduced notch lengths is presented in Table 4.2.

Table 4.2: Notch lengths used in the experimental study.

Notch length as % of the mean circumference	2	4	6	7	8	9	10	11	12	14	17	20	25	30	40
Notch length in wavelengths	0.2	0.4	0.6	0.7	0.8	0.9	1.0	1.1	1.2	1.4	1.7	2.0	2.5	3.0	4.1

It was shown in [23] that the axial extent of the circumferentially oriented notch has negligible effect on the reflection from the crack, provided its axial width is much smaller than the probing wavelength (here 3 mm $\ll$ 64.7 mm) and that the length of the crack is larger than its width (here 3 mm $\ll$ 13.1 mm, which is the smallest mean notch length considered). These two conditions were fulfilled in the experiments, hence the introduced notch approximated a narrow crack well.

As discussed in section 2.4.4, the analysis of the guided waves in a pipe can be simplified to the analysis of guided waves in an analogical unwrapped infinite plate, provided the pipe wall thickness is much less than the pipe radius and the wavelength is much less than the pipe circumference. Here the wall thickness of 10.8 mm is much less than the mean pipe radius of 104.6 mm and the wavelength of 64.7 mm is much smaller than the mean pipe circumference of 656.9 mm. Therefore, the plate/pipe approximation can be used for analysis of waves propagating in the experimental sample. The SH0 phase velocity in the sample material was measured to be 3236.2 m/s at 20.5 °C using the time of flight measurement of the waves transmitted from the transduction ring and reflected from the opposite cut-end of the pipe. Using the measured velocity, and the equation (2.39), the maximum phase velocity error due to neglecting the curvature in the plate/pipe approximation was estimated at 0.48 % [25]. This maximum error occurs for 45° and decreases as the angle gets smaller [58]. As will be discussed in the next section, the angular range of waves used for imaging was limited, hence the associated errors were much smaller than the maximum error and

hence they were neglected here.

4.5. Selection of optimal imaging parameters

In this section FE simulations are used to find the optimal imaging parameters for each of the synthetic focusing imaging methods, so that they can achieve the best image quality and can be compared fairly. The imaging methods were optimized for resolution and coherent SNR. The FMCPWI was omitted here because the influence of the imaging parameters on resolution and SNR is identical as in PWI. In PWI the angular step between the transmitted plane waves was set to be 1° which according to [43] is sufficient to achieve maximum resolution.

4.5.1 Transmission

First, it was identified that PWI reconstructions suffer from the same coherent noise bands due to S0 guided wave mode as TFM does (e.g. [58,60]). In PWI these appear due to excitation of a shock wave, portrayed in Figure 4.10. It occurs when the interval between the excitation of the subsequent array elements, needed to achieve the desired angle α_q, closely matches the time it takes for the S0 guided wave mode (excited as a

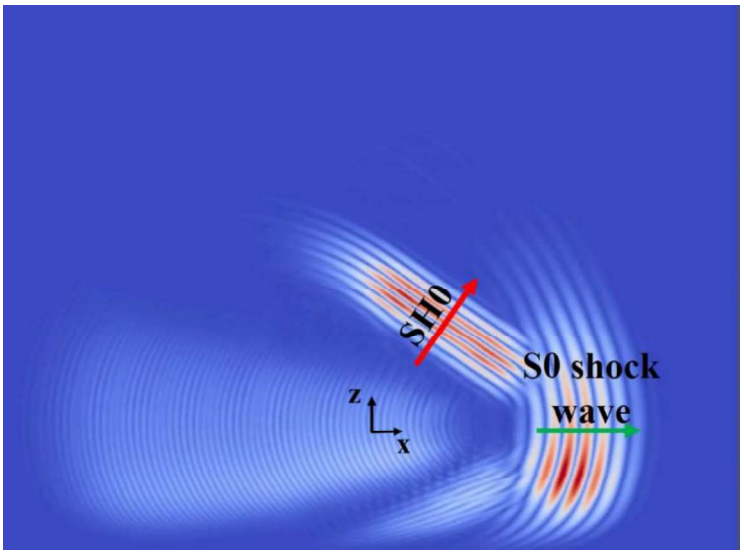

Figure 4.10: Unwrapped pipe schematic presenting the S0 shock wave appearing during transmission of SH0 plane wave at 36.6° angle. x and z are circumferential and axial directions respectively.

by-product [113]) to travel the pitch distance between the array elements. Consequently, the excitation of every subsequent element adds energy to the circumferentially propagating wave front gradually increasing its amplitude.

The critical SH0 angle $\alpha_{crit.}$ at which the shock wave occurs can be found from the following equation:

$$\alpha_{crit.} = \sin^{-1}\left(\frac{c_{SH0}}{c_{S0}}\right). \tag{4.4}$$

In the case study presented in this thesis, this critical angle was 36.6°. At this SH0 plane wave angle, the angle of the faster S0 plane wave is 90°, hence the S0 mode propagates in the circumferential direction. Figure 4.11 (a-b) compares the PWI reconstructions using the transmission angular range of -45° to 45° and -28° to 28°.

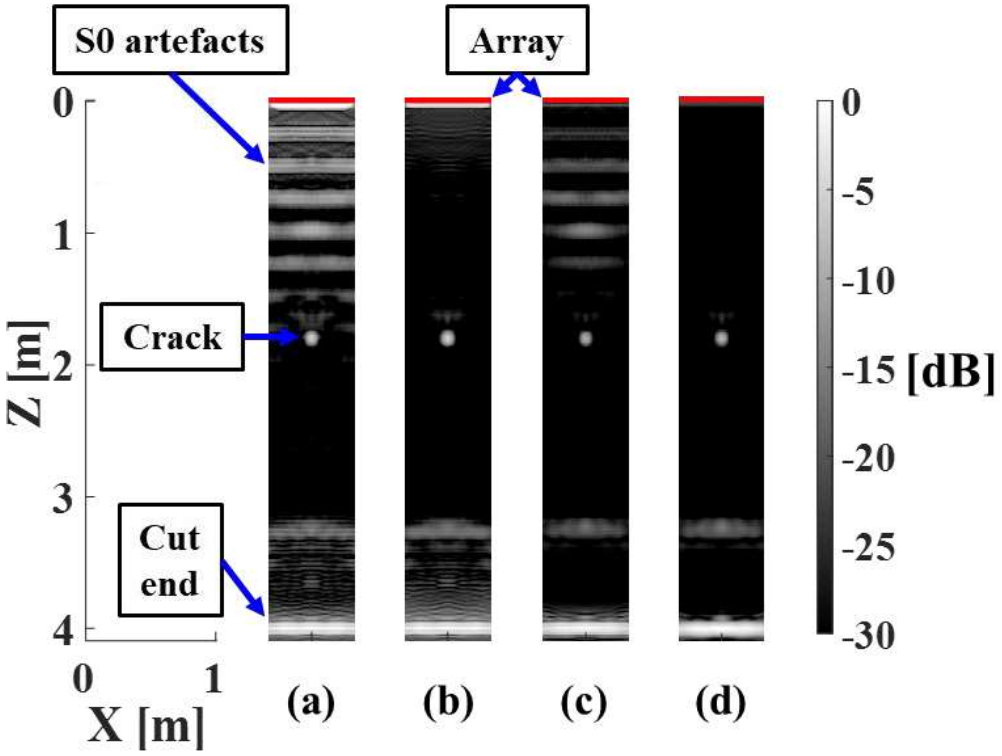

Figure 4.11: Comparison of reconstructions of the FE pipe model with 1.3 λ_{SH0}, 75 % through wall thickness deep crack at 1.8 m axial distance from the array. The unwrapped pipe images were reconstructed using PWI with the transmission angular range of (a) -45° to 45°, (b) -28° to 28°, and TFM using (c) unfiltered FMC data, (d) FMC data with waves travelling at angles larger than 28° removed. x and z are circumferential and axial directions respectively. The image intensity is in decibel scale with respect to the cut-end reflection. 3 helical paths were used for focusing on transmission and reception in TFM reconstructions and 3 helical paths were used for focusing on reception in PWI reconstructions.

The coherent noise bands appear in images reconstructed with the wider transmission angular range, but they are not present when the transmission angular range is decreased to -28° to 28°. Therefore, it can be concluded that decreasing the angular range of transmitted waves below the range at which the S0 mode is excited in the circumferential direction effectively eliminates the coherent noise bands from the PWI images. While the S0 mode propagates at exactly 90° when the SH0 plane wave angle is equal to the critical angle, the artefacts are still noticeable for the transmission angles close to 36.6°. Through the gradual decrease of the PWI transmission angular range it was established that the artefacts vanish at an angular range between -28° to 28°, hence this is the range used for imaging in the project presented here. It is possible to selectively filter out the angles around the critical angle and use the higher transmission angular range as well. However, the SH0 mode incidence angles higher than 40° would result in a substantial conversion of the SH0 mode to the S0 mode on the reflection from the planar surfaces (e.g. crack face, pipe cut-end, welds). This would result in coherent noise which would decrease the quality of the reconstructed images. Additionally, as was shown in [115], the reflectivity of the SH0 waves from cracks is the highest at normal incidence and decreases with the decrease of the angle of incidence. Therefore, the angular range above 40° was deemed unattractive here.

Given the analogy between FMC and PWI acquisition methods discussed in [49], to avoid the coherent noise bands due to the S0 guided wave mode in the TFM reconstructions, angles around the same critical angle should be filtered out, for example, using the method outlined in section 3.8. Figure 4.11 (c-d) shows the comparison of TFM reconstruction using unfiltered data to a reconstruction with waves travelling at angles larger than 28° filtered out from the FMC data. The filtering removes the unwanted coherent noise bands corrupting the reconstructed image, which results in significant improvement in the coherent SNR.

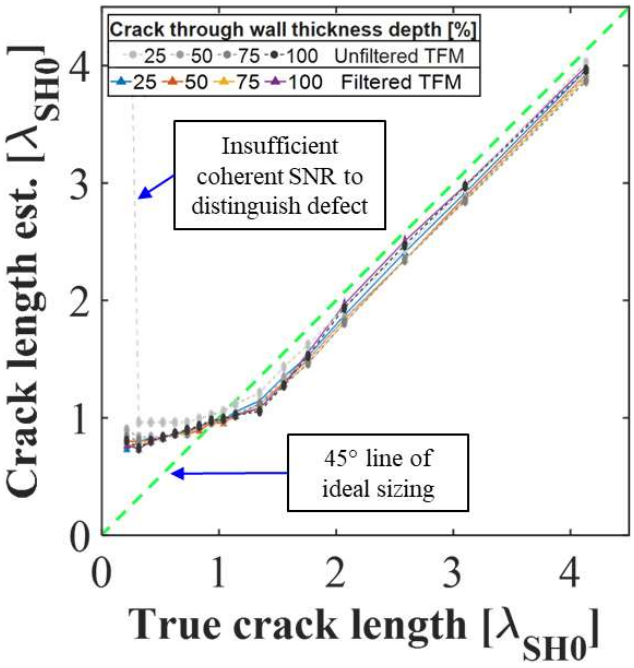

Figure 4.12: Plot of FWHM crack length estimates measured from the images reconstructed using TFM with (solid coloured lines) and without (grey scale dashed lines) FMC data filtering. The crack length estimates are plotted against the true crack lengths. The results are based on the FE simulations. The implemented FMC filtering removed the waves travelling at angles larger than 28° from the ultrasonic data.

Subsequently, the influence of the FMC data filtering on crack lateral length estimation and resolution of TFM was investigated. The circumferential length of each crack was estimated from the reconstructed images using the FWHM method outlined in section 4.2. These estimates were plotted against the true crack lengths for crack through wall thickness depths from 25 % to 100 % in Figure 4.12. As it was discussed in section 3.6, the resolution of imaging algorithms is limited by diffraction. Therefore, in theory, it would be expected that the FWHM estimate curves would follow the 45° line of ideal size estimate for longer cracks and the curves would plateau when crack lengths are below the resolution limit. The sub-resolution crack indications were expected to essentially become a PSF, which is one of the measures of the resolution. Instead, around the expected resolution limit, a distinct regime change can be observed. The curves starts to plateau, however instead of transitioning into a horizontal line, the curves descend at a gentle slope and they finally become horizontal at crack lengths smaller than half a wavelength. While the exact nature of that phenomenon has not

been determined, the author suspects that the transition period before the final plateau is related to the finite bandwidth of the probing wave, i.e. the resolution limit for each spectral component of the tone burst is different. Therefore, in this thesis, the resolution limit of the imaging system is taken as the crack length at which it becomes possible to reliably estimate the true length (i.e. with error <10 %) from the reconstructed image. This is the point at which the curves depart from the 45° line of the ideal size estimate. The crack sizing curves plotted for TFM with and without FMC data filtering coincide and they depart from the 45° line of the ideal size estimate at the same value. Therefore, FMC filtering has negligible impact on the lateral resolution.

It is worth noting that for short, shallow cracks (e.g. 0.2 λ_{SH0} long, 25 % through thickness deep crack) the unfiltered TFM curves show a sudden, large overestimation of the crack lateral size. This is associated with coherent noise obscuring the crack indication and impairing defect detection. In the case study presented here, the defect is relatively far away from the array. However, if the defect would be closer and its position would coincide with the S0 mode noise bands visible in Figure 4.11(c), distinguishing a small defect from these noise bands would be impossible. Therefore, elimination of the coherent noise is important in synthetic focusing imaging to achieve good image quality and acceptable detection of defects throughout the entire ROI. In the remainder of this thesis, the FMC data used for TFM imaging was filtered prior to the reconstruction.

Next, the influence of the range of angles used for focusing on transmission on resolution and SNR was investigated. In PWI the angular range of physically excited waves was varied. Because in TFM the angular range of transmitted waves cannot be conveniently controlled, the same was achieved via adjusting the number of helical paths used for synthetic focusing on transmission. In this section, the number of helical

paths used for synthetic focusing on reception was kept constant at 3 helical paths for all the considered imaging methods. Figure 4.13 compares the sizing capabilities of (a) PWI with transmission angles from 0° (CSM) to -32° to 32°, and (b) TFM with 1 to 4 helical paths used for synthetic focusing on transmission. Only angles up to -32° and 32° were included in PWI to avoid coherent noise issues mentioned in the previous paragraph.

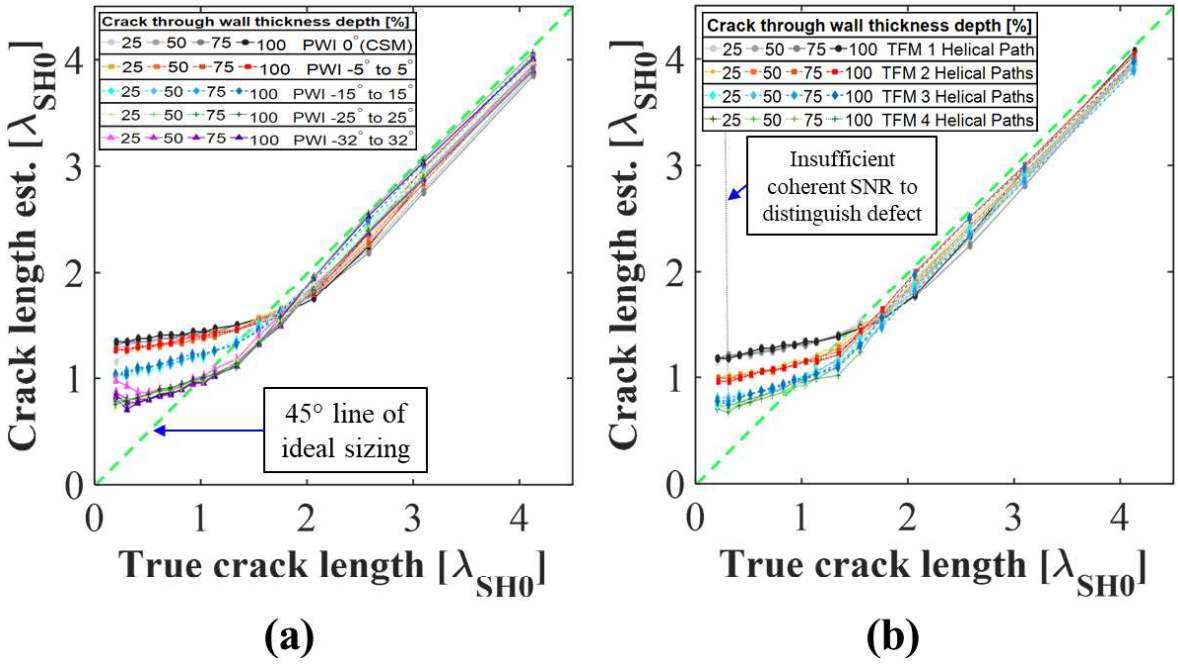

Figure 4.13: Plot of FWHM crack length estimates measured from (a) PWI reconstructions using different plane wave transmission angular ranges, and (b) TFM reconstructions using different range of helical paths for synthetic focusing on transmission. The crack length estimates are plotted against the true crack lengths. The results are based on the FE simulations.

Figure 4.13(a-b) shows the improvement in resolution with the increase in the transmission angular range used for reconstructions in both techniques. In TFM, the noticeable improvement in resolution is between 1 and 3 helical paths. There is marginal improvement using 4 helical paths, however, the coherent SNR is insufficient to distinguish very small cracks from the coherent noise. This limits detectability of small defects, hence 3 helical paths are preferred. In PWI, the angular range between -28° and 28° was found to be the range beyond which there is no further improvement in resolution in the case study presented in this thesis. This is in line with the results

presented in [115], where it was shown that the specular reflection decreases with the incidence angle and there is almost no specular reflection at incidence angles around 30°. It is the specular reflection that reveals the face of the crack and it is a major contribution to the defect indication in the reconstructed image.

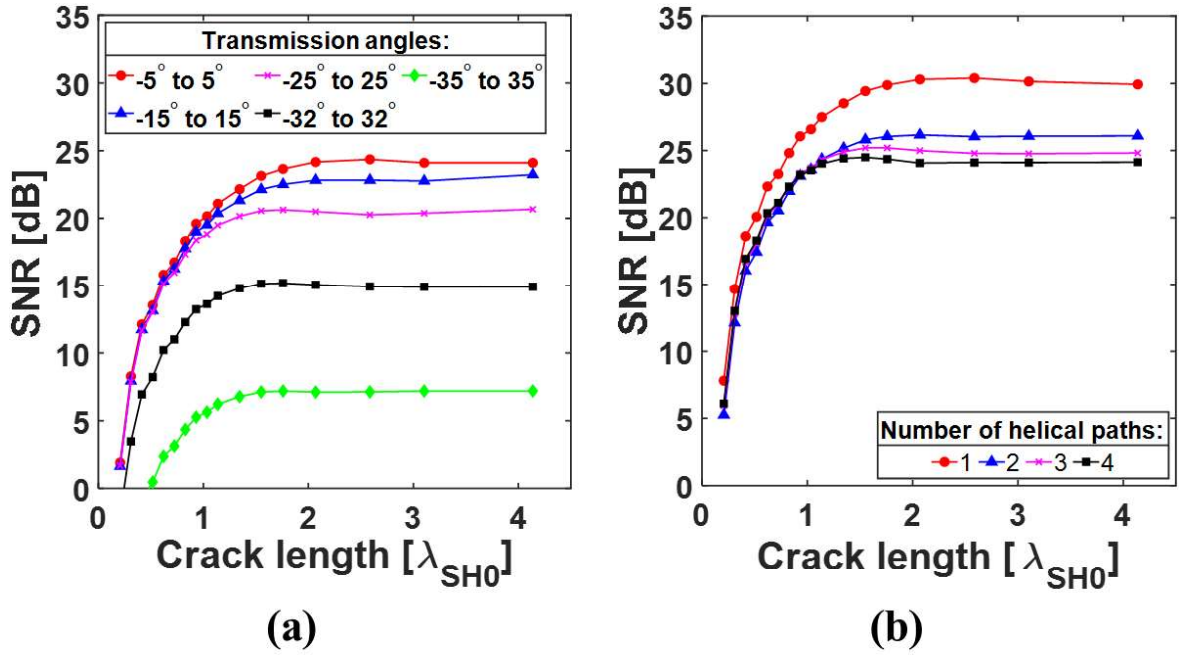

Figure 4.14: Coherent SNR measured from (a) PWI and (b) TFM reconstructions using different angular ranges on transmission. The SNR curves are plotted for the range of crack lengths. The results are based on the FE simulations of 50 % through wall thickness deep crack.

Subsequently, the influence of the transmission angular range on coherent SNR was investigated. The SNR curves for PWI and TFM are plotted in Figure 4.14(a) and (b) respectively. The SNR of each reconstruction was measured using the method outlined in section 4.2. In general, there is a decrease in SNR with an increase in angular range used for focusing. In PWI, there is a considerable drop in coherent SNR when increasing transmission angular range beyond -25° and 25°. This is because the S0 noise band artefacts are increasingly appearing when approaching the critical angle of 36.6°. The observed negative SNR for shorter cracks means that the RMS of the coherent noise is higher than the defect indication amplitude which is not desired. Therefore, to avoid coherent noise issues, transmission angles should be kept well below the critical angle. In TFM, on the other hand, the considerable coherent SNR drop is

not observed when increasing the angular range on transmission and coherent SNR appears to be around 5 dB higher compared to PWI. This is caused by the filtering used on FMC data which removes the coherent noise beyond the desired angular range. Comparable results would be achieved if there was no filtering used in TFM (see Figure 4.11).

4.5.2 Reception

To select the optimal angular range on reception, its influence on image resolution and SNR was investigated. For each FE model, images of the interrogated area were reconstructed using the range of helical path orders from 1 to 4. Estimated crack lengths were plotted against their true values for each imaging method. Crack through wall thickness depths between 25 % and 100 % were considered. In this section, the angular range of transmitted plane waves in PWI was kept constant at -28° to 28° and in TFM 3 helical paths were used for focusing on transmission. The FWHM crack length estimate plots for CSM, PWI and TFM are presented in Figure 4.15.

For all three considered methods, with the increase in the number of helical paths from 1 to 3, the FWHM curves depart from the 45° line of ideal size estimate at significantly lower crack lengths for each additional helical path of higher order used for reconstruction of the image. Therefore, a wider angular range on reception results in better resolution. There is no change when increasing the number of helical paths from 3 to 4, or further. The relationship between the angular range used for reconstructions and sizing accuracy obeys the law of diminishing returns i.e. when the angular range is small, increase in that range results in significant improvement in resolution, but as the angular range gets wider, its further broadening yields less impact on the achieved resolution. Eventually the angular range reaches the point at which its further increase does not improve resolution, which is the maximum achievable resolution.

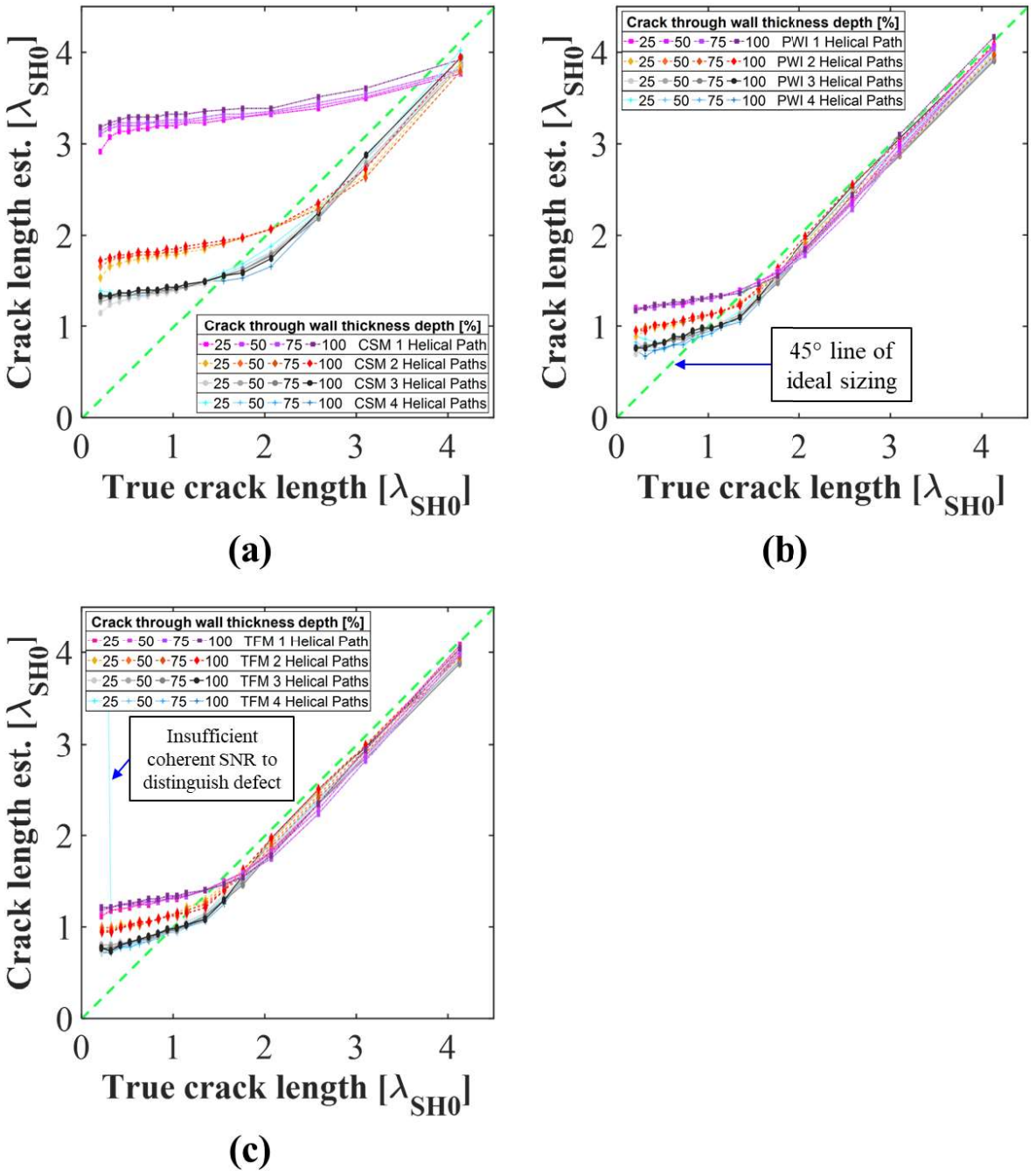

Figure 4.15: Crack length estimates obtained from (a) CSM, (b) PWI and (c) TFM images reconstructed from the FE data, plotted against true crack lengths for different range of helical paths used for focusing on reception.

Figure 4.16 presents the coherent SNR values measured from the reconstructed images of 50 % through wall thickness deep cracks using (a) CSM, (b) PWI and (c) TFM. For each imaging method, the curves represent a different range of helical paths used for focusing on reception. For all three considered imaging methods the same pattern can be observed, i.e. SNR noticeably degrades with the increase in number of helical

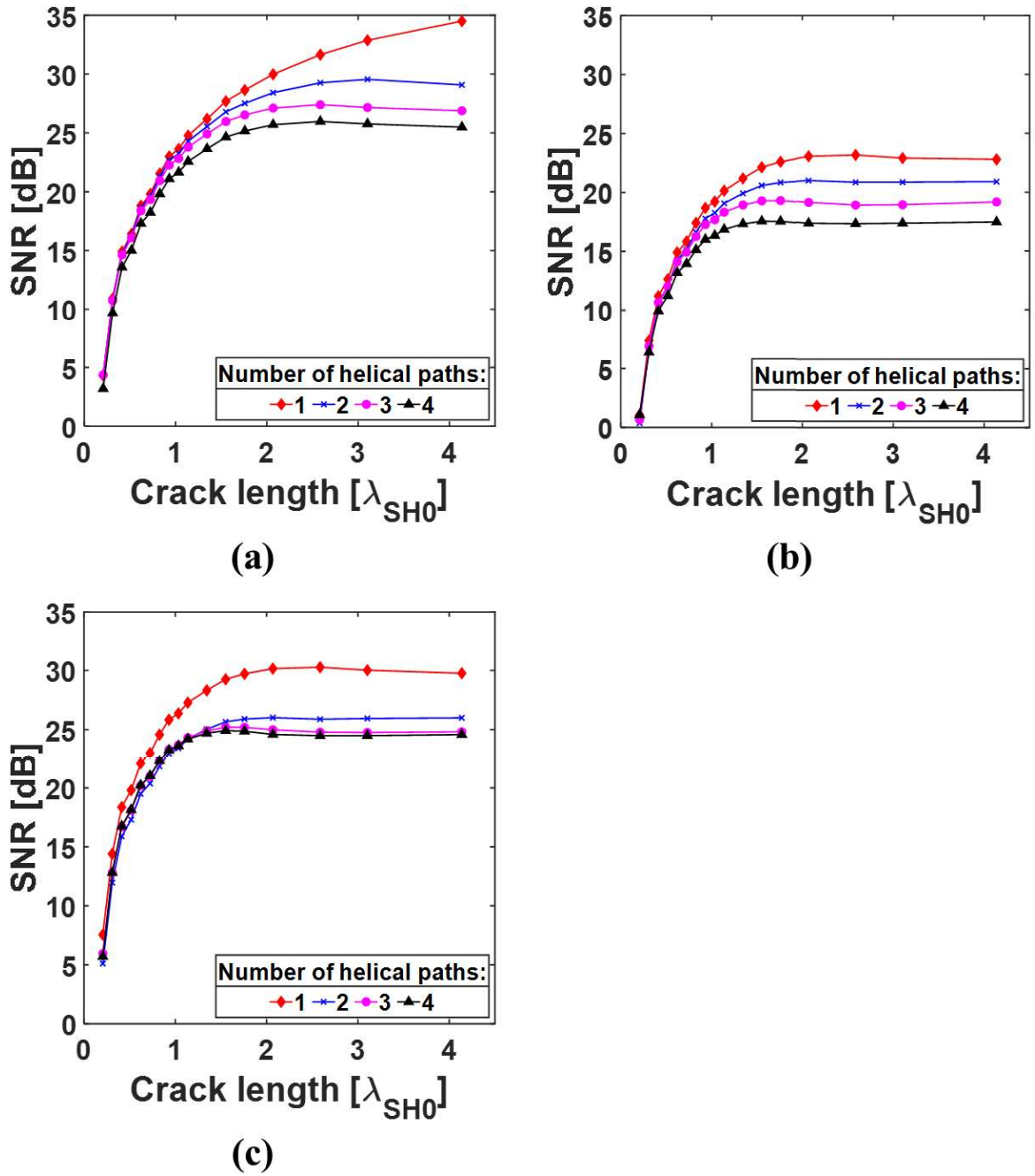

Figure 4.16: Coherent SNR measured from (a) CSM, (b) PWI and (c) TFM reconstructions plotted against the true crack lengths. The results are based on the FE simulations of 50 % through wall thickness deep crack.

paths used for reconstruction. As could be expected, CSM has higher coherent SNR in comparison to PWI and TFM, thanks to 0° SH0 plane wave excitation which effectively suppresses the unwanted modes. The coherent noise in PWI and TFM is primarily caused by inevitable excitation of the S0 guided wave mode when exciting SH0 guided waves.

4.5.3 Discussion on selection of imaging parameters

From the above results, it can be concluded that achieving optimal image reconstruction resolution and coherent SNR depends (amongst other factors) on appropriate selection of angular ranges on transmission and reception. The angular range used for reconstruction has to be sufficient to allow the best resolution, however extending it beyond this range decreases coherent SNR and hence degrades the quality of the image.

In the case study presented in this thesis, the optimal number of helical paths on reception to achieve the best defect reconstruction at 1.8 m away from the array was found to be 3 for all the considered imaging methods. For PWI and FMCPWI, the optimal transmission range was found to be between -28° to 28° and for TFM the optimal number of helical paths used for focusing on transmission was 3.

It is worth noting that to achieve the same optimal resolution throughout the whole length of the pipe in the time domain implementation of synthetic focusing imaging methods, the number of helical paths used for reconstruction varies with axial position. In general, in classic bulk wave imaging, resolution decreases with the axial distance from the array as the effective transmission/reception angular range decreases away from the array. In the case of pipe GWT, when using a set number of helical paths throughout the length of the pipe the same phenomenon occurs. This can be mitigated by progressively increasing the number of helical paths used for reconstruction of pixels with increase of axial distance to maintain quasi constant angular range on transmission/reception. In other words, pixels further away would have to be reconstructed using more helical paths than pixels closer to the array. In practice, for short range pipe applications, a fixed number of helical paths is typically sufficient. In

PWI, transmission angles remain constant throughout the length of the pipe, hence they would not need to be changed.

4.6. Lateral crack sizing

This section compares and evaluates the lateral crack sizing capabilities of CSM, TFM, PWI and FMCPWI. For the fair comparison of all four image reconstruction methods, they were implemented here using the optimal imaging parameters found in the previous section. The comparison is based on the FE and the experimental results. The study evaluates the example case with a range of part-circumferential part-depth cracks/notches.

Figure 4.17 shows the comparison of the FWHM crack length estimate curves obtained from CSM, TFM and PWI reconstructions using the FE data. Four through wall thickness crack depths were considered here, 25 %, 50 %, 75 % and 100 %.

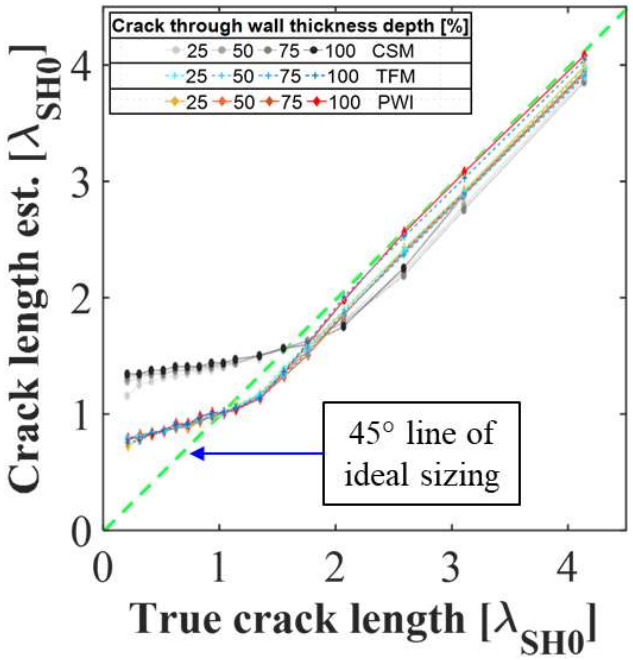

Figure 4.17: Plot of FWHM crack length estimates measured from CSM, TFM and PWI reconstructions based on FE data. The crack length estimates for a range of crack through thickness depths are plotted against the true crack lengths.

The SH0 CSM curves depart from the 45° line of ideal size estimate at larger crack lengths compared to TFM and PWI, indicating inferior resolution of CSM. From the plot, the maximum achievable resolution by CSM is around 1.4 λ_{SH0} which is consistent with results presented in [25,58], where the angular spectrum method implementation of pipe guided wave CSM was investigated. These comparable results mean that the time domain implementation of synthetic focusing imaging algorithm yields the same resolution as the angular spectrum method. They also serve as cross validation for the FE results presented here.

PWI and TFM crack length estimate curves look almost identical, and they depart from the 45° line of ideal size estimate at the same value. This means that their maximum achievable resolution is comparable, and it is around 0.9 λ_{SH0} which is close to the theoretical 0.5 wavelength diffraction limit. This is a significant improvement in comparison to the maximum achievable resolution by CSM, therefore, both TFM and PWI are better suited for characterisation of small defects in pipes.

Figure 4.18 shows the comparison of the parts of the k-space recovered through the reconstruction using (a) TFM, (b) PWI and (c) CSM methods, assuming a monochromatic probing wave. The spatial frequency mapping procedure used here was outlined in section 3.6. Because in CSM the ROI is illuminated from a single angle, the spatial frequencies encoded by CSM lie on the arc corresponding to a range of angles used for imaging on reception. The spatial frequencies retrieved through PWI and TFM essentially comprise a superposition of a number of such arcs at the range of different angles corresponding to the angles of transmitted probing waves. The comparable resolution of PWI and TFM observed earlier is related to the fact that the range of spatial frequencies which both methods retrieve through the imaging process is practically identical, as it can be seen in the Figure 4.18(a-b). The part of k-space

retrieved with CSM is substantially smaller due to the single illumination angle, which is in line with the inferior resolution noticed in the FE results presented earlier.

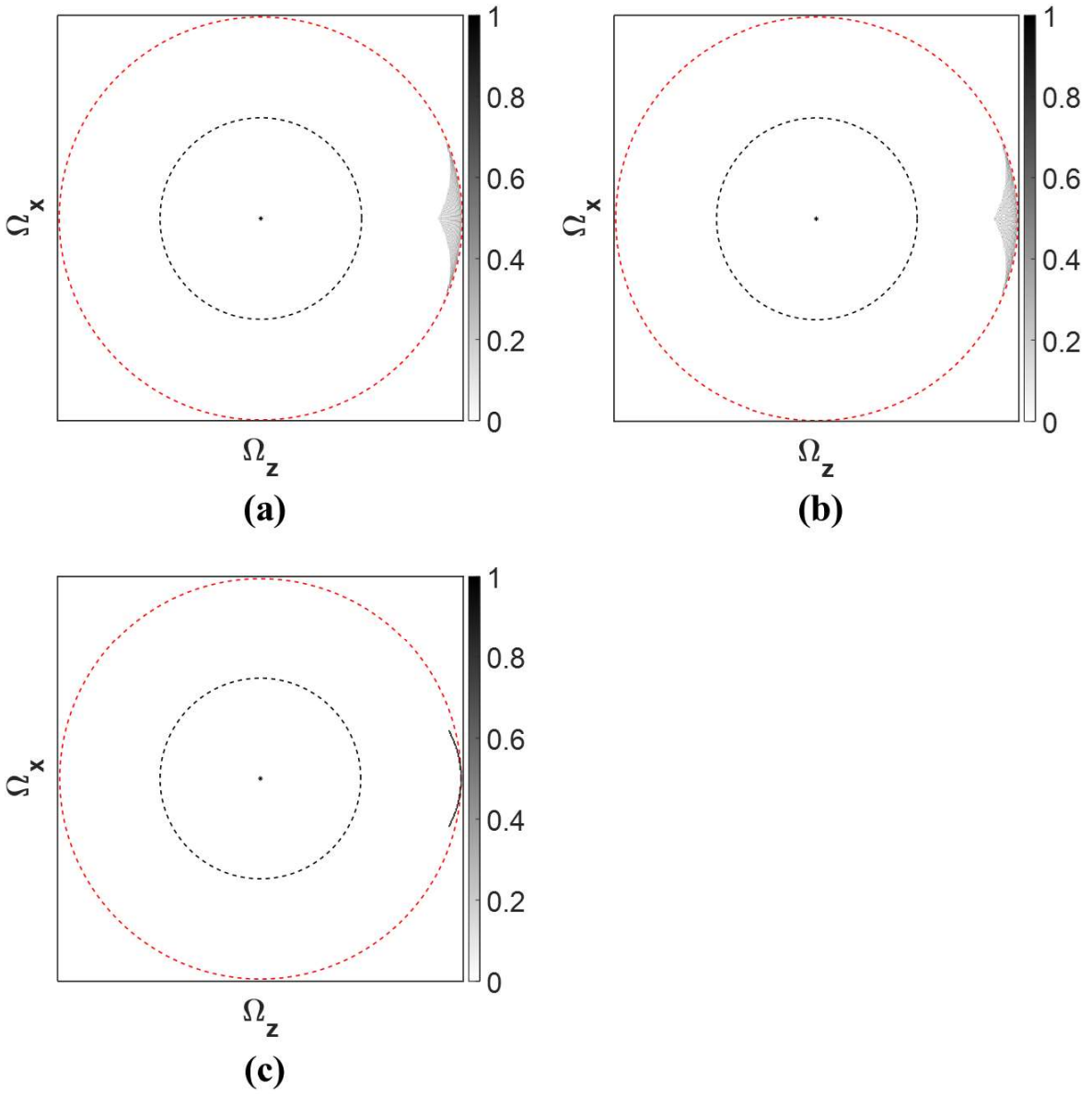

Figure 4.18: K-space plots comparing spatial frequencies retrieved with (a) TFM, (b) PWI and (c) CSM. The k-space plots are for an arbitrary point 1.8 m away from the array aligned with the centre of the array. Transmission plane wave angles in PWI were between -28° and 28°, 3 helical paths on reception were used for all methods and 3 helical paths on transmission were used in TFM. The plots present the normalised sum of contributions from all transmission/reception direction pairs.

Since PWI and TFM achieve comparable resolution and recover the same spatial frequency range, the main difference between the two imaging algorithms is the method of ultrasonic data acquisition. The comparison between the two acquisition methods, PWI and FMC, can be conveniently done by comparing the performance of PWI and

FMCPWI. Both methods use the same reconstruction algorithm, and the only difference is that the latter one synthesizes plane wave ultrasonic data from the FMC data. As presented in Figure 4.19, in FE simulations, PWI and FMCPWI yield identical results. This is rather expected since the superposition of the contributions from each array element and application of appropriate delay laws can be performed in the FE model or the same result can be achieved by superposition in post processing. This is due to the fact that the ultrasonic wave propagation in the considered geometry is a linear problem, hence the superposition principle is valid here. Therefore, it can be concluded that the method of acquisition, FMC or transmission of actual plane waves, has no impact on resolution nor coherent SNR. Therefore, their performance in the real world applications is predominantly determined by the incoherent SNR, which will be investigated in the next section.

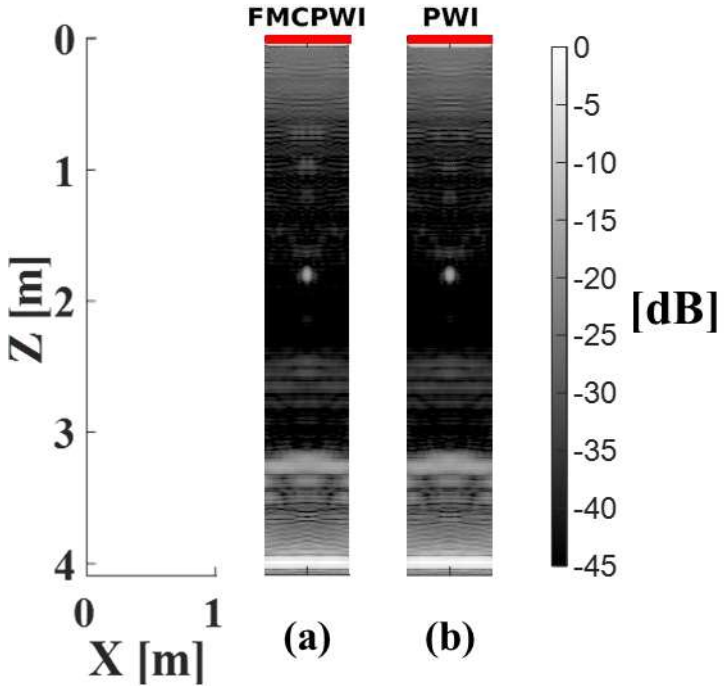

Figure 4.19: Comparison of (a) FMCPWI and (b) PWI reconstructions presented in the form of unwrapped pipe. The ultrasonic data was obtained from the FE simulations. x and z are circumferential and axial directions respectively.

So far the discussion was based on FE data. Here, the FE results are validated by the comparison of the FE and the experimental FWHM crack/notch length estimate

curves obtained from the CSM and PWI reconstructions for 50 % through wall thickness deep crack/notch, as presented in Figure 4.20(a). The curves obtained from the experiments closely resemble the ones from the FE study, which supports validity of the FE results. The experimental results confirm that PWI clearly outperforms CSM in terms of achievable resolution.

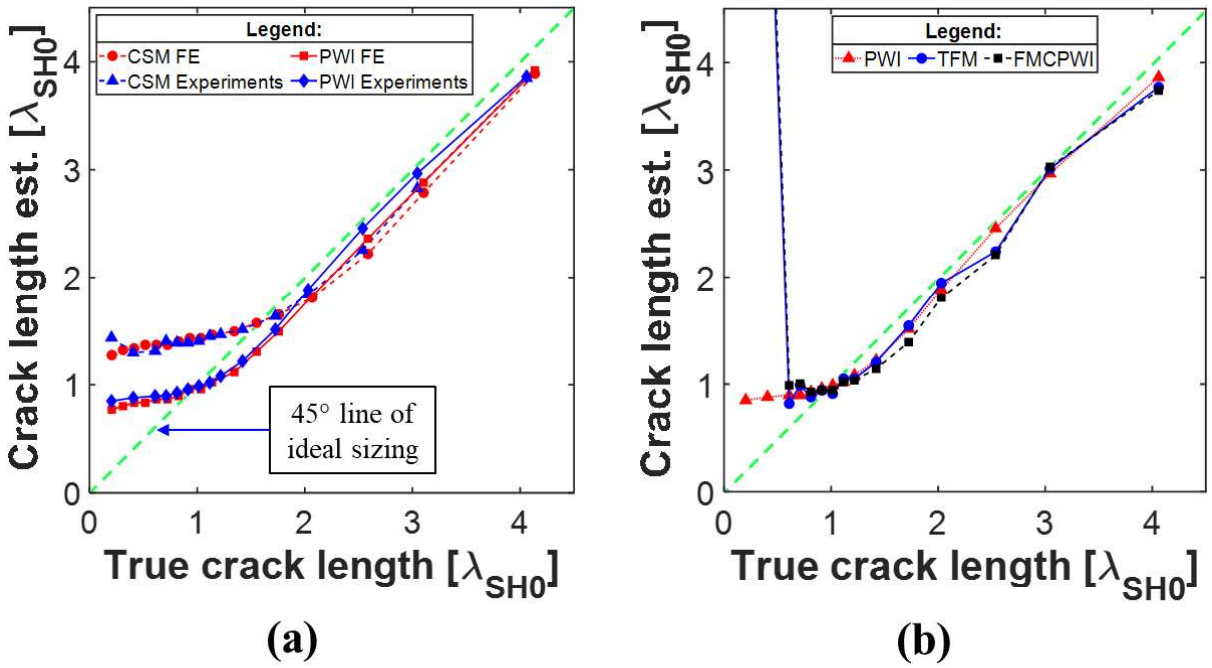

Figure 4.20: Comparison of FWHM sizing capabilities of (a) PWI and CSM using experimental and FE results for 50 % through thickness deep notch/crack, (b) PWI, TFM and FCPWI using experimental results for 50 % through thickness deep notch.

Subsequently, the FWHM notch length estimate curves for PWI, TFM and FMCPWI obtained from the experiments are compared in Figure 4.20(b). As expected, all three methods perform alike for almost all notch lengths, except for short notches. In the case of notches shorter than 0.6 λ_{SH0} TFM and FMCPWI curves reveal great notch size overestimate, while PWI behaviour resembles the behaviour observed in the FE study. The severe notch length overestimate is a sign that the sizing algorithm does not distinguish notch indication from the noise related artefacts. This happens when the noise level is less than -6 dB below the defect indication amplitude. This makes sizing small defects using FMC based approaches unreliable. The experimental PWI curve departs from the 45° line of ideal size estimate at 0.9 λ_{SH0}, which marks the resolution

limit of this method. The error in defect sizing is given by deviation of the FWHM size estimate points from the 45° line of ideal sizing. For each method, within its resolution limits, the error is less than 10 - 15 %, and typically much less than that, as can be seen in Figure 4.20(b). It rapidly increases when the notch size is below the resolution limit. The sizing accuracy can be further improved by using the FWHM plots (e.g. Figure 4.20) as sizing correction charts similarly to the method proposed in [198]. The exact defect lateral size can be found by mapping the defect indication length measured from the PWI reconstruction onto the FWHM curve and looking up the corresponding true defect length. The FWHM curves for a particular inspection scenario could be obtained through the FE simulations or experimentally using a sample of a similar material and geometry to the inspected pipe.

4.7. SNR comparison

According to the FE results presented earlier in Figure 4.17 and Figure 4.19, TFM, PWI and FMCPWI should produce comparable results with resolution on the same level and coherent SNR sufficient to reliably size small defects. Therefore, poor SNR in experiments observed in the previous section is attributed to incoherent noise which is only present in experiments. In FE, PWI and FMCPWI results are indistinguishable, while in experiments PWI clearly suffers less from incoherent noise issues compared to FMCPWI. Since the only difference between these two techniques is the acquisition method, it can be concluded that the increased noise level is associated with the acquisition method. FMCPWI uses the same FMC data as the TFM algorithm and only these two methods experience SNR issues. Furthermore, the FMC data is filtered in the Fourier domain prior to TFM and FMCPWI reconstructions, hence if the noise was coherent, significant SNR improvement should be observed, however this is not the case.

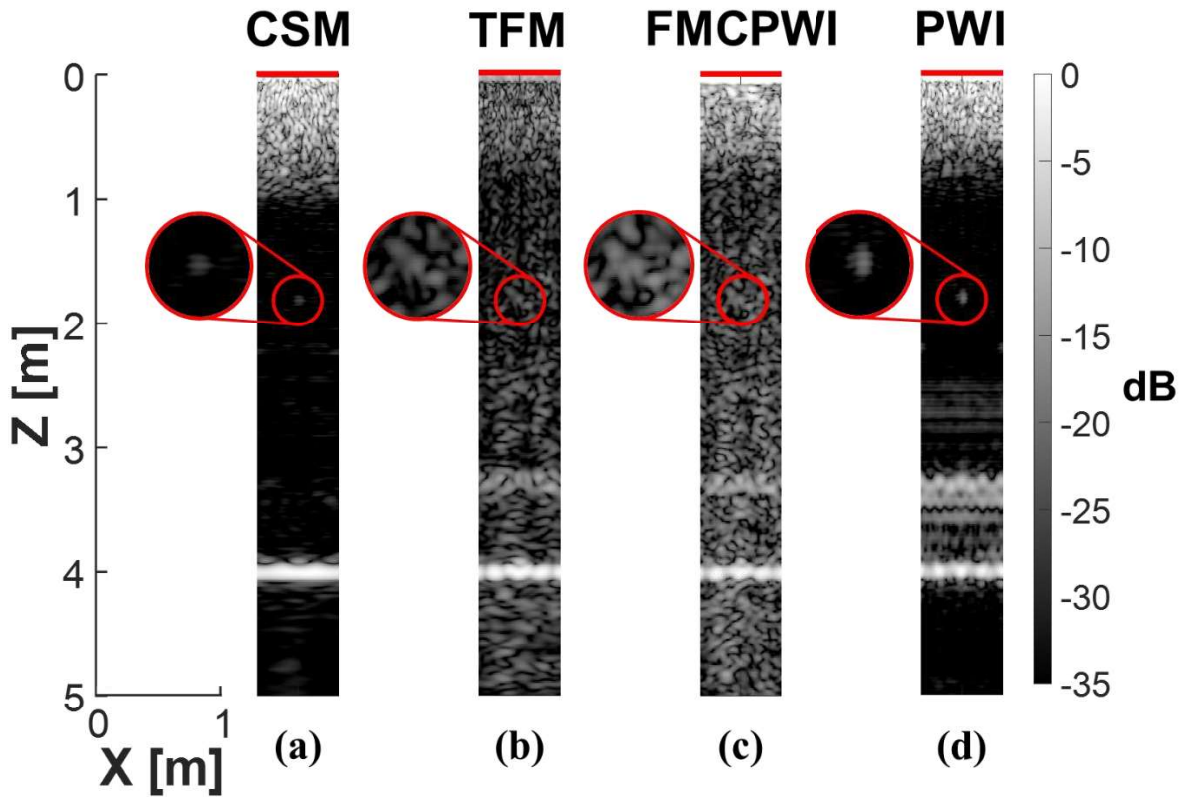

Figure 4.21: Comparison of reconstructions of 0.2 λ_{SH0} long, 50 % through wall thickness deep notch at 1.8 m axial distance from the array using (a) CSM, (b) filtered TFM, (c) filtered FMCPWI and (d) PWI. The images are reconstructed from the experimental data and they are presented in the form of unwrapped pipe. The notch removed 1 % of the CSA of the pipe.

Figure 4.21 shows the reconstructions of a pipe with a 0.2 λ_{SH0} long, 50 % through wall thickness deep notch at 1.8 m axial distance from the array obtained using all four studied synthetic focusing imaging methods. The empirical inspection of these images further supports the above hypothesis; one can notice in the TFM and FMCPWI reconstructions artefacts typical for incoherent noise. Moreover, for this short notch, TFM and FMCPWI have insufficient SNR to distinguish defect indication from the noise artefacts which hinders defect detection sensitivity of these methods.

Figure 4.22 shows the comparison of experimental SNR for all four considered techniques. It can be noted that, in general, FMC based methods have lower SNR in comparison to CSM and PWI. Counterintuitively, PWI achieves higher SNR compared to CSM. The latter technique uses only a single plane wave for reconstruction, whereas PWI uses multiple acquisitions. Using multiple acquisitions for each reconstruction is

in some respect equivalent to averaging and results in improved incoherent SNR of PWI in comparison to CSM. On the other hand, TFM uses multiple acquisitions, but this is not enough to compensate for very low transmission energy. Energy transmitted per each acquisition in the FMC approach is only a fraction of energy transmitted during each PWI acquisition. As a consequence, TFM's SNR is lower than the SNR of PWI or even CSM. FMCPWI and TFM using Fourier filtered FMC data achieve identical SNR. FMCPWI using unfiltered FMC data achieves on average around 5 dB lower SNR, compared to the filtered FMC implementations. However, even with Fourier filtering, SNR of FMCPWI and TFM reconstructions are on average around 10 dB lower compared to the reconstructions obtained from classic unfiltered PWI. This difference is associated with a difference in incoherent SNR between FMC and PWI methods of acquisition.

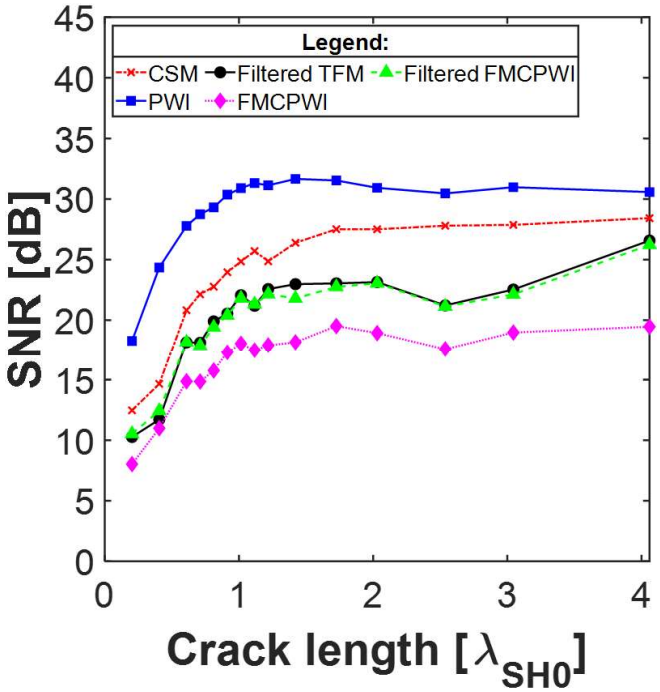

Figure 4.22: SNR vs true crack length for 50 % through wall thickness deep notch measured from (a) CSM, (b) PWI, (c) filtered TFM, (d) unfiltered FMCPWI and (e) filtered FMCPWI reconstructions obtained from experimental data.

In TFM, FMCPWI and PWI reconstructions in Figure 4.21 the false cut-end echoes are visible between 3.2 m and 3.3 m away from the array. These are due to the SH0

to S0 and S0 to SH0 mode conversions at the cut-end. In PWI reconstructions in experiments the maximum false echo indication was measured at -11.5 dB with respect to SH0 cut-end echo. In TFM reconstructions the maximum false echo indication was at -11.1 dB, however there is substantial incoherent noise overlaid, hence this number is not reliable. According to the FE simulations, the false echoes in TFM and PWI are similar (e.g. see Figure 4.11), and these were measured to be -17.5 dB and -16 dB respectively. The false echoes in PWI reconstructions will be discussed further in section 4.9 together with a proposal of a method for their mitigation.

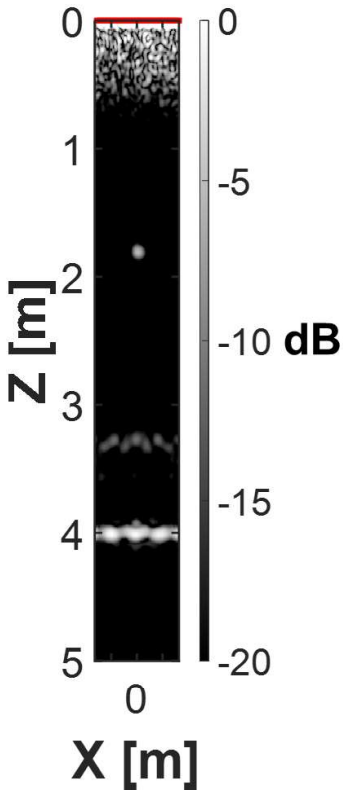

Figure 4.23: PWI reconstruction of pipe with 1.4 λ_{SH0} long 50 % through wall thickness deep notch. The image is reconstructed from the experimental data and it is presented in the form of unwrapped pipe. The notch removed 7 % of the CSA of the pipe.

In the reconstructions presented in Figure 4.21, the noise is very visible in the images, because the wide dynamic range was set to allow observation of a very small notch of 1 % of the pipe CSA, to prove the capability of detection of such small defects using PWI and CSM, and to aid discussion on the origins of the noise. For balance, Figure 4.23 presents the PWI reconstruction of a pipe with larger, 1.4 λ_{SH0} long 50 % through

wall thickness deep notch which removes 7 % of the pipe CSA.

From the above discussion and results it can be concluded that the performance of the techniques based on FMC is primarily limited by incoherent SNR. In experiments, PWI noticeably outperforms these techniques in terms of sensitivity to small defects. Despite the resolution of FMCPWI and TFM being comparable to PWI, these techniques should not be deployed for detection and sizing of small defects without any methods mitigating incoherent noise such as averaging or coded excitation [199-201]. While these mitigating methods provide improvement in SNR, they have some drawbacks which should be considered while choosing a technique for short range GWT inspection. The advantage of PWI is that it does not require application of these mitigating techniques, providing good SNR thanks to the high energy transmission per each acquisition. Research presented in [43,49] also suggests that PWI can achieve comparable resolution to TFM with fewer acquisitions. In fact, unlike the FMC based approaches, in PWI the number of acquisitions does not depend on the number of elements in the array. Hence, this method is particularly attractive for arrays with large numbers of elements. Additionally, each PWI inspection automatically acquires data that can be used for classic T(0,1) guided wave inspection and to produce CSM reconstruction, which is advantageous and allows simultaneous use of both techniques without additional transmissions and processing. CSM can aid reliable detection of defects in the small section of pipe where false echoes appear in PWI.

Because PWI and TFM perform alike in terms of resolution, and PWI was shown to achieve a superior SNR, only PWI is considered in the remainder of this chapter.

4.8. Crack depth estimation

It was shown in [25,58] that it is possible to estimate crack through wall thickness depth from maximum defect indication amplitude (intensity) measured from the images reconstructed using CSM. The same idea can be used with PWI. Figure 4.24 shows a plot of the maximum crack indication amplitudes measured from the PWI reconstructions against the crack/notch circumferential extent in wavelengths of the probing wave for all the considered crack/notch depths. The solid curves are obtained from the FE simulations and the dashed curve corresponds to experimental results. The amplitudes are normalised by the cut end indication amplitude measured in the pipe without a defect.

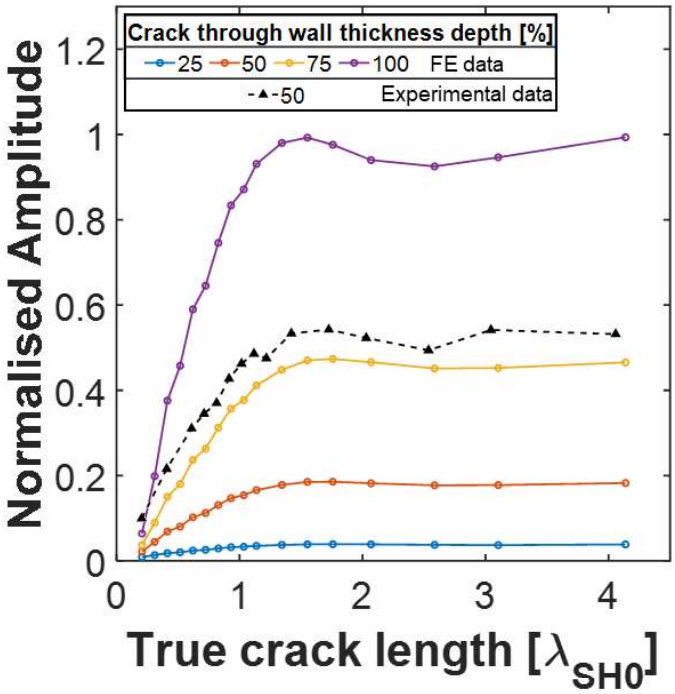

Figure 4.24: Maximum crack indication amplitude normalised by cut end indication amplitude versus true crack length for a range of crack/notch through wall thickness depths from 25 % to 100 %. Solid curves represent FE data and dashed curve corresponds to experimental results. The curves were obtained from the PWI reconstructions.

Looking at the FE curves, they are very similar to the ones presented in [25,58] for CSM. For shorter cracks the amplitude increases with an increase in the length of a crack and it reaches the amplitude peak around 1.5 λ_{SH0}. At this point the curves

plateau at different amplitudes for each respective crack depth and with further increase in crack length, these amplitudes remain relatively constant. The slight amplitude peak observed around 1.5 λ_{SH0} is associated with interaction of crack tip diffraction with the crack face reflection. A detailed investigation into this phenomenon in plates can be found in [113]. It can be concluded from Figure 4.24 that, in general, the amplitudes at which crack indications plateau are proportional to crack through thickness depths. The deeper the crack is, the higher its indication amplitude. The amplitude of through wall thickness crack is almost the same as the amplitude of cut end reflection with its peak amplitude at 99 % of cut end amplitude. This was expected as the through wall thickness crack reflects all incident waves at its circumferential extent.

The shape of the 50 % through wall thickness notch indication amplitude curve obtained from the experiments in Figure 4.24 is remarkably similar to the curves obtained from the FE study. However, the recorded experimental amplitudes are more than double the amplitudes of the corresponding 50 % through wall thickness zero volume crack obtained from the FE simulations. The differences in amplitudes relative to cut end reflection are attributed to the axial extent of the notch and resulting reflections from its front and back faces. Similar difference in T(0,1) reflection between the zero volume cracks and notches with axial extent of 5 % of the probing wavelength (here 3 mm wide notch is 4.6 % of λ_{SH0}) were reported in [22,107]. While the study was conducted for SH0 mode at normal incidence, it appears to be valid for a wider range of incidence angles which are used in PWI. Similar discrepancy between the zero volume crack indication amplitudes in FE and the 3 mm notch in the experiments was observed in [25,58] for CSM. Nevertheless, the FE results presented here were not fully validated and hence more work is needed on this subject in the future.

Because for each through wall thickness depth and length of the crack the indication

amplitudes take different distinct values, it would be possible to estimate the depth of a zero volume circumferentially oriented crack from the reconstructed image using curves obtained from the FE simulations (e.g. Figure 4.24). The approach is yet to be validated experimentally for zero volume cracks, however, given a good agreement between the experiments and FE predictions in the literature for guided wave reflectivity problems [22,23,114,115], it is likely to work. Assuming the crack length can be estimated with good accuracy, the depth estimation is limited to cracks longer than resolution. This is because the depth estimation using similar curves to the ones presented in Figure 4.24 requires the amplitude of the crack indication and its length to be estimated with good accuracy.

4.9. S0 cancelling transduction setup

The new transduction setup cancelling the unwanted S0 mode which was proposed in section 3.9 was implemented in the FE simulations. Figure 4.25(a-b) shows the comparison of a transmitted 10° SH0 plane wave with and without the S0 cancelling. It is apparent that the S0 cancelling transduction suppresses the unwanted S0 plane

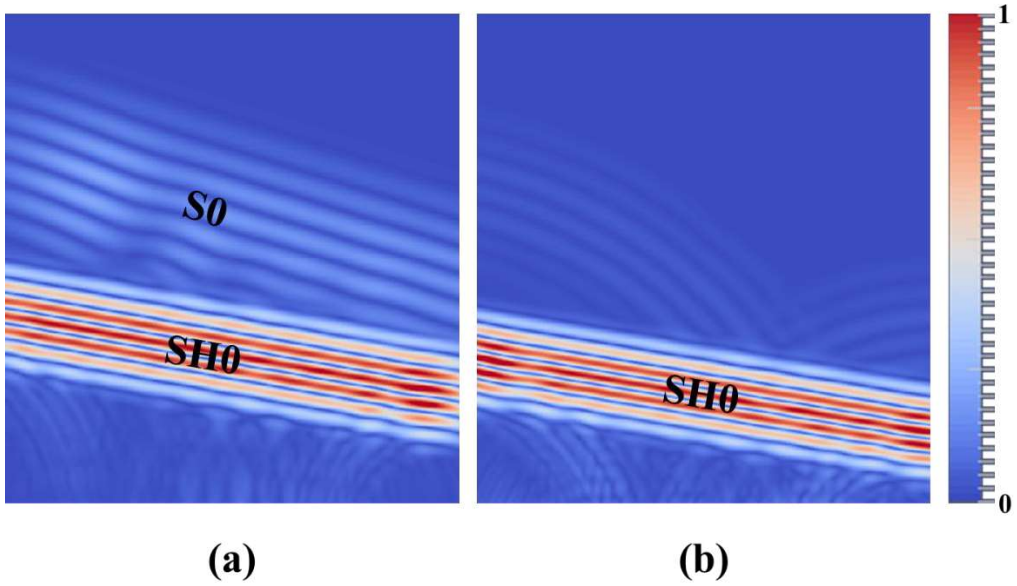

Figure 4.25: Simulation of 10° plane wave transmitted using (a) classic transduction setup and (b) S0 cancelling setup.

wave that would be otherwise excited when applying the delay laws to create a plane wave at a desired angle. There are only negligible residual S0 waves left from the first and last elements of the array.

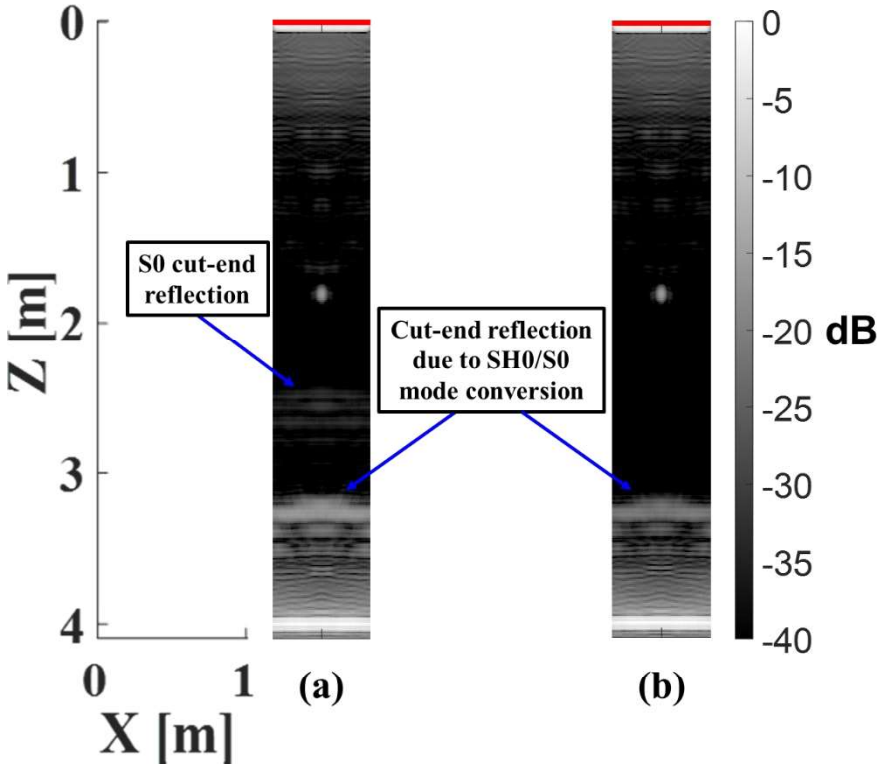

Figure 4.26: FE comparison of PWI reconstructions of pipe with 0.2 λ_{SH0}, 75 % through wall thickness deep crack at 1.8 m axial distance from the array. PWI reconstructions were obtained using: (a) classic transduction setup and (b) S0 cancelling setup. Images are in the form of unwrapped pipe.

A convenient way to quantify the reduction of the S0 related artefacts in the final reconstruction is to measure an intensity drop of the S0 reflection from the cut-end of the pipe, which results in a false cut-end echo in the image. Additionally, some of the energy of SH0 and S0 plane waves mode converts during the reflection from the cut-end of the pipe. The SH0 mode converts to the S0 mode and S0 converts to SH0. The artefacts caused by both mode-converted waves appear in the same location in the reconstructed image due to reciprocity. Therefore, the suppression of the S0 transmission should result in a noticeable reduction in the SH0-S0/S0-SH0 artefact as well. Figure 4.26 compares the PWI reconstructions obtained using (a) the classic transduction and (b) the S0 cancelling transduction. It reveals that there is at least 20

dB reduction (from -30 dB to -50 dB) of the S0 false cut-end echo artefact to levels undistinguishable from the background noise level, which indicates the complete S0 suppression. Furthermore, there is around -5 dB reduction (from around -16 dB to -21 dB) of the SH0 to S0 and the S0 to SH0 false cut-end artefact due to reduction of the S0 to SH0 contribution, because the S0 incident wave is completely suppressed. The biggest contribution to this artefact is from the SH0 to the S0 mode conversion which is unavoidable, as SH0 is the probing wave. Apart from the reduction of unwanted artefacts in the reconstructed images, the S0 suppression method does not have a negative impact on resolution as the number of transmitting/receiving SH0 elements oriented in the circumferential direction remains the same. Therefore, if there is a need to eliminate all the artefacts caused by illumination with S0 plane wave, the presented method could be implemented without a negative impact on quality of the reconstructions.

The concept has not been implemented experimentally due to the limitations of the available phased array controller. It was intended to perform the S0 cancelling with the use of the spare row of transducers in the transduction ring used for experiments. This way the number of transducers oriented in the circumferential direction for SH0 excitation would remain unchanged. However, the Verasonics Vantage™ 32LE phased array controller can only transmit waves on 64 elements during acquisition. Alternatively, it was considered to rotate every other element of the active transducer row by 90° to allow S0 cancelling this way. This configuration would imply the use of 25 kHz centre frequency to provide sufficient spatial sampling needed to avoid grating artefacts with only 20 elements transmitting SH0 mode. However, such low frequency was significantly outside the operating frequency range of the phased array controller and would require longer transmission times than permitted (due to large wavelength and required delays for plane wave excitation). Therefore, experimental validation is

not provided here.

4.10. Discussion on generalisation of the results

4.10.1 Axial location

In order to test the influence of the axial position of a crack along the pipe on its indication reconstructed using PWI, a 50 % through wall thickness deep, 1.55 λ_{SH0} long (15 % of the pipe circumference) crack was simulated in the FE model described in section 4.3 by disconnecting the elements at a range of axial locations. The zero volume cracks were simulated from 1.5 m to 3.5 m away from the array in steps of 0.5 m. Figure 4.27 presents the PWI reconstructions of images for a pipe with cracks at all considered axial locations.

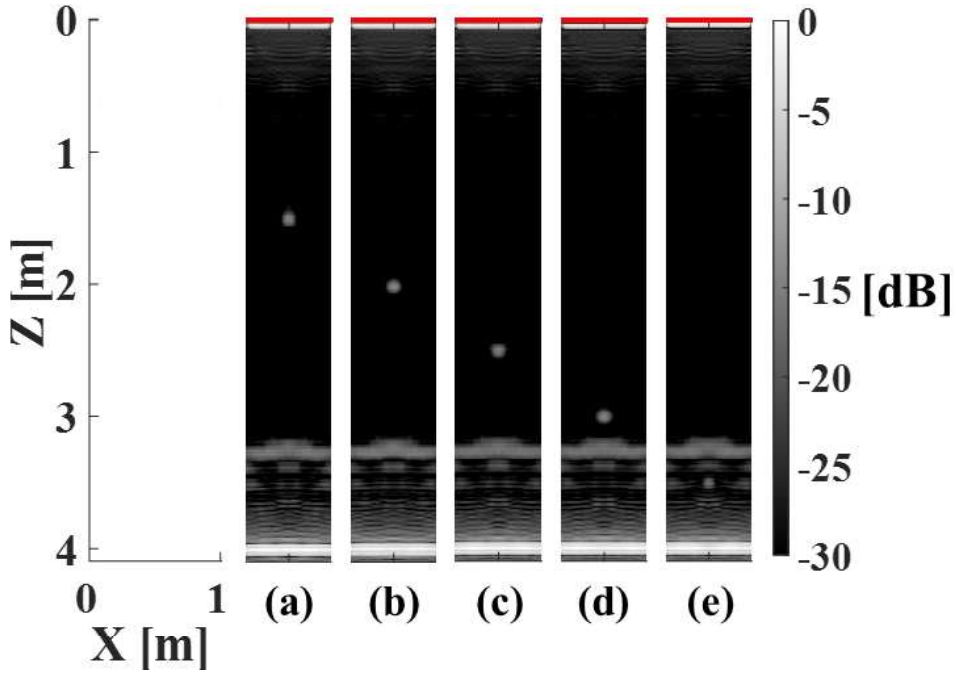

Figure 4.27: PWI reconstruction of the pipe with 50 % through wall thickness deep, 1.55 λ_{SH0} long cracks at axial locations between 1 m and 3.5 m. The reconstructions are based on ultrasonic data from the FE simulations.

To investigate the influence of the axial position on the resolution, the crack length estimates using the FWHM method were plotted against the distance in Figure 4.28.

The length of the crack indication slightly increases with the increase in the axial position of the crack for axial positions between 1.5 m and 3 m. This is expected, as with the distance from the array, the angular range on reception is slightly decreasing due to the constant number of helical paths used for focusing on reception. This results in a gradual decrease in the range of angles used for imaging on reception and consequently a gradual decrease in resolution. As mentioned in section 4.5, this can be mitigated by increasing the number of helical paths used for focusing as the axial distance increases, however for short pipes, like the one considered here, the constant number is sufficient.

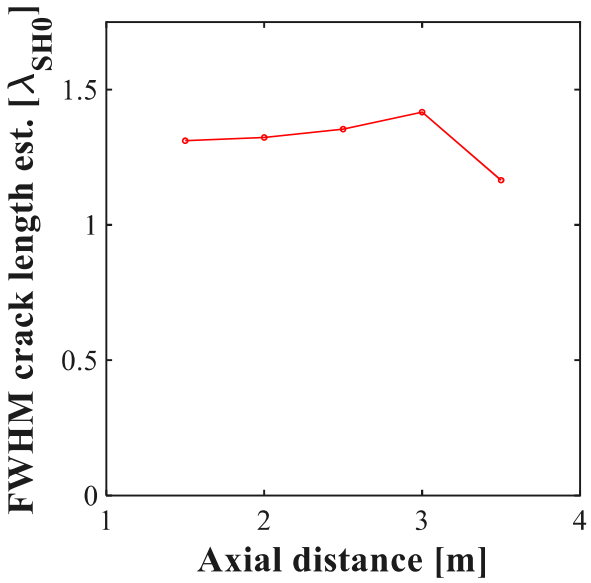

Figure 4.28: The FWHM crack length estimates from the PWI reconstructions of the pipe with 50 % through wall thickness deep, 1.55 λ_{SH0} long cracks at axial locations between 1 m and 3.5 m. The results are based on the FE data.

Additionally, as discussed in sections 2.4.4 and 4.4, there is a phase velocity error associated with the use of the plate-pipe approximation which affects the waves propagating at larger angles with respect to the central axis of the pipe. The error is very small, especially given the limited angular ranges on transmission and reception, hence its contribution in the considered pipe is negligible. However, because the error is proportional to the propagation distance (i.e. error is expressed as a percentage of the phase velocity), it is expected to contribute to the increase in the lateral size of a

defect indication in longer pipes. Therefore, when using guided wave PWI in long pipes, it would be desired to correct for the SH0 mode phase velocity variations with the angle of propagation.

In the case of a crack at 3.5 m away from the array, a substantial decrease in the FWHM crack length estimate is observed. This is caused by the interaction of the crack indication with artefacts due to SH0 to S0 and S0 to SH0 mode conversions at the cut-end. Therefore, the reliable lateral length estimation of cracks near the false echo may not be possible with PWI. Defect detection and sizing in this area can be aided with CSM or PWI with reduced transmission angles to avoid the formation of a false echo at the cost of a decreased resolution. It is worth noting that while the cut-ends are not very common in pipelines, the more common flanged joints are also very strong reflectors and they would create similar echoes. Butt welds are the most common joint type between pipeline sections. They are much weaker reflectors (i.e. around 22.5 % of the cut-end value), hence the false echoes due to mode conversion would not be problematic because only a fraction of the energy undergoes mode

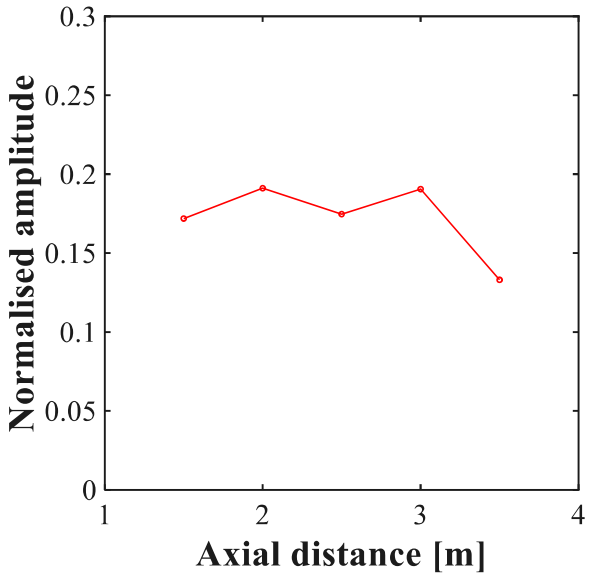

Figure 4.29: The maximum amplitudes of crack indications normalised by the cut-end echo amplitude measured from the PWI reconstructions of the pipe with 50 % through wall thickness deep, 1.55 λ_{SH0} long cracks at axial locations between 1 m and 3.5 m. The results are based on the FE data.

conversion. However, the SH0 mode weld echoes (without mode conversion) would be noticeable, as it is the case in regular GWT.

Next, the influence of the axial position of a crack on its indication amplitude in the reconstructed images was investigated. Figure 4.29 presents a plot of the maximum crack indication amplitude normalised by the amplitude of the cut-end echo against the axial position along the pipe. The amplitude is relatively constant for axial positions between 1.5 m and 3 m with fluctuations of around 10 %. The recorded amplitudes are in a good agreement with the results presented in section 4.8. Therefore, it can be concluded that the axial position of the crack does not have a substantial impact on its indication amplitude. As before, it can be noted that the indication of the crack at 3.5 m away from the array differs from indications at other positions. Its amplitude is substantially lower compared to the other four crack positions, indicating some destructive interference with the mode converted waves reflected from the cut-end. Hence, indications of defects located near the false cut-end echo should not be used for defect characterisation in PWI with wide angular range on transmission.

4.10.2 Different frequency of excitation and pipe sizes

The generalisation of the CSM results to different frequencies of excitation and pipe sizes was thoroughly discussed in [25,58], therefore only a brief discussion based on these studies is provided here. Since CSM is PWI with only the 0° probing wave, it is reasonable to assume that these results are valid for PWI with wider transmission angles.

It was shown that the shape of the FWHM crack length plot for CSM with axes normalised by wavelength does not change with the frequency of the probing wave. Therefore, translating these results to PWI, the resolution limit of 0.9 λ_{SH0} is the same for all frequencies, but because the wavelength is a function of the frequency this

resolution limit is 58 mm at 50 kHz and, for example, 116 mm at 25 kHz. One has to also remember that the error in phase velocity due to plate-pipe approximation is inversely proportional to the frequency. Hence, using lower frequencies will result in larger errors which can affect focusing performance and lead to blurring in the reconstructed image. Therefore, care must be taken when choosing the excitation frequency.

When it comes to the amplitude of crack indication, Davies and Cawley (2009) [25] reported that it remains constant with frequency for through wall thickness cracks of the same circumferential length as a fraction of the wavelength. However, it was shown that the amplitude of part-depth crack indication is proportional to the frequency of excitation. This is because the reflection amplitude of the SH0 mode from a part-depth crack depends on the crack depth as a fraction of the incident wavelength and as a fraction of the wall thickness [114].

Finally, it was demonstrated that using the same excitation frequency in a pipe of a different diameter with a crack of the same absolute circumferential length in metres results in practically identical amplitude and crack indication length. Therefore, it was concluded that the amplitude and length of a defect indication depends on the absolute size of the defect rather than the proportion of the circumference that it occupies.

From the above discussion it can be concluded that synthetic focusing imaging methods can be successfully deployed for guided wave inspection of pipes of different diameters using a range of different frequencies.

4.11. Summary

In this chapter the performance of synthetic focusing imaging methods introduced in chapter 3 was compared and evaluated using FE and experimental studies. The key performance indicators were lateral resolution and SNR.

First, the FE model and experimental setup were outlined. This was followed by the FE study on selection of the optimal imaging parameters for CSM, TFM, and PWI. It was observed that the coherent noise and the angular reflectivity of the SH0 mode limit the range of angles on transmission and reception that can be effectively used for focusing during reconstructions. TFM, FMCPWI and PWI reconstructions suffer from the artefacts caused by the unwanted S0 mode excited during the transmission. It was shown that by the reduction of the transmission angles in PWI to the range between -28° and 28° the coherent noise due to the S0 mode can be successfully mitigated. The same can be achieved in TFM by filtering out the waves travelling at angles outside this range from the FMC data. It was concluded that the optimal number of helical paths used for imaging on reception is 3 for all the considered methods.

Subsequently, the comparison of resolution, sizing capabilities and SNR was conducted. The key conclusions were that PWI, FMCPWI and TFM achieve comparable resolution of 0.9 λ_{SH0} which is superior to the CSM resolution of 1.4 λ_{SH0}. The FMC based methods achieve a substantially lower SNR compared to methods involving plane wave acquisition (PWI and CSM). Consequently, TFM and FMCPWI were insensitive to smaller notches in experiments, indicating that these techniques should not be deployed without incoherent noise mitigation methods. While PWI and CSM achieved sufficient SNR to detect the smallest introduced notches, PWI achieves better resolution with significantly higher overall SNR making it a more attractive choice for pipe GWT. Therefore, PWI was used in the remainder of this chapter. The experimental results supported validity of the FE findings.

This was followed by the FE and the experimental study on the crack through wall thickness depth estimation from the PWI reconstructions. It was shown that it is possible to estimate crack depth, provided its lateral length is longer than the resolution limit.

Next, a novel PWI transduction setup was evaluated in the FE study. It suppresses the transmission of the unwanted S0 mode in PWI and hence reduces some coherent noise artefacts further improving the overall SNR. The chapter concluded with discussion on generalisation of the results for different axial positions of a crack, different frequencies and pipe diameters.

This page intentionally left blank

5. Synthetic focusing imaging in pipe guided wave testing using a partial circumferential array

5.1. Introduction

So far this thesis considered guided wave synthetic focusing imaging in pipes deployed using fully circumferential transduction rings. As discussed in section 1.1, it is sometimes the case that the access to the full pipe circumference is limited during inspection of hard-to-reach structures. Therefore, in this chapter, the influence of reducing the circumferential phased array extent on guided wave imaging is investigated.

The previous chapter concluded that, amongst the considered methods, PWI is the most attractive technique for high resolution synthetic focusing imaging in pipe GWT. Hence, only PWI is considered here, however, because of the similarities between PWI and TFM, the findings can be assumed valid for the latter technique.

The chapter begins with a theoretical discussion on the influence of limited circumferential access on synthetic focusing imaging in section 5.2. This is followed by a description of the Finite Element (FE) model and experimental setups in section 5.3. Section 5.4 presents and discusses the practical effects of a partial circumferential array on reconstructed images using PWI with the focus on the resolution and SNR. The chapter concludes with the summary presented in section 5.5.

Parts of this chapter have been adapted and extracted from the publication [P2], which was submitted to IEEE® Transactions on Ultrasonics, Ferroelectrics, and Frequency Control but has not been published at the time of writing this thesis.

5.2. Limited Circumferential Array Theory

This section presents the extension of the theory introduced in section 3.6 for the fully circumferential synthetic focusing imaging. Here the concern is with imaging using partial circumferential phased arrays.

In principle, the reduction of the circumferential extent of the transducer array will have a negative effect on the image reconstructed using synthetic focusing imaging techniques. Reduced array extent impacts: (a) the k-space available for imaging and (b) the performance of the phased array.

When considering the influence of a partial circumferential array on the k-space, the transducer array has to be treated as a spatial sampler [202]. In the limited array configuration, the aperture is not quasi-infinite as was the case in the fully

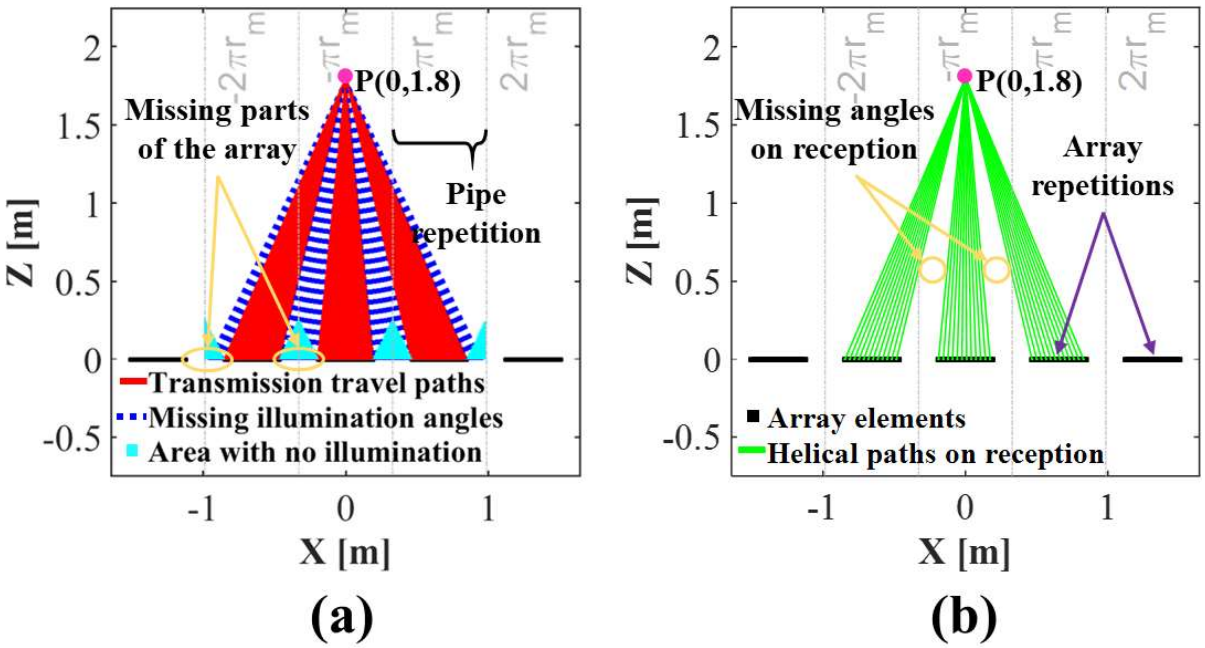

Figure 5.1: Unwrapped pipe display outlining the (a) transmission and (b) reception travel paths to/from the arbitrary point (pixel) P(0 m ,1.8 m) for 60 % circumferential array setup. The schematic shows 5 repetitions of the pipe circumference; the vertical grey dashed lines mark the borders between the pipe repetitions. The angular range between -28° to 28° on transmission (a) and 3 helical paths on reception (b) were used in the diagram. The figure illustrates the missing angular ranges due to the limited circumferential array and shows the area with no plane wave illumination in the presented array setup. r_m is the mean radius of the pipe. [P2]

circumferential configuration, and consequently not all the backscattered waves can be recorded. The partial circumferential array becomes a quasi-infinite series of finite apertures which means that for an arbitrary point P in the ROI periodic parts of the transmission/reception angular range will be missing as outlined in Figure 5.1.

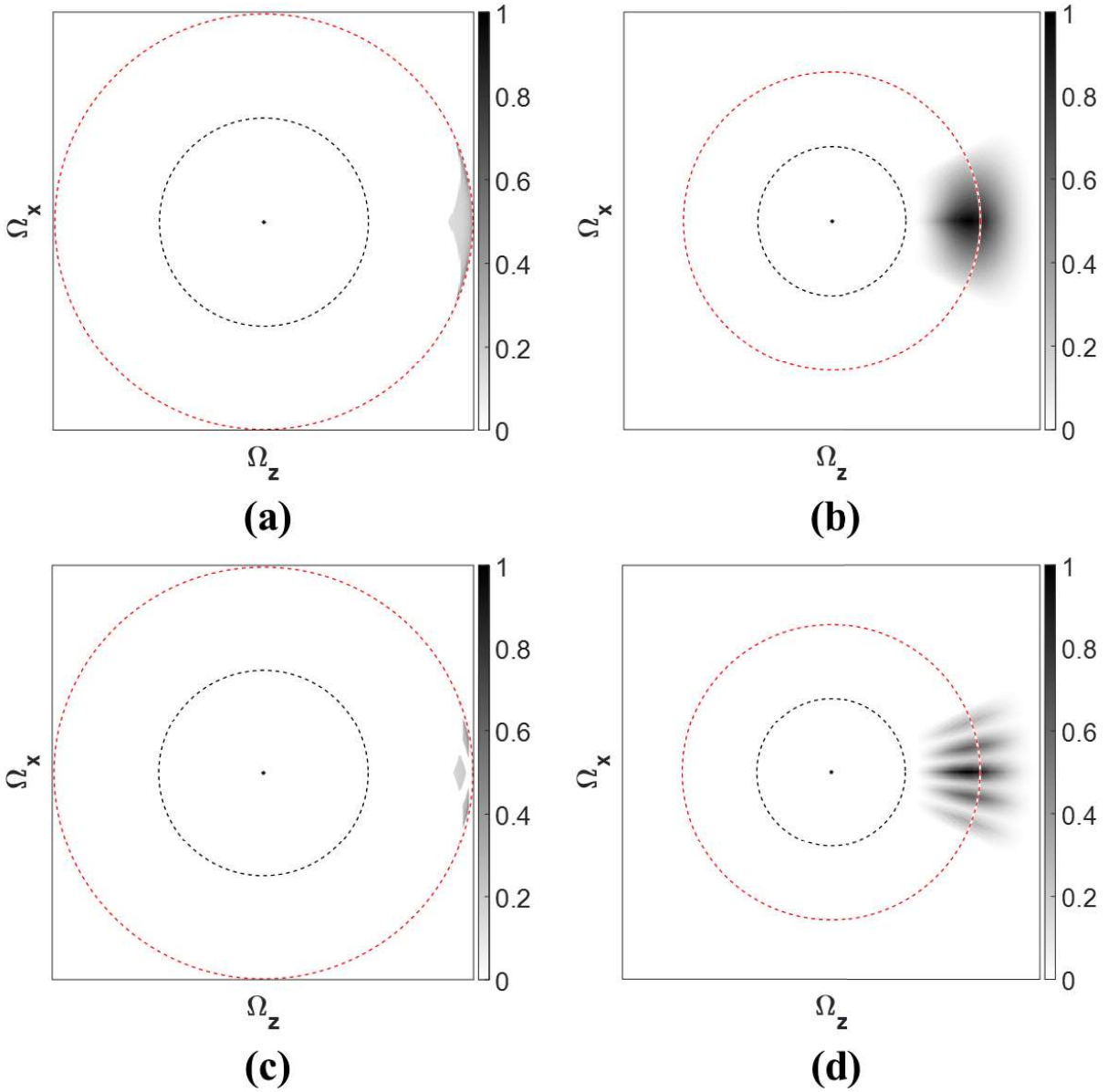

Figure 5.2: Comparison of k-space available for imaging in pipe guided wave PWI inspection with fully circumferential array (a-b) to the array extending on 60 % of the pipe circumference (c-d). The k-space plots are for a point 1.8 m away from the array aligned with the centre of the array. Transmission plane wave angles were between -28° and 28° and 3 helical paths on reception were used for reconstruction. The plots present normalised sum of contributions from all transmission/reception direction pairs for all considered temporal frequencies. The excitations considered were: (a, c) 50 kHz monochromatic excitation and (b, d) 5-cycle Hann windowed 50 kHz centre frequency tone burst. [P2]

The missing transmission/reception angular range limits the portion of the k-space disc that can be populated from the measurements. Figure 5.2 compares the k-space available for imaging with a fully circumferential array to the array extending only on 60 % of the pipe circumference for 50 kHz monochromatic (a, c) and 5-cycle Hann windowed (b, d) excitations. The k-space mapping was performed using the method outlined in section 3.6. Limiting the array circumferential extent leads to an uneven population of the k-space as a consequence of the gaps in the angular ranges of transmitted and recorded waves. As expected, the Hann windowed excitation, providing a broader temporal frequency range, results in better coverage of the k-space compared to the monochromatic excitation. The FE and experimental studies in section 5.4 will answer the question whether a broader temporal frequency range provides enough additional k-space coverage to make up for the missing spatial sampling due to the limited circumferential extent of the array.

In the case of a fully circumferential array, each point around the pipe with the same axial distance from the array has the same transmission/reception angular range. With the constant number of helical paths considered on reception, the angular range on reception gradually decreases with the axial distance. If an array is attached to only a portion of the circumference, the transmission and reception angular ranges will vary depending on the location around the pipe. This is shown in Figure 5.3(b,c), where parts of the k-space retrieved through imaging using partial phased array are shown for two arbitrary points in the domain. Consequently, the varying angular range through the pipe results in an uneven coverage of the ROI, which can be presented in the form of the k-space coverage map (Figure 5.3(a)). The coverage map for each point in the ROI indicates the fraction of the Ewald limiting circle area available for imaging. The values are normalised by the highest value i.e. 1 means the highest percentage of k-space area available for imaging within the ROI and 0 means no k-space available

for imaging (e.g. due to lack of illumination).

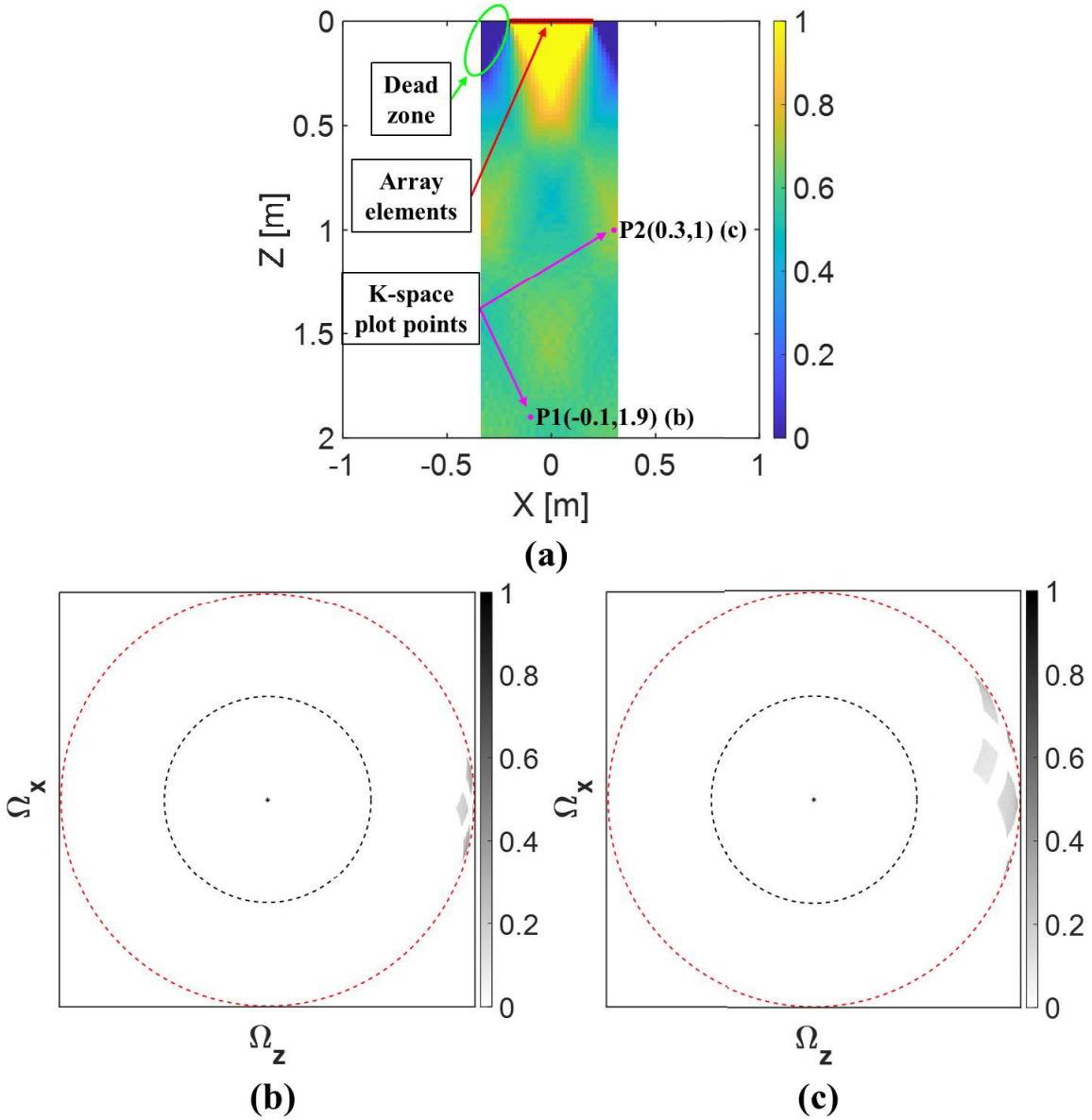

Figure 5.3: (a) Normalised k-space coverage map in the form of unwrapped pipe display presenting the percentage of Ewald's limiting circle available for imaging for each point (pixel) in the ROI when 60 % circumferential array is used; (b,c) are k-space plots, comprising a normalised sum of contributions from all transmission/reception direction pairs, for two arbitrary example points P1(-0.1 m, 1.9 m) and P2(0.3 m, 1 m) respectively. For simplicity, the monochromatic 50 kHz excitation is considered in this figure. The angular range on transmission is -28° to 28° and 3 helical paths are considered on reception.

According to Figure 5.3(a), the region immediately ahead of the array and close to its centre line gets the best k-space coverage. This region is illuminated with all the transmitted plane wave angles, and with a set number of helical paths on reception it provides the widest angular range on reception. When moving away from the array or

to the side of its centre line the number of plane wave angles that illuminate a given point in the ROI and/or its reception angular range decrease. This results in a decrease of the k-space available for imaging away from the array as is the case in the classic 2D bulk wave array imaging. A substantial decrease in the k-space coverage is particularly apparent in the first 0.6 m of the ROI. One can notice that near the axial position of the array, in the position 180° around the pipe circumference from the centre of the array, exists a 'dead zone' with no spatial components available for imaging. This is the consequence of limited plane wave transmission angles to between –28° and 28°. As the result, no transmitted waves can reach this region as outlined in Figure 5.1(a). In practice, the region immediately near the array could not be inspected even using a fully circumferential array because the transducers cannot receive while they are still transmitting. Therefore, this part of the pipe cannot be inspected with the proposed synthetic focusing imaging setup, however, inspection of this 'dead zone' can be performed locally using commercially available equipment (e.g. QSR® by Guided Ultrasonics Ltd. [1,203]) with only partial circumferential access.

Throughout the pipe a slight chequered pattern can be seen in the k-space coverage map. Due to the fixed transmission angular range in PWI and limited circumferential extent of the array there are periodically appearing regions with increasing and decreasing transmission angular range which result in increasing/decreasing k-space coverage. When considering an arbitrary point P, as it is moved axially along the array centreline in the positive z-direction away from the array, the range of incident plane wave angles that illuminate point P decreases. This occurs because each transmitted wave does not span the entire circumference, as was the case with the fully circumferential array, causing some incident waves to simply miss point P. The decrease in the incident angular range leads to fewer spatial frequencies being available for imaging. As point P is moved even further away, some of the incident waves

transmitted at higher angles begin to illuminate point P after traveling in helical directions wrapping around the circumference once. This results in an increase in the incident wave angular range and consequently an increase in the available spatial frequencies for imaging. This pattern repeats periodically as P is moved throughout the pipe, resulting in a chequered pattern in the k-space coverage map. The author also appreciates that the uneven coverage of the ROI leads to variation in the pixel intensity in the reconstructed images. Results elsewhere [44] have shown that it is possible to correct for this effect but the benefit was minimal, and this was therefore not considered further.

The second aspect of limited circumferential access is related to the performance of the phased array, especially in its focusing capabilities. Although focusing is performed synthetically in post processing, the same principles as in the case of classic physical phased array focusing apply to synthetic focusing imaging. Therefore, parameters of a transducer array, such as the number of elements and aperture length, have a direct influence on the reconstructed image quality and achieved resolution. More elements provide better beam directionality and improved focusing (assuming constant element width and spacing). Therefore, decreasing the circumferential extent of the array has a negative impact on focusing and consequently on the resolution of the reconstructed image as shown in [204-206]. A small circumferential extent can lead to an increase in the side lobe amplitude causing artefacts in the reconstructed images [206]. Having fewer elements also decreases the maximum steerable angle. This being said, the setup considered in this thesis would not experience the decrease of the maximum steerable angle due to the very small array pitch of 0.3 λ_{SH0}. The aggregate effect of an uneven k-space coverage and decreased phased array performance on resolution will be investigated later in 5.4.

5.3. Methodology – finite element model and experimental setup

The finite element study was conducted using the model introduced in section 4.3. The outline of the model is presented in Figure 5.4. Here circumferential extents of the phased array between 20 % and 100 % were modelled. Three circumferential positions of the crack with respect to the centreline of the array were considered: 0°, 90° and 180°. Zero-axial length, part-circumferential, part-depth planar cracks of 3 % to 40 % circumferential extents (0.3 λ_{SH0} to 4.1 λ_{SH0}) and 50 % through wall thickness depth were modelled by disconnecting adjacent elements.

The setup used in the experiments was the same as the one described in section 4.4 and it is schematically outlined in Figure 5.4. For each notch length the ultrasonic data using different array circumferential extents (20 % to 100 %) and positions (0°, 90° and 180°) was collected together with data used in chapter 4 during the same experiment. The limited circumferential array was simulated by using only parts of the transduction ring array. For each considered array circumferential extent the array was virtually rotated by setting the array centre at 0°, 90° and 180° position with respect to the notch centre.

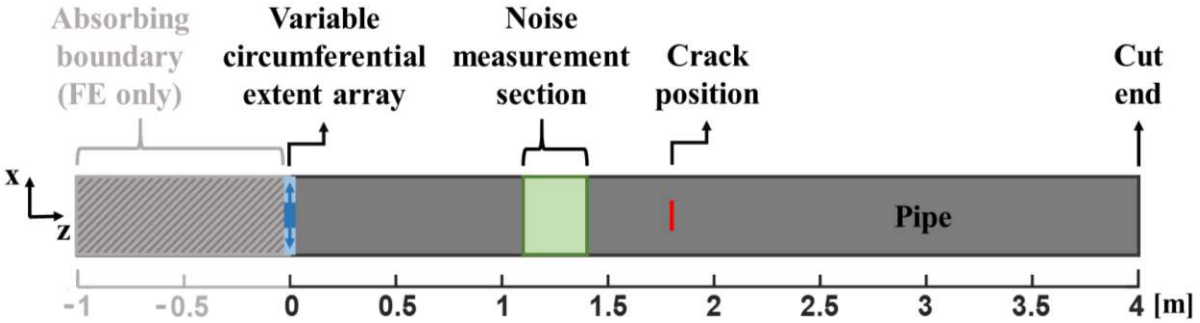

Figure 5.4: The outline of the guided wave inspection setup considered in the FE and experimental studies.

In the experiments FMCPWI was used for imaging instead of regular PWI. This is because PWI suffered from unexplained coherent noise when using array circumferential extents between 70 % and 80 %, regardless of the circumferential position of the array. Figure 5.5

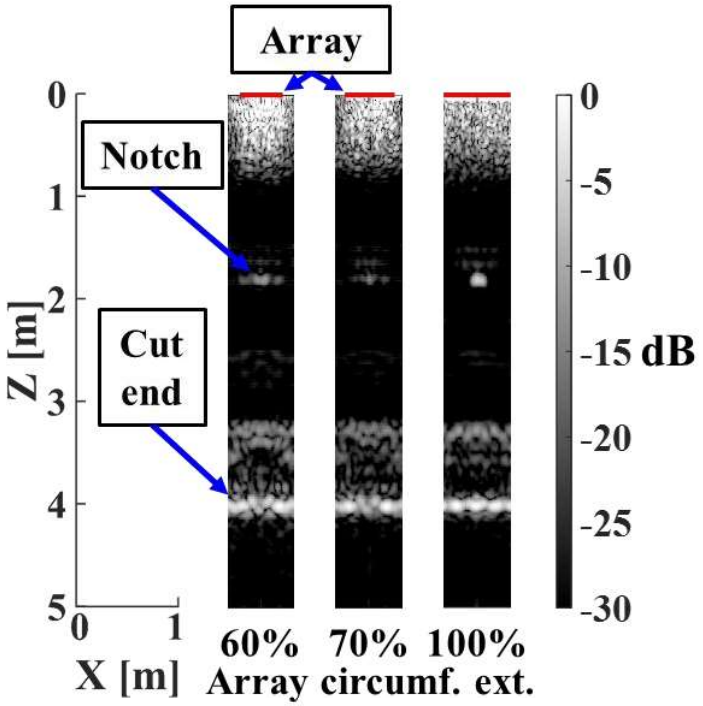

Figure 5.5: The comparison of unwrapped pipe PWI reconstructions of 2.1 λ_{SH0} long (20 % of the circumference), 50 % through wall thickness deep crack at 1.8 m axial distance from the array at 0° crack circumferential positions using a range of array circumferential extents. The reconstructions are based on the experimental data.

compares PWI reconstructed images of an arbitrary 2.1 λ_{SH0} long notch with 60 %, 70 % and 100 % array circumferential extents. In reconstructions using 60 % and 100 % array circumferential extents, the notch indications represent the notch length with expected accuracy, despite some coherent noise observed near defect indication for 60 % array extent. The notch indication in the PWI image reconstructed using 70 % array circumferential extent is of much lower amplitude compared to the two other reconstructions and it does not represent the notch length accurately. The attempt to estimate the length of the notch from the reconstruction leads to its severe underestimate. The same phenomenon was observed for all considered notch lengths and positions around the circumference with respect to the centre of the array. The most likely cause of the issue is the destructive interference of the coherent noise with waves scattered from the notch. The phenomenon did not appear in the FE simulations, hence the problem was related to the experimental setup. The author conducted a

thorough investigation into the problem.

First, the spare row of transducers in the ring was used in the acquisition process to rule out the faulty transducers. This had virtually no influence on the results and the coherent noise was still present. Subsequently, the influence of transduction ring axial and circumferential positions as well as the influence of balancing coefficients was investigated, however no improvement was observed. The issue persisted regardless of the frequency of excitation. Next, the setup was modified so that waves were transmitted with the Verasonics Vantage™ 32LE phased array controller, but the response was acquired via the HS5 Handyscope paired with Olympus amplifier. This way it was confirmed that the presence of the coherent noise is associated with the transmission stage of the acquisition process as data acquired with the Handyscope still contained the noise. Subsequently, the filtering of waves travelling at angles outside the range of -28° and 28° from the PWI ultrasonic data was implemented in the same fashion as the method presented in section 3.8 for FMC based imaging techniques. The filtering did not remove the coherent noise. Finally, the author conducted an extensive FE study in the search for the potential cause of the coherent noise, however neither changing transducer element size, simulation of the transducer imbalance nor changing the position of the crack yielded the results resembling the observed issue. Therefore, it was speculated that the coherent noise is likely caused by severe variations between the channel output levels of the phased array controller. Unfortunately, only one low frequency phased array controller capable of controlling the 40 element array was available, hence the FCMPWI was used in experiments since the FMC ultrasonic data did not suffer from the same issue. Because FMCPWI was shown in the previous chapter to achieve insufficient incoherent SNR to detect small subwavelength defects, only notches longer or equal to 0.6 λ_{SH0} were considered in this chapter.

Throughout the experiments and FE studies the range of transmitted waves was kept

between -28° and 28° to avoid unwanted circumferential guided wave modes, and the transmission angular step was kept at 1°. 3 helical paths were used for focusing on reception and a 50 kHz centre frequency, 5-cycle Hann windowed tone burst excitation was used.

The resolution and SNR measurements were conducted in the same fashion as described in section 4.2.

5.4. Results and discussion

This section evaluates and compares the performance of the PWI method using different circumferential extents of the array. The comparison is based on PWI (FE) and FMCPWI (experiments) reconstructions of a range of part-circumferential part-depth cracks/notches at three positions around the pipe circumference.

5.4.1 Finite element results

The PWI reconstructions of a 1.3 λ_{SH0} long, 50 % through wall thickness deep crack at an arbitrary 1.8 m axial distance from the array obtained using array circumferential extents between 20 % and 100 % for (a) 0°, (b) 90° and (c) 180° crack circumferential positions with respect to the centreline of the array are presented in Figure 5.6. According to the figure, cracks can be reliably detected and located using array circumferential extents of 50 % and above regardless of their position around the pipe circumference. With the decrease in the array circumferential extent there is an increase in coherent noise artefacts. For arrays extending on to less than a half of the circumference, the crack indication cannot be distinguished from these artefacts, which hinders reliability of pipe inspection with such array extents. The reasons for this phenomenon are the severe decrease in k-space available for imaging, the increase in the side lobe amplitude, the impaired modal control and the decreased focusing

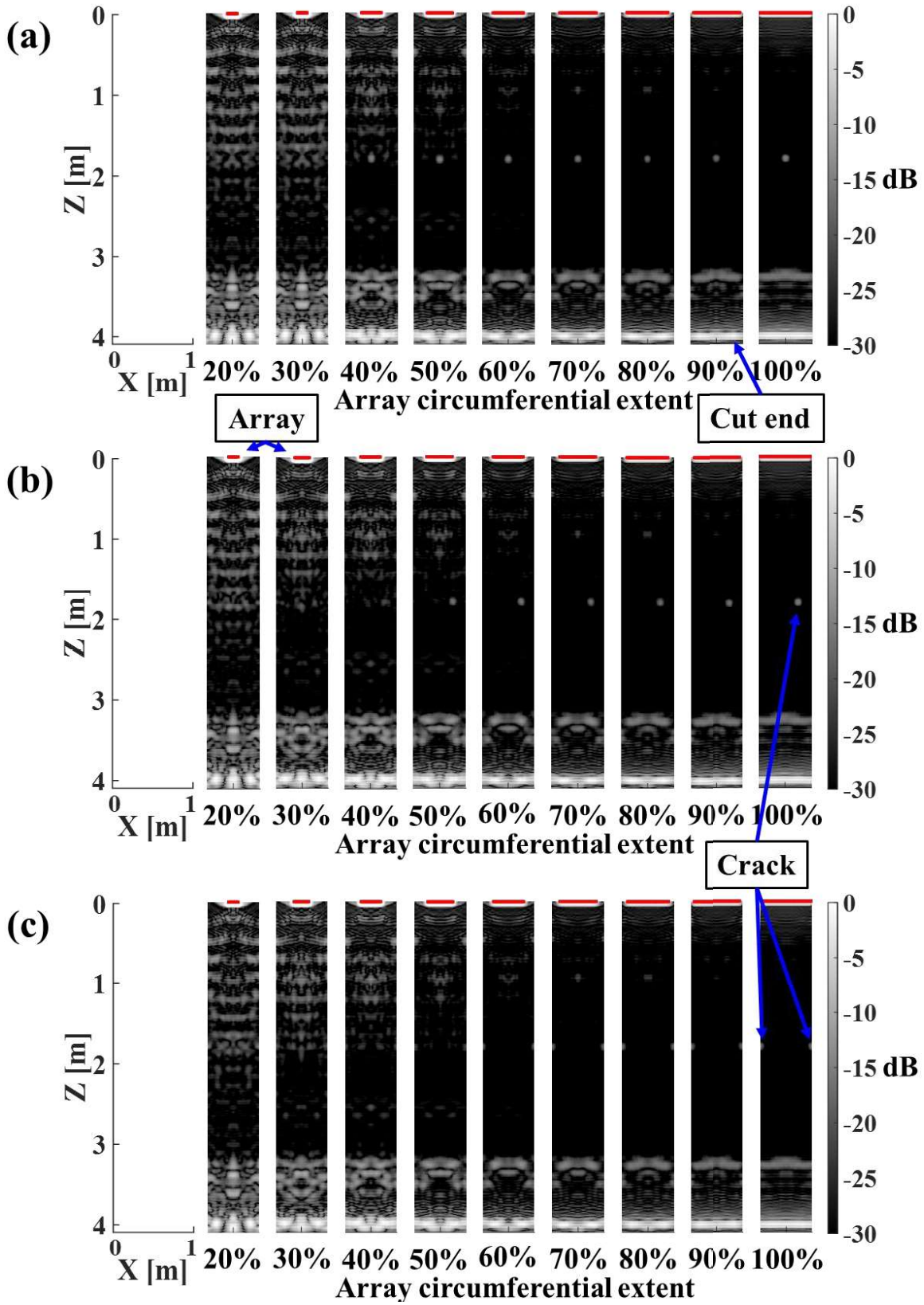

Figure 5.6: Comparison of unwrapped pipe PWI reconstructions of 1.3 λ_{SH0} long (13 % of the circumference), 50 % through wall thickness deep crack at 1.8 m axial distance from the array at (a) 0°, (b) 90° and (c) 180° crack circumferential positions using a range of array circumferential extents. The reconstructions are based on FE data. [P2]

performance, all caused by substantial decrease in aperture length and number of array elements. Therefore, only array circumferential extents above 50 % are considered in the rest of this chapter.

To assess the impact of the partial circumferential array on PWI resolution and defect sizing accuracy, FWHM crack length estimate curves were plotted in Figure 5.7 for 60 % to 100 % array circumferential extents and 0°, 90° and 180° defect positions around the pipe circumference with respect to the array centreline. The 50 % circumferential array was omitted because the coherent SNR was not sufficient to reliably size small cracks. The plots reveal that in the case of all three considered crack circumferential positions, the crack length estimate curves for all presented array circumferential extents depart from the 45° line of the ideal size estimate around the same value of 0.9 λ_{SH0}. This is the maximum achievable resolution.

The error in crack length estimate is given by the deviation of the FWHM curves from the 45° line for the perfect estimate. For a typical fully circumferential inspection, within its resolution limits, the error is less than 10 - 15 % and typically much less than that as discussed in section 4.6. The curves representing the fully circumferential array are marked with solid blue curves in Figure 5.7(a-c). According to Figure 5.7(a, c) in the case of the 0° and 180° crack positions the crack sizing error for all considered array percentage extents is within 20 %. This would mean that reducing the circumferential extent of the array only slightly decreases the crack sizing accuracy. However, as can be seen in Figure 5.7(b), for the 90° crack position, limited array circumferential extents result in a crack length estimate error exceeding the typical values for larger cracks (>2 λ_{SH0}). For these larger cracks the sizing error is inversely proportional to the array circumferential extent which indicates the negative influence of limited circumferential array on the reconstructed images. Because the inaccurate sizing appears only for one circumferential position it is taken to be associated with

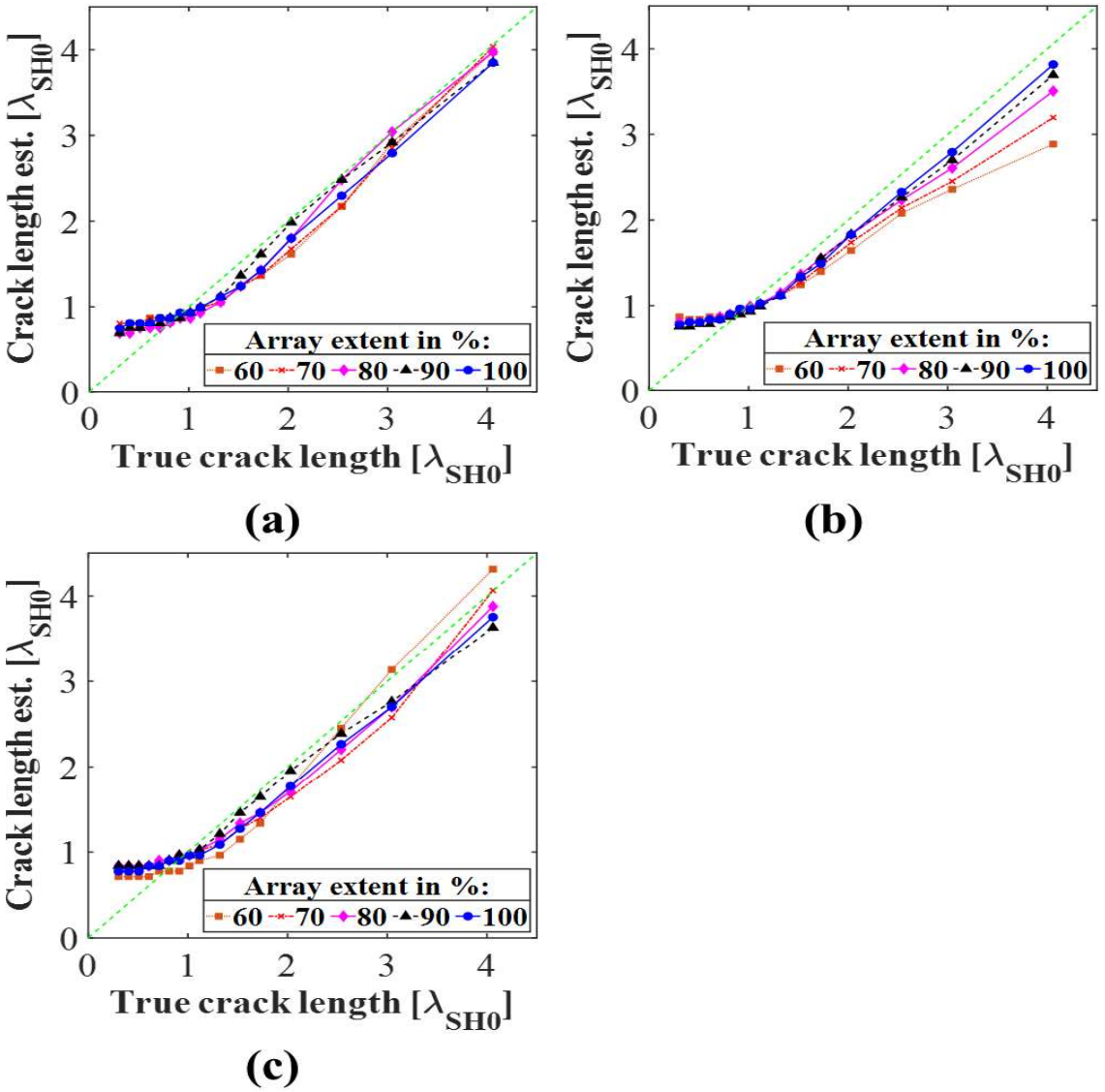

Figure 5.7: FWHM crack length estimate plots from PWI reconstructions with 60 % to 100 % array circumferential extents and (a) 0°, (b) 90° and (c) 180° crack circumferential positions with respect to array centreline. The planar cracks were 50 % through wall thickness deep at 1.8 m away from the array. The 45° green dashed lines are the perfect crack length estimate lines. The results are based on data from the FE simulations. [P2]

coherent noise caused by the limited extent of the array. This is further supported by the fact that at this position, the crack length estimate curves converge to the fully circumferential curves for the smaller defects and they depart from the 45° line of the ideal size estimate at similar values indicating comparable resolution.

The author observed and has heard from other researchers in the field that coherent noise indicated in FE simulations is sometimes higher than the actual coherent noise

observed in the experiments. While the physical nature of this difference is yet to be determined, the effect might be associated with stronger coherence of multiple signals in the simulations compared to experiments; the components of the signals that combine to make a coherent noise signal are precisely matched in simulation but could

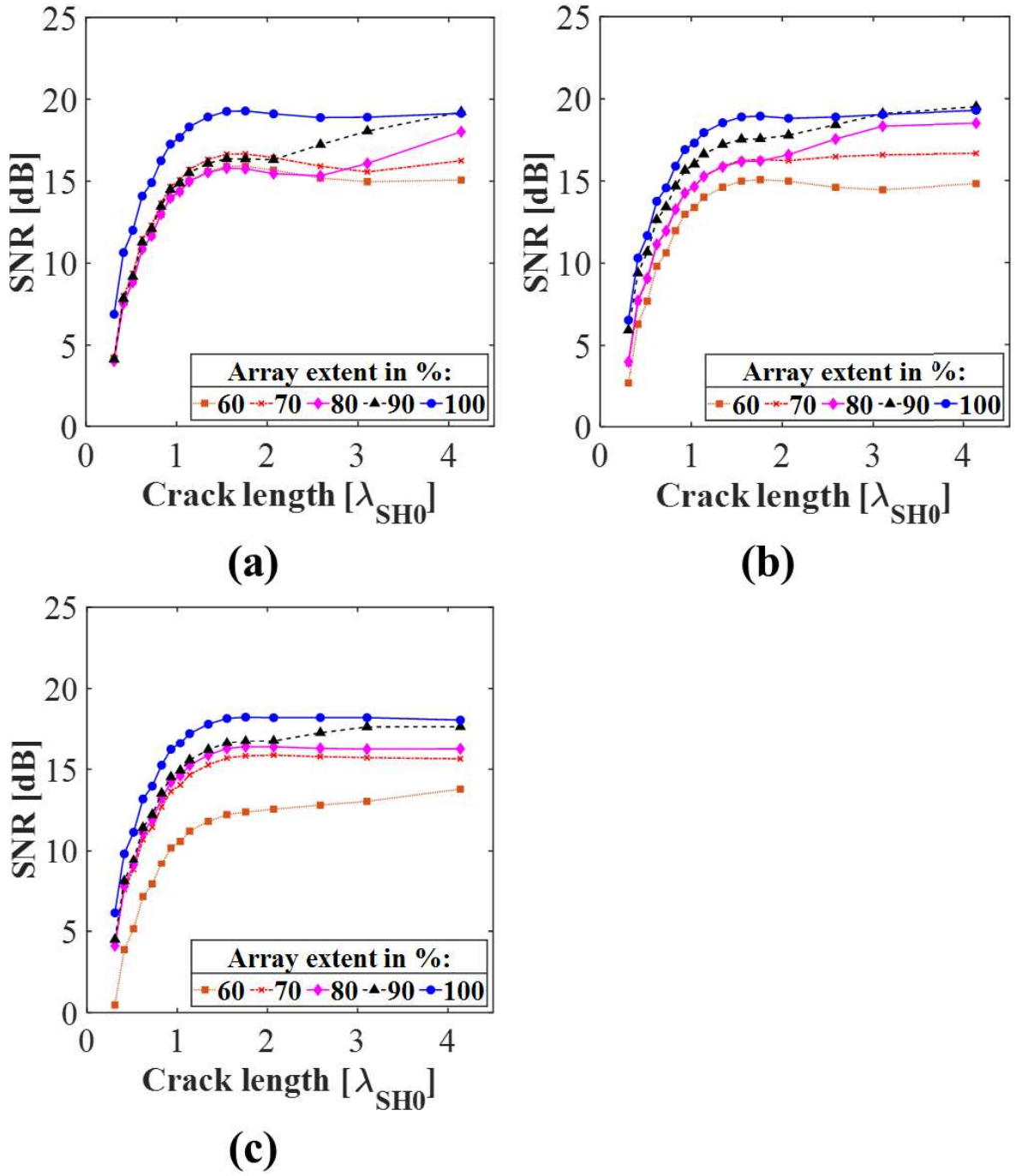

Figure 5.8: Coherent SNR versus true crack length plots obtained from PWI reconstructions using 60 % to 100 % array circumferential extents and (a) 0°, (b) 90° and (c) 180° crack circumferential positions with respect to array centreline. The results are based on the FE data. [P2]

have some phase variations in experiments. Therefore, the experimental results will determine the actual performance of the limited circumferential array and whether coherent noise indicated in Figure 5.7(b) negatively affects it.

As was discussed in section 4.6, the sizing accuracy can be improved by using the FWHM plots presented in Figure 5.7 as sizing correction charts similarly to method proposed in [198]. The exact defect size can be found by mapping the defect indication measured from the PWI reconstruction onto the FWHM curve plot for a given array circumferential extent.

In Figure 5.8, the influence of different array circumferential extents on the coherent SNR in the FE PWI reconstructions is quantified in the form of SNR plots for a range of crack lengths and (a) 0°, (b) 90° and (c) 180° crack circumferential positions. As expected, the SNR achieved using a fully circumferential array is always the highest regardless of the crack circumferential position. For larger cracks the SNR curves obtained using fully circumferential array plateau at around 18 dB. The general trend of decrease in coherent SNR with decrease in array circumferential extent is clearly visible. The SNR curves obtained using 60 % array circumferential extent are on average around 5 dB lower compared to the fully circumferential array curves.

5.4.2 Experimental results

Figure 5.9 compares the experimental FMCPWI reconstructions of a 1.4 λ_{SH0} long, 50 % through-wall-thickness deep notch 1.8 m away from the array, obtained using array circumferential extents between 20 % and 100 %. The investigated notches are at (a) 0°, (b) 90° and (c) 180° circumferential positions with respect to array centreline. The presented experimental reconstructions confirm the FE findings for PWI from the previous subsection. Array extents below 50 % are not suitable for reliable detection of notches in pipes. While it is possible to detect notches longer than a wavelength

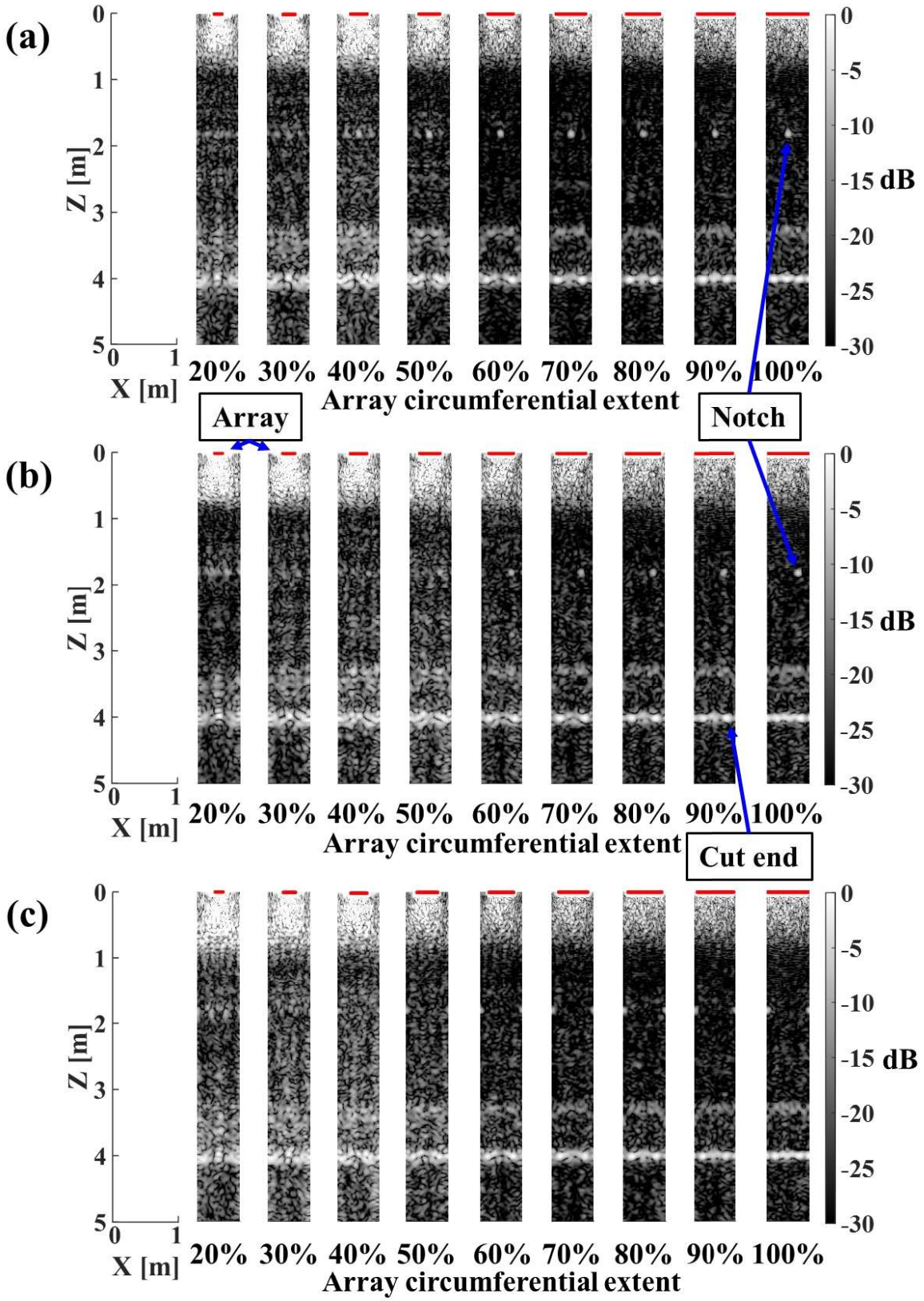

Figure 5.9: Comparison of unwrapped pipe FMCPWI reconstructions of an arbitrary 1.4 λ_{SH0} long, 50 % through wall thickness deep notch at 1.8 m axial distance from the array at (a) 0°, (b) 90° and (c) 180° notch circumferential positions using a range of array circumferential extents. The results are based on the experimental data. [P2]

with the 50 % circumferential array, it is not possible to reliably distinguish notches shorter than the wavelength from the noise which obstructs their detection. Arguably, detection of shorter notches would be possible if PWI was used instead of FMCPWI, thanks to its superior SNR. However, this needs to be confirmed experimentally in the future. The array extents of 60 % and above provide much more reliable notch detection, including sub-wavelength notches. The slightly inferior quality of experimental reconstructions compared to the FE results is caused by the additional incoherent noise which was not present in the FE study. In section 4.7, in the case of the fully circumferential array, PWI was shown to achieve significantly higher incoherent SNR compared to FMC based methods. Therefore, it is expected that if PWI was used instead of FMCPWI, much better SNR would be achieved.

To quantitatively assess the resolution and sizing accuracy of the experimental implementation of FMCPWI with limited circumferential access the FWHM crack length size estimate plots obtained from reconstructions using 60 % to 100 % circumferential extents are presented in Figure 5.10 for (a) 0°, (b) 90° and (c) 180° notch circumferential positions. The FWHM sizing curves obtained from experiments closely coincide with the FE curves in Figure 5.7 successfully validating the FE findings. The experimental curves depart from the 45° line of the ideal size estimate around 1 λ_{SH0} crack length though small variations of this value are observed for different notch circumferential positions and array extents. Therefore, it can be concluded that the lateral resolution of the imaging system with array circumferential extent between 60 % and 100 % is 1 λ_{SH0} which is marginally inferior to the resolution observed in the FE study. Both the FE and experimental curves indicate that the reduction of array circumferential extent to 60 % has limited influence on the achieved resolution. This means that the additional k-space coverage due to the temporal bandwidth of the typical Hann windowed tone burst excitation (see Figure 5.2(c,d))

makes up for the missing spatial sampling due to the limited circumferential extent of the array. According to Figure 5.10, for 70 % to 100 % array circumferential extents and 0° to 180° notch positions the sizing error is predominantly less than 20 % and usually much less than that. The 60 % array extent provides slightly inferior sizing

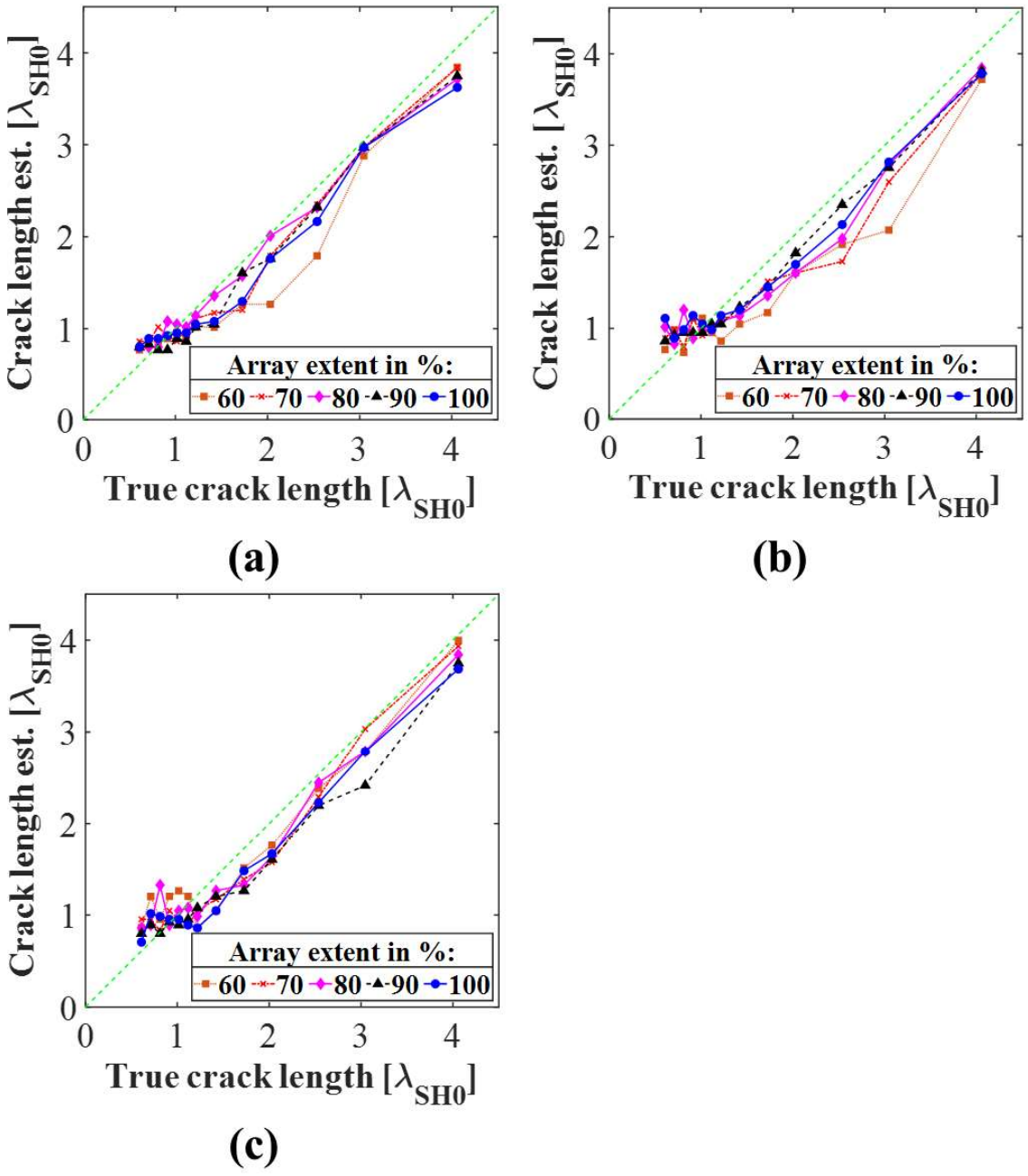

Figure 5.10: Experimental FWHM notch length estimate plots from FMCPWI reconstructions with 60 % to 100 % array circumferential extents and (a) 0°, (b) 90° and (c) 180° crack circumferential positions with respect to array centreline. The notches are 50 % through wall thickness deep at 1.8 m away from the array. The 45° green dashed lines are the ideal notch length estimate lines. [P2]

error. The increased sizing error for larger defects observed in the FE results presented in Figure 5.7(b) for 90° crack position does not appear in the experimental results.

In Figure 5.11 the influence of different array circumferential extents on the aggregate (coherent and incoherent) SNR in the experimental FMCPWI reconstructions is quantified in the form of SNR plots for a range of crack lengths and (a) 0°, (b) 90° and (c) 180° crack circumferential positions. Counterintuitively, experimental SNR

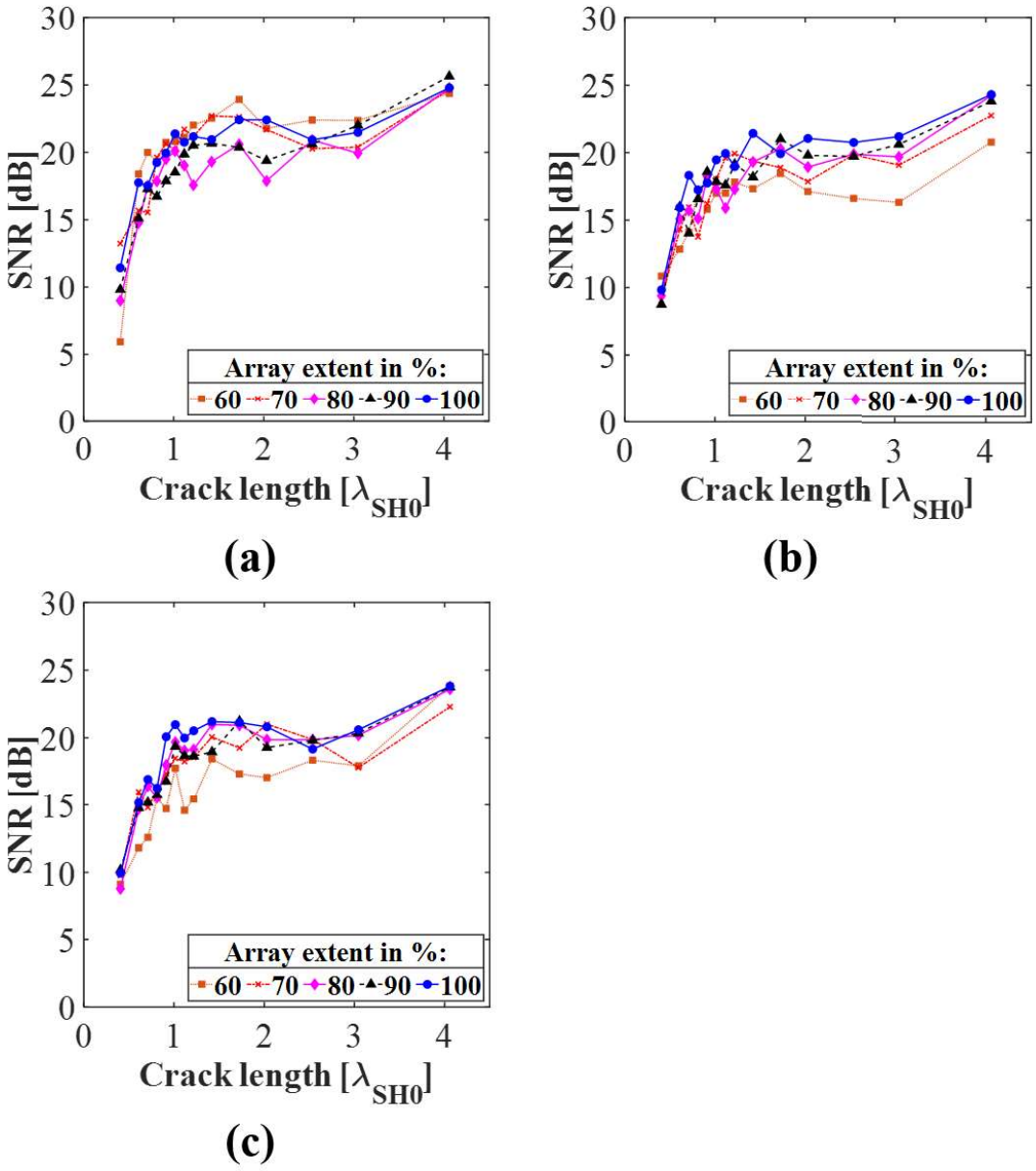

Figure 5.11: Aggregate SNR versus true crack length plots obtained from experimental FMCPWI reconstructions using 60 % to 100 % array circumferential extent and (a) 0°, (b) 90° and (c) 180° crack circumferential positions with respect to array centreline. [P2]

curves indicate a higher SNR compared to FE simulations as discussed earlier in section 4.7. This is caused by the tendency of the FE simulations to overestimate coherent noise in the closed geometries such as a pipe. The differences in SNR curves between different array circumferential extents are smaller compared to the differences observed in FE study. This agrees with the qualitative visual inspection of FMCPWI reconstructions with array extents of 60 % and above presented in Figure 5.9, where the level of incoherent noise speckles is similar for 60 % to 100 % circumferential extents. While in Figure 5.11(b,c) one could notice a slight degradation of SNR performance with the decrease in array circumferential extent, because the differences between the SNR levels are small, the slight fluctuations of the curves due to the random nature of the incoherent noise make it hard to observe this phenomenon. The main reason for the discrepancy between the FE and experimental SNR is the domination of the incoherent noise in the experiments (discussed earlier in section 4.7) and the lower significance of the coherent noise than indicated in the FE study. Nevertheless, the overall shape of the SNR curves in the experimental and FE studies is the same. For notches shorter than 1.5 λ_{SH0} the SNR steeply increases with the increase in the notch length and the SNR curves plateau when the notch length is above 1.5 λ_{SH0}. The shape of the SNR curves is primarily governed by the shape of the defect indication amplitude curves (e.g. presented for fully circumferential array in Figure 4.24). Based on the results presented in Figure 5.11, it can be concluded that the SNR achieved with array circumferential extents above 60 % is sufficient for reliable detection of notches. Because SNR is higher than 6 dB for notches longer than the resolution it is sufficient to estimate the lateral length of the notches using FWHM method.

In section 4.8 it was shown that it is possible to estimate crack depth from its indication in the reconstructed image using a fully circumferential array. When the

circumferential extent of the phased array is limited, additional complexity arises. As discussed in section 5.2, the reduced array extent results in the uneven illumination and reception throughout the pipe. Consequently, the crack indications in different positions would have slightly different amplitudes. Therefore, this would have to be accounted for when estimating the crack depth using a partial circumferential array.

5.5. Summary

This chapter investigated the impact of a limited circumferential phased array on the performance of SH0 guided wave PWI (FE simulations) and FMCPWI (experiments) in pipes. It was analytically established that limiting the circumferential extent of the array has a negative impact on the k-space data available for imaging and the phased array focusing performance, however, some of the adverse effects are mitigated by the temporal bandwidth of a typical probing Hann-windowed wavelet. The FE and experimental studies compared the key performance indicators such as lateral resolution and SNR for a range of different array circumferential extents in 0°, 90° and 180° circumferential positions with respect to the centreline of the array. The experimental results supported the validity of the FE findings. It was concluded that while a fully circumferential array provides the best performance of synthetic focusing imaging, it is not essential for reliable pipe inspection. The detection and location of cracks above a wavelength is possible with arrays above 50 % of the circumference, however, array circumferential extents of at least 60 % are required for the reliable detection and location of shorter cracks, and sizing of cracks longer than the resolution. In general, restricting the circumferential extent of the array to 60 % results in a slight decrease in SNR, however, it has a limited impact on the achievable resolution. Array circumferential extents below 50 % result in the presence of strong coherent and incoherent noise artefacts making it impossible to distinguish the crack indication from the noise and hence these circumferential extents are not suitable for pipe inspection.

6. Conclusions and future work

6.1. Thesis review

In this thesis the high resolution synthetic focusing imaging methods such as TFM and PWI were adapted to pipe GWT. Their performance was evaluated and compared against the current state-of-the-art technique in GWT, CSM. The influence of limiting array circumferential extent on the imaging capabilities was investigated to address the inspection scenarios where there is only partial circumferential access.

In chapter 2, the fundamentals of elastic wave propagation in solids were outlined with the main focus on guided waves in plates and pipes. The chapter discussed the current implementations of guided waves to NDT of pipes, and briefly outlined their capabilities and limitations.

Chapter 3 of the thesis revised the popular two dimensional synthetic focusing imaging algorithms such as CSM, TFM and PWI. The theoretical framework for the adaptation of these imaging techniques to pipe GWT was outlined, followed by a discussion on resolution achievable by guided wave phased array imaging setup using a fully circumferential transduction ring in pulse echo configuration. Subsequently, the adaptation of the considered imaging techniques to pipe GWT was presented. A spatial Fourier domain filter removing undesired coherent noise from the FMC data was proposed to improve coherent SNR of FMC based methods. Then, a novel guided wave PWI transduction setup was introduced to allow the suppression of the unwanted fundamental S0 mode and hence to improve the coherent SNR. Finally, a method transforming FMC data into ultrasonic data corresponding to PWI acquisition was presented.

In chapter 4 the methodology for resolution and SNR measurements from the

reconstructed images was introduced. This was followed by the outline of the FE model and the experimental setup. Next, a study on the selection of the optimal imaging parameters for synthetic focusing imaging methods was conducted using the FE simulations. Subsequently, the performance of CSM, TFM, PWI and FMCPWI was evaluated and compared in terms of the lateral resolution, defect sizing accuracy and SNR using FE and experimental studies. Following, the potential for crack through wall thickness depth estimation from the PWI reconstructions was presented. Then, the performance of the S0 cancelling transduction setup was evaluated based on the FE results. The chapter concluded with the discussion on generalisation of the results for different axial positions of a crack, different frequencies and pipe diameters.

Chapter 5 begins with the analytical analysis of the influence of the limited circumferential access on the reconstructions using synthetic focusing imaging. This is followed by the investigation of the practical consequences of reducing the circumferential extent of the phased array based on FE and experimental studies. The considered key performance indicators were lateral resolution, defect sizing accuracy and SNR.

6.2. Main findings

The current ultrasonic pipe GWT systems are designed to achieve high volumetric coverage from a single device position. The ability to inspect tens of metres of pipe in a single acquisition, comes at the price of limited individual defect characterisation. Hence, GWT is typically deployed as a screening method. The areas where potential defects are indicated are then inspected using more quantitative local techniques, such as bulk wave phased array ultrasonic testing, which allow for defect characterisation. It is often the case that the access to the pipe is very limited and consequently the local follow-up inspections are not possible. Examples of such inaccessible locations

include certain crucial tubular components within the UK's AGR nuclear power plants. EDF Energy was the industrial partner for this project, and the primary motivation behind it was the inspection of pipes that extend into the restricted high radiation zone of the reactor. These pipes can be partially accessed from zones with lower levels of radiation from where GWT can be deployed. In such inspection setups, individual defect characterisation has to rely on GWT, and therefore an improvement in this method is needed to address such inspection scenarios.

Phased array synthetic focusing imaging is frequently utilized in bulk wave ultrasonic testing to identify, locate, and characterize defects in material. By implementing these imaging techniques to pipe GWT, it would be possible to achieve similar results with guided waves. Therefore, in this thesis high resolution synthetic focusing imaging methods CSM, TFM, PWI and FMCPWI were adapted to inspection of pipes using guided waves. The proposed adaptation is based on the plate-pipe analogy in which analysis of guided waves in pipe is approximated by analogical analysis of guided waves in an unwrapped infinite periodic plate neglecting the curvature. The adaptation of the imaging algorithms uses the local plate guided wave solutions instead of the global pipe guided wave solutions suggested in the literature. This allowed for simplification of the imaging algorithms, avoidance of dispersion considerations and retrieval of a wider range of spatial frequencies during the reconstruction process.

To evaluate and compare the performance of the considered synthetic focusing imaging methods in a fair way, the optimal imaging parameters were investigated. It was observed that during FMC and PWI acquisitions the undesired fundamental S0 mode is excited in the circumferential direction as a by-product of the SH0 excitation. It results in artefacts in the form of periodically appearing noise bands corrupting the reconstructed images. It was established that the coherent noise due to the S0 mode can be successfully mitigated by the reduction of the transmission angles in PWI to

the range between -28° and 28° and by analogical filtering out the waves travelling at angles outside this range from the FMC data used for TFM.

It was shown that the range of angles on transmission and reception that can be effectively used for focusing during reconstruction is limited by the coherent noise and the angular reflectivity of the SH0 mode. Until a certain point the increase in the resolution thanks to wider transmission/reception angular range outweighs the negative impact on the coherent SNR. However, beyond this point the increase in the resolution is negligible and the further increase in transmission/reception angular range degrades the image quality. Through the investigation of this trade-off it was established that the optimal range of transmission angles in PWI and FMCPWI was between -28° to 28° and for TFM the optimal number of helical paths used for focusing on transmission was 3. On reception, 3 helical paths were found to be optimal for all considered imaging methods.

The performance of the reconstruction methods implemented with the optimal imaging parameters was then evaluated and compared in terms of resolution, sizing accuracy and SNR. It was shown that PWI, FMCPWI and TFM achieve practically identical resolution of 0.9 λ_{SH0} which is superior to the resolution of 1.4 λ_{SH0} achieved by CSM. The FMC based methods produce images with a substantially lower SNR compared to the methods involving plane wave acquisition, namely PWI and CSM. The lower SNR was attributed to incoherent noise. Consequently, TFM and FMCPWI were insensitive to smaller notches in experiments, indicating that these techniques should not be deployed without incoherent noise mitigation methods. While PWI and CSM achieved sufficient SNR to detect the smallest introduced notch removing 1 % of the cross sectional area of the pipe, PWI achieves better resolution with significantly higher overall SNR making it a more attractive choice for pipe GWT. Hence this technique was used in the remainder of the study. Within the resolution limit, the maximum

error in the crack length estimate from the images reconstructed using PWI was shown to be between 10 % and 15 %, with a typical error much smaller than that. The error could be minimised with the use of size correction charts.

Through the FE simulations, it was demonstrated that the amplitude of the crack indication is proportional to its depth. This finding suggests the potential for estimating the depth of a crack through wall thickness from reconstructed images, assuming the crack's length exceeds the resolution limit. Some discrepancies between the FE results and the experiments were observed and were attributed to the fact that while FE study investigated zero-volume cracks, the experimental notches had axial extent, resulting in reflections from their front and back faces, as observed in the literature. However, further investigation is needed to definitively determine the cause of these discrepancies.

During the transmission of the SH0 guided wave mode with shear contact transducers inevitably the unwanted S0 mode is excited which can result in artefacts and decreased SNR in the reconstructed images. A novel PWI transduction setup was proposed to supress the transmission of the S0 mode during PWI acquisition. In the FE study it was shown that the transduction setup achieves practically a complete suppression of the undesired mode. The false cut-end echo artefact due to the S0 mode was reduced by at least 20 dB to levels indistinguishable from the background noise.

It is often the case that access to the full pipe circumference is limited in hard-to-reach inspection scenarios. Therefore, this thesis investigated a deployment of guided wave synthetic focusing imaging in pipes where there is access to only part of the circumference. It was analytically demonstrated that limiting the circumferential extent of the array has a negative impact on the range of spatial frequencies available for imaging and the phased array focusing performance, however, some of the adverse effects are mitigated by the temporal bandwidth of a typical probing Hann-windowed

tone burst. Additionally, the study revealed that a restricted circumferential span of the array results in a varying range of spatial frequencies available for imaging around the pipe circumference. This stands in contrast to the constant range of spatial frequencies around the circumference when utilizing a fully circumferential array. From the FE and experimental studies it was concluded that while a fully circumferential array provides the best performance of the synthetic focusing imaging, it is not essential for reliable pipe inspection. The detection and location of cracks longer than a wavelength is possible with arrays above 50 % of the circumference, however, array circumferential extents of at least 60 % are required for the reliable detection and location of shorter cracks, and lateral size estimation of cracks longer than the resolution. In general, restricting the circumferential extent of the array to 60 % results in a slight decrease in SNR, however, it has a limited impact on achievable resolution, which was shown to decrease from 0.9 λ_{SH0} to 1 λ_{SH0}. Limiting the array extent resulted in the increase of the maximum error in crack length estimate from the reconstructed images to 20 %, however the typical error was much smaller than that and it can be reduced with the use of size correction charts. Array circumferential extents below 50 % result in the presence of strong coherent and incoherent noise artefacts making it impossible to distinguish the defect indication from the noise and hence these circumferential extents are not suitable for pipe inspection.

During the EngD project a prototype pipe inspection tool for high resolution synthetic focusing imaging using guided waves was created by the adaptation of the design of the commercially available Guided Ultrasonics Ltd. [1] transduction ring. The developed prototype tool allowed for individual control over each transducer and had narrower circumferential spacing between the elements compared to the commercial transduction ring. The narrower spacing was required to provide sufficient spatial sampling, allowing the use of higher excitation frequencies for imaging applications in

order to achieve better resolution. Individually addressed elements were a substantial departure from the 8 channel per transducer row approach used in the industry so far. The successful implementation of the prototype inspection tool in the experiments and a good agreement between the FE and experimental results served as a proof of concept that the high resolution synthetic focusing imaging can be effectively deployed to pipe GWT.

6.3. Suggestions for future work

The study presented in this thesis was concerned with part-circumferential part-depth planar cracks with face perpendicular to the axial direction of the pipe because this was a particular focus of interest for the industrial partner of the EngD programme. However, in other industries, e.g. oil and gas, corrosion is the main concern, so it would be useful to investigate the performance of synthetic focusing imaging techniques for corrosion morphologies.

The project proposed the S0 mode cancelling PWI transduction setup, to eliminate the artefacts caused by the presence of the unwanted mode. The reduction of the transmitted S0 mode to levels indistinguishable from the background noise was shown in the FE simulations. The concept was not studied experimentally due to limitations of the available hardware, hence an experimental validation is yet to be completed.

In section 4.8, it was demonstrated that crack depth can be estimated from the crack indication amplitude in the reconstructed image. It was shown that the crack indication amplitude varies with the axial extent of the part-depth crack. Because the notch used in the experiments had an axial width of 3 mm, the recorded amplitude was higher compared to the one observed for the zero volume crack in the FE simulations. The typical part-depth cracks in pipes have a very narrow width and hence they can be considered as zero volume cracks. Therefore, it would be beneficial

to conduct experiments with zero volume cracks or very narrow notches to show whether the FE predictions of crack indication amplitude as a function of crack depth and length are accurate enough to be used for crack depth estimation. It would also be useful to develop an analytical expression for crack indication amplitude in PWI reconstructions with a wide range of probing wave angles.

In this thesis synthetic focusing imaging methods were deployed in a relatively short pipe. The next step would be to investigate the performance of these methods in longer pipes. In long range applications, to maintain quasi constant resolution throughout the pipe, the number of helical paths used for focusing would have to progressively increase with distance. Moreover, in longer pipes, the phase velocity error due to plate/pipe approximation could become noticeable and lead to blurring of reconstructed features far away from the array. Hence, it would be beneficial to correct for phase velocity variations with angle of propagation. Additionally, longer pipes typically contain welds, hence the effect of welds on imaging results would need to be studied.

In the experiments, a partial circumferential array was simulated by using only part of the transduction ring for transmitting and receiving the ultrasonic waves. To implement guided wave synthetic focusing imaging to practical inspection of pipes with limited circumferential access, a new transduction device needs to be developed. In the project presented in this thesis a fully circumferential ring of piezoelectric shear contact transducers was used. The rigid ring chassis clamped onto the pipe provided an even coupling of the transducers via a spring loaded assembly at each element, ensuring an even force pushing each transducer against the surface. Such an attachment method would not be feasible with access to only part of the circumference. An attractive idea worth exploring would be to use a partial circumferential phased array consisting of guided wave electromagnetic acoustic transducers (EMATs) instead of piezoelectric transducers. EMATs do not require direct coupling to the specimen surface and

because they consist of magnets, they can be readily attached to the ferromagnetic pipes. The idea of an EMAT phased array was explored for example in [207], and the use of an array of EMATs for guided wave structural health monitoring was investigated in [134,135,138,139]. PWI would be a preferred method for deployment with EMAT phased arrays because it provides high acoustic energy during each acquisition thanks to excitation of waves with all the array elements. This would partially compensate for a much lower amplitude of ultrasonic waves excited with EMATs compared to piezoelectric transducers. If connections between the EMAT phased array elements would be flexible (i.e. the array could conform to different curvature profiles), the same array could be deployed for inspection of different pipe sizes. This would create an opportunity for inspection of other ferromagnetic plate like structures with small curvature (i.e. where effects of the curvature can be neglected) such as tanks, boilers and pressure vessels.

This page intentionally left blank

References

1. Guided Ultrasonics. Available online: http://www.guided-ultrasonics.com/ (accessed on 18 August 2022).

2. ResearchAndMarkets. *Global Oil and Gas Pipelines Market Outlook to 2025 - Capacity and Capital Expenditure Outlook with Details of All Operating and Planned Pipelines*; ResearchAndMarkets: 2022.

3. ResearchAndMarkets. *Pipeline Construction Market By Pipe Type, By Application, By End User: Global Opportunity Analysis and Industry Forecast, 2021-2031*; 2022.

4. Dodds, P.E.; McDowall, W. The future of the UK gas network. *Energy Policy* **2013**, *60*, 305-316, doi:10.1016/j.enpol.2013.05.030.

5. Sider, A.; Friedman, N. More Than Half of U.S. Pipelines Are at Least 46 Years Old. *The Wall Street journal. Eastern edition* **2016**.

6. Cosham, A.; Hopkins, P. The effect of dents in pipelines - guidance in the pipeline defect assessment manual. *International Journal of Pressure Vessels and Piping* **2004**, *81*, 127-139, doi:10.1016/j.ijpvp.2003.11.004.

7. Hanif, W.; Kenny, S. Mechanical Damage and Fatigue Assessment of Dented Pipelines Using Fea. *Proceedings of the 10th International Pipeline Conference - 2014, Vol 2* **2014**.

8. Okodi, A.; Li, Y.; Cheng, R.; Kainat, M.; Yoosef-Ghodsi, N.; Adeeb, S. Crack Propagation and Burst Pressure of Pipeline with Restrained and Unrestrained Concentric Dent-Crack Defects Using Extended Finite Element Method. *Applied Sciences-Basel* **2020**, *10*, doi:10.3390/app10217554.

9. Alexander, C.; Brownlee, K. Methodology for Assessing the Effects of Plain Dents, Wrinkle Bends, and Mechanical Damage on Pipeline Integrity. In Proceedings of the NACE International 2007 Corrosion Conference & Exposition, Nashville, Tennessee, 2007.

10. Sieradzki, K.; Newman, R.C. Stress-corrosion cracking. *Journal of Physics and Chemistry of Solids* **1987**, *48*, 1101-1113, doi:10.1016/0022-3697(87)90120-x.

11. Raja, V.S.; Shoji, T. *Stress corrosion cracking: theory and practice*; Woodhead Publishing Ltd.: Oxford, UK, 2011.

12. Andresen, P.L.; Was, G.S. 4.07 - Irradiation Assisted Stress Corrosion Cracking. In *Comprehensive Nuclear Materials*, 2 ed.; Konings, R., Stoller, R.E., Eds.; Elsevier: San Diego, 2019; Volume 4, pp. 190-217.

13. Evans, T.C. Hydrogen Attack on Carbon Steels. *Mechanical Engineering* **1948**, *70*, 414-416.

14. Yokogawa, K.; Fukuyama, S.; Kudo, K.; Shewmon, P.G. Effect of hydrogen attack on tensile and creep properties of low carbon steel. *International Journal of Pressure Vessels and Piping* **1989**, *37*, 365-385, doi:10.1016/0308-0161(89)90030-6.

15. Nelson, G.A. Hydrogenation Plant Steels. In Proceedings of the American Petroleum Institute, Washington, DC, 1949; pp. 163-174.

16. Ma, Q.; Tian, G.; Zeng, Y.; Li, R.; Song, H.; Wang, Z.; Gao, B.; Zeng, K. Pipeline In-Line Inspection Method, Instrumentation and Data Management. *Sensors (Basel)* **2021**, *21*, doi:10.3390/s21113862.

17. Ho, M.; El-Borgi, S.; Patil, D.; Song, G. Inspection and monitoring systems subsea pipelines: A review paper. *Structural Health Monitoring* **2019**, *19*, 606-645, doi:10.1177/1475921719837718.

18. Carvalho, A.A.; Rebello, J.M.A.; Souza, M.P.V.; Sagrilo, L.V.S.; Soares, S.D. Reliability of non-destructive test techniques in the inspection of pipelines used in the oil industry. *International Journal of Pressure Vessels and Piping* **2008**, *85*, 745-751, doi:10.1016/j.ijpvp.2008.05.001.

19. Nonbel, E. *Description of the Advanced Gas Cooled Type of Reactor (AGR)*; 87-550-2264-2; Nordisk Kernesikkerhedsforskning: Rosktldc, Denmark, 1996.

20. Alleyne, D.N.; Pavlakovic, B.; Lowe, M.; Cawley, P. The Use of Guided Waves for Rapid Screening of Chemical Plant Pipework. *Journal of the Korean Society for Nondestructive Testing* **2002**, *22*, 589-598.

21. Alleyne, D.N.; Pavlakovic, B.; Lowe, M.J.S.; Cawley, P. Rapid long-range inspection of chemical plant pipework using guided wave. *Insight* **2001**, *43*, 93.

22. Demma, A.; Cawley, P.; Lowe, M.J.S.; Roosenbrand, A.G. The reflection of the fundamental torsional mode from cracks and notches in pipes. *Journal of the Acoustical Society of America* **2003**, *114*, 611-625, doi:10.1121/1.1582439.

23. Alleyne, D.N.; Lowe, M.J.; Cawley, P. The Reflection of Guided Waves from Circumferential Notches in Pipes. *Journal of Applied Mechanics* **1998**, *65*, 635-641, doi:10.1115/1.2789105.

24. Demma, A.; Cawley, P.; Lowe, M.J.S.; Roosenbrand, A.G.; Pavlakovic, B. The reflection of guided waves from notches in pipes: a guide for interpreting corrosion measurements. *NDT & E International* **2004**, *37*, 167-180, doi:10.1016/j.ndteint.2003.09.004.

25. Davies, J.; Cawley, P. The Application of Synthetic Focusing for Imaging Crack-Like Defects in Pipelines Using Guided Waves *Transactions on Ultrasonics, Ferroelectrics, and Frequency Control* **2009**, *56*, 759-771.

26. Chiao, R.Y.; Thomas, L.J. Analytic Evaluation of Sampled Aperture Ultrasonic Imaging Techniques for NDE. *IEEE Transactions on Ultrasonics, Ferroelectrics, and Frequency Control* **1994**, *41*, 484-493, doi:10.1109/58.294109.

27. Papaelias, M.P.; Roberts, C.; Davis, C.L. A review on non-destructive evaluation of rails: state-of-the-art and future development. *Proceedings of the Institution of Mechanical Engineers, Part F: Journal of Rail and Rapid Transit* **2008**, *222*, 367-384, doi:10.1243/09544097jrrt209.

28. Reverdy, F.; Benoist, G.; Le Ber, L. Advantages and Complementarity of Phased-Array Technology and Total Focusing Method. In Proceedings of the 19th World Conference on Non-Destructive Testing, Munich, Germany, 2016.

29. Wilcox, P.D. Ultrasonic Arrays in NDE: Beyond the B-scan. *The 39th Annual Review of Progress in Quantitative Nondestructive Evaluation AIP Conf. Proc* **2013**, *1511*, 33-50, doi:10.1063/1.4789029.

30. Wilcox, P.D.; Holmes, C.; Drinkwater, B.W. Enhanced Defect Detection and Characterisation by Signal Processing of Ultrasonic Array Data. In Proceedings of the 9th European Conference on NDT, Berlin, Germany, 2006.

31. Marmonier, M.; Robert, S.; Laurent, J.; Prada, C. Real-time 3D imaging with Fourier-domain algorithms and matrix arrays applied to non-destructive testing. *Ultrasonics* **2022**, *124*, doi:ARTN 106708 10.1016/j.ultras.2022.106708.

32. Sutcliffe, M.; Weston, M.; Dutton, B.; Charlton, P.; Donne, K. Real-time full matrix capture for ultrasonic non-destructive testing with acceleration of post-processing through graphic hardware. *Ndt & E International* **2012**, *51*, 16-23, doi:10.1016/j.ndteint.2012.06.005.

33. Wang, C.; Mao, J.; Leng, T.; Zhuang, Z.Y.; Wang, X.M. Efficient Acceleration for Total Focusing Method Based on Advanced Parallel Computing in FPGA. *International Journal of Acoustics and Vibrations* **2017**, *22*, 536-540, doi:10.20855/ijav.2017.22.4500.

34. Zhang, J.; Drinkwater, B.W.; Wilcox, P.D. The Use of Ultrasonic Arrays to Characterize Crack-Like Defects. *Journal of Nondestructive Evaluation* **2010**, *29*, 222-232, doi:10.1007/s10921-010-0080-6.

35. Elliott, J.B.; Lowe, M.J.S.; Huthwaite, P.; Phillips, R.; Duxbury, D.J. Sizing Subwavelength Defects With Ultrasonic Imagery: An Assessment of Super-Resolution Imaging on Simulated Rough Defects. *IEEE Transactions on Ultrasonics, Ferroelectrics, and Frequency Control* **2019**, *66*, 1634-1648, doi:10.1109/TUFFC.2019.2925974.

36. Karaman, M.; Li, P.C.; Odonnell, M. Synthetic-Aperture Imaging for Small-Scale Systems. *IEEE Transactions on Ultrasonics, Ferroelectrics, and Frequency Control* **1995**, *42*, 429-442, doi:10.1109/58.384453.

37. Ylitalo, J.T.; Ermert, H. Ultrasound Synthetic-Aperture Imaging - Monostatic Approach. *IEEE Transactions on Ultrasonics, Ferroelectrics, and Frequency Control* **1994**, *41*, 333-339, doi:10.1109/58.285467.

38. Holmes, C.; Drinkwater, B.W.; Wilcox, P.D. Post-Processing of the Full Matrix of Ultrasonic Transmit–Receive Array Data for Non-Destructive Evaluation. *NDT & E International* **2005**, *38*, 701-711, doi:10.1016/j.ndteint.2005.04.002.

39. Oralkan, O.; Ergun, A.S.; Johnson, J.A.; Karaman, M.; Demirci, U.; Kaviani, K.; Lee, T.H.; Khuri-Yakub, B.T. Capacitive micromachined ultrasonic transducers: next-generation arrays for acoustic imaging? *IEEE Transactions on Ultrasonics, Ferroelectrics, and Frequency Control* **2002**, *49*, 1596-1610, doi:10.1109/tuffc.2002.1049742.

40. Cheng, J.; Lu, J.-y. Extended High-Frame Rate Imaging Method with Limited-Diffraction Beams. *IEEE Transactions on Ultrasonics, Ferroelectrics, and Frequency Control* **2006**, *53*, 880-899, doi:10.1109/tuffc.2006.1632680.

41. Le Jeune, L.; Robert, S.; Lopez Villaverde, E.; Prada, C. Plane Wave Imaging for Ultrasonic Non-destructive Testing: Generalization to Multimodal Imaging. *Ultrasonics* **2016**, *64*, 128-138, doi:10.1016/j.ultras.2015.08.008.

42. Montaldo, G.; Tanter, M.; Bercoff, J.; Benech, N.; Fink, M. Coherent Plane-Wave Compounding for Very High Frame Rate Ultrasonography and Transient Elastography. *IEEE Transactions on Ultrasonics, Ferroelectrics, and Frequency Control* **2009**, *56*, 489-506, doi:10.1109/Tuffc.2009.1067.

43. Zhuang, Z.; Zhang, J.; Lian, G.; Drinkwater, B.W. Comparison of Time Domain and Frequency-Wavenumber Domain Ultrasonic Array Imaging Algorithms for Non-Destructive Evaluation. *Sensors* **2020**, *20*, 4951, doi:10.3390/s20174951.

44. Sui, H.; Xu, P.; Huang, J.; Zhu, H. Space Optimized Plane Wave Imaging for Fast Ultrasonic Inspection with Small Active Aperture: Simulation and Experiment. *Sensors* **2020**, *21*, doi:10.3390/s21010055.

45. Cosarinsky, G.; Fernandez-Cruza, J.; Camacho, J. Plane Wave Imaging through Interfaces. *Sensors (Basel)* **2021**, *21*, doi:10.3390/s21154967.

46. Sandrin, L.; Catheline, S.; Tanter, M.; Hennequin, X.; Fink, M. Time-resolved pulsed elastography with ultrafast ultrasonic imaging. *Ultrason Imaging* **1999**, *21*, 259-272, doi:10.1177/016173469902100402.

47. Sandrin, L.; Tanter, M.; Catheline, S.; Fink, M. Shear modulus imaging with 2-D transient elastography. *IEEE Transactions on Ultrasonics, Ferroelectrics, and Frequency Control* **2002**, *49*, 426-435, doi:10.1109/58.996560.

48. Song, T.K.; Chang, J.H. Synthetic aperture focusing method for ultrasound imaging based on planar waves. 2004.

49. Velichko, A.; Croxford, J. Strategies for Data Acquisition Using Ultrasonic Phased Arrays. *Proceedings of the Royal Society* **2018**, *474*, doi:10.1098/rspa.2018.0451.

50. Sicard, R.; Goyette, J.; Zellouf, D. A SAFT algorithm for lamb wave imaging of isotropic plate-like structures. *Ultrasonics* **2002**, *39*, 487-494, doi:10.1016/S0041-624X(01)00087-7.

51. Wilcox, P.D. Omni-directional guided wave transducer arrays for the rapid inspection of large areas of plate structures. *IEEE Transactions on Ultrasonics, Ferroelectrics, and Frequency Control* **2003**, *50*, 699-709, doi:10.1109/Tuffc.2003.1209557.

52. Sicard, R.; Chahbaz, A.; Goyette, J. Guided lamb waves and L-SAFT processing technique for enhanced detection and imaging of corrosion defects in plates with small depth-to-wavelength ratio. *IEEE Transactions on Ultrasonics, Ferroelectrics, and Frequency Control* **2004**, *51*, 1287-1297, doi:10.1109/tuffc.2004.1350957.

53. Davies, J.; Simonetti, F.; Lowe, M.J.S.; Cawley, P. Review of Synthetically Focused Guided Wave Imaging Techniques With Application to Defect Sizing. In Proceedings of the 25th Annual Review of Progress in Quantitative Nondestructive Evaluation, Brunswick, ME, USA, 2006; pp. 142-149.

54. Dalitz, C.; Pohle-Frohlich, R.; Michalk, T. Point spread functions and deconvolution of ultrasonic images. *IEEE Transactions on Ultrasonics, Ferroelectrics, and Frequency Control* **2015**, *62*, 531-544, doi:10.1109/TUFFC.2014.006717.

55. Ozaki, Y.; Sumitani, H.; Tomoda, T.; Tanaka, M. A new system for real-time synthetic aperture ultrasonic imaging. *IEEE Transactions on Ultrasonics, Ferroelectrics, and Frequency Control* **1988**, *35*, 828-838, doi:10.1109/58.9340.

56. Sparrow, C.M. On Spectroscopic Resolving Power. *The Astrophysical Journal* **1916**, *44*, doi:10.1086/142271.

57. Nanekar, P.; Kumar, A.; Jayakumar, T. SAFT-assisted sound beam focusing using phased arrays (PA-SAFT) for non-destructive evaluation. *Nondestructive Testing Evaluation* **2015**, *30*, 105-123, doi:10.1080/10589759.2014.1002837.

58. Davies, J. Inspection of Pipes Using Low Frequency Focused Guided Waves, PhD Thesis. Imperial College London, London, 2008.

59. Hayashi, T.; Murase, M. Defect imaging with guided waves in a pipe. *The Journal of the Acoustical Society of America* **2005**, *117*, 2134-2140, doi:10.1121/1.1862572.

60. Davies, J.; Cawley, P. The Application of Synthetically Focused Imaging Techniques for High Resolution Guided Wave Pipe Inspection. In Proceedings of the AIP Conference, 2007; pp. 681-688.

61. Davies, J.; Cawley, P.; Michael, L. Long Range Guided Wave Pipe Inspection – the Advantages of Focusing. In Proceedings of the 17th World Conference on Nondestructive Testing, Shanghai, China, 2008; pp. 1-6.

62. Graff, K.F. *Wave Motion in Elastic Solids*; Dover Publications: New York, 1975.

63. Royer, D.; Valier-Brasier, T. *Elastic Waves in Solids 1*; ISTE: London, 2022.

64. Achenbach, J.D. *Wave Propagation in Elastic Solids*; Elsevier: Amsterdam, 1973.

65. Rose, J.L. *Ultrasonic Guided Waves in Solid Media*; Cambridge University Press: 2014.

66. Auld, B.A. *Acoustic Fields and Waves in Solids* John Wiley & Sons: New York, 1973; Volume 2.

67. Ostachowicz, W.; Kudela, P.; Krawczuk, M.; Zak, A. *Guided Waves in Structures for SHM : The Time - domain Spectral Element Method*; Wiley: 2012.

68. Navier, C.L. *Annales de chimie et de physique*; Crochard: Paris, 1821; Volume 19.

69. Kolsky, H. *Stress Waves in Solids*, 1 ed.; Dover Publications: New York, 1963.

70. Helmholtz, H. Über Integrale der hydrodynamischen Gleichungen, welcher der Wirbelbewegungen entsprechen. *Journal für die reine und angewandte Mathematik* **1858**, *55*, 25–55.

71. Malvern, L.E. *Introduction to the mechanics of a continuous medium*; Prentice-Hall: New Jersey, 1969.

72. Miklowitz, J. *The Theory of Elastic Waves and Waveguides*, 1 ed.; North Holland: Oxford, 1978.

73. Ostachowicz, W.; Güemes, A. *New Trends in Structural Health Monitoring*; Springer: Vienna, 2013; Volume 542.

74. Nazarchuk, Z.; Skalskyi, V.; Serhiyenko, O. *Acoustic Emission: Methodology and Application*; Springer: New York, 2017.

75. Viktorov, I.A. *Rayleigh and Lamb Waves: Physical Theory and Applications*; Springer: New York, NY, 1967.

76. Li, J.; Rose, J.L. Natural Beam Focusing of Non-axisymmetric Guided Waves in Large-diameter Pipes. *Ultrasonics* **2006**, *44*, 35-45, doi:10.1016/j.ultras.2005.07.002.

77. Velichko, A.; Wilcox, P.D. Excitation and Scattering of Guided Waves: Relationships Between Solutions for Plates and Pipes. *The Journal of the Acoustical Society of America* **2009**, *125*, 3623-3631, doi:10.1121/1.3117441.

78. Lamb, H. On waves in an elastic plate. *Proceedings of the Royal Society of London. Series A* **1917**, *93*, 114-128, doi:10.1098/rspa.1917.0008.

79. Harker, A.H. *Elastic Waves in Solids, With Applications to Nondestructive Testing of Pipelines*; A. Hilger in association with British Gas: Bristol, 1988.

80. Pavlakovic, B.; Lowe, M.; Alleyne, D.; Cawley, P. Disperse: A General Purpose Program for Creating Dispersion Curves. In *Review of Progress in Quantitative Nondestructive Evaluation*, Thompson, D.O., Chimenti, D.E., Eds.; Springer: New York, NY, 1997; Volume 16, pp. 185-192.

81. Zimmermann, A.A.E.; Huthwaite, P.; Pavlakovic, B. High-resolution thickness maps of corrosion using SH1 guided wave tomography. *Proceedings of The*

Royal Society A: Mathematical Physical and Engineering Sciences **2021**, *477*, 20200380, doi:10.1098/rspa.2020.0380.

82. Malyarenko, E.V.; Hinders, M.K. Ultrasonic Lamb wave diffraction tomography. *Ultrasonics* **2001**, *39*, 269-281, doi:10.1016/s0041-624x(01)00055-5.

83. Belanger, P.; Cawley, P.; Simonetti, F. Guided wave diffraction tomography within the born approximation. *IEEE Transactions on Ultrasonics, Ferroelectrics, and Frequency Control* **2010**, *57*, 1405-1418, doi:10.1109/TUFFC.2010.1559.

84. Alleyne, D.N.; Vogt, T.; Cawley, P. The choice of torsional or longitudinal excitation in guided wave pipe inspection. In Proceedings of the 5th Iranian International NDT Conference, Tehran, 2018.

85. Cawley, P.; Alleyne, D.N. The use of Lamb waves for the long range inspection of large structures. *Ultrasonics* **1996**, *34*, 287-290, doi:10.1016/0041-624x(96)00024-8.

86. Wilcox, P.D. A rapid signal processing technique to remove the effect of dispersion from guided wave signals. *IEEE Transactions on Ultrasonics, Ferroelectrics, and Frequency Control* **2003**, *50*, 419-427, doi:10.1109/tuffc.2003.1197965.

87. Sicard, R.; Goyette, J.; Zellouf, D. A numerical dispersion compensation technique for time recompression of Lamb wave signals. *Ultrasonics* **2002**, *40*, 727-732, doi:10.1016/s0041-624x(02)00201-9.

88. Rayleigh, J.W.S. *The Theory of Sound*; Dover Publications: New York, NY, 1945; Volume 1.

89. Stokes, G.G. Smith's Prize examination question no. 11. *reprinted in Mathematics and Physics Papers (1905)* **1876**, *5*, 362.

90. Tolstoy, I. *Wave Propagation*; McGraw-Hill: New York, NY, 1973.

91. Qu, J.; Berthelot, Y.; Li, Z. Dispersion of Guided Circumferential Waves in a Circular Annulus. In Proceedings of the Review of Progress in Quantitative Nondestructive Evaluation, Boston, MA, 1996.

92. Liu, G.; Qu, J. Guided Circumferential Waves in a Circular Annulus. *Journal of Applied Mechanics* **1998**, *65*, 424-430, doi:10.1115/1.2789071.

93. Zhao, X.; Rose, J.L. Guided circumferential shear horizontal waves in an isotropic hollow cylinder. *The Journal of the Acoustical Society of America* **2004**, *115*, 1912-1916, doi:10.1121/1.1691037.

94. Pochhammer, L. Ueber die Fortpflanzungsgeschwindigkeiten kleiner Schwingungen in einem unbegrenzten isotropen Kreiscylinder. *Journal für die Reine und Angewandte Mathematik* **1876**, *1876*, 324-336, doi:10.1515/crll.1876.81.324.

95. Chree, C. Longitudinal Vibrations of a Circular Bar. *Quarterly Journal of Pure and Applied Mathematics* **1886**, *21*, 287-298.

96. Chree, C. The Equations of an Isotropic Elastic Solid in Polar and Cylindrical Coordinates, Their Solutions and Applications. *Transactions of the Cambridge Philosophical Society* **1889**, *14*, 250-369.

97. Ghosh, J. Longitudinal vibrations of a hollow cylinder. *Bulletin of the Calcutta Mathematical Society* **1923**, *14*, 31-40.

98. Gazis, D.C. Exact Analysis of the Plane-Strain Vibrations of Thick-Walled Hollow Cylinders. *The Journal of the Acoustical Society of America* **1958**, *30*, 786-794, doi:10.1121/1.1909761.

99. Gazis, D.C. Three-Dimensional Investigation of the Propagation of Waves in Hollow Circular Cylinders. I. Analytical Foundation. *The Journal of the Acoustical Society of America* **1959**, *31*, 568-573, doi:10.1121/1.1907753.

100. Morse, P.M.; Feshbach, H. *Methods of Theoretical Physics*; McGraw-Hill: New York, 1953.

101. Pavlakovic, B. Leaky Guided Ultrasonic Waves in NDT. University of London, London, 1998.

102. Gazis, D.C. Three-Dimensional Investigation of the Propagation of Waves in Hollow Circular Cylinders. II. Numerical Results. *The Journal of the Acoustical Society of America* **1959**, *31*, 573-578, doi:10.1121/1.1907754.

103. Silk, M.G.; Bainton, K.F. The propagation in metal tubing of ultrasonic wave modes equivalent to Lamb waves. *Ultrasonics* **1979**, *17*, 11-19, doi:10.1016/0041-624x(79)90006-4.

104. Nishino, H.; Takashina, S.; Uchida, F.; Takemoto, M.; Ono, K. Modal Analysis of Hollow Cylindrical Guided Waves and Applications. *Japanese Journal of Applied Physics* **2001**, *40*, 364-370, doi:10.1143/jjap.40.364.

105. Pierce, A.D.; Kil, H.-G. Elastic Wave Propagation from Point Excitations on Thin-Walled Cylindrical Shells. *Journal of Vibration and Acoustics* **1990**, *112*, 399-406, doi:10.1115/1.2930524.

106. Diligent, O.; Grahn, T.; Bostrom, A.; Cawley, P.; Lowe, M.J. The low-frequency reflection and scattering of the S0 Lamb mode from a circular through-thickness

hole in a plate: Finite Element, analytical and experimental studies. *The Journal of the Acoustical Society of America* **2002**, *112*, 2589-2601, doi:10.1121/1.1512292.

107. Demma, A.; Cawley, P.; Lowe, M. Scattering of the fundamental shear horizontal mode from steps and notches in plates. *The Journal of the Acoustical Society of America* **2003**, *113*, 1880-1891, doi:10.1121/1.1554694.

108. Le Clezio, E.; Castaings, M.; Hosten, B. The interaction of the S0 Lamb mode with vertical cracks in an aluminium plate. *Ultrasonics* **2002**, *40*, 187-192, doi:10.1016/s0041-624x(02)00135-x.

109. Norris, A.N.; Vemula, C. Scattering of flexural waves on thin plates. *Journal of Sound and Vibration* **1995**, *181*, 115-125, doi:10.1006/jsvi.1995.0129.

110. McKeon, J.C.P.; Hinders, M.K. Lamb Wave Scattering from a through Hole. *Journal of Sound and Vibration* **1999**, *224*, 843-862, doi:10.1006/jsvi.1999.2164.

111. Fromme, P.; Sayir, M.B. Measurement of the scattering of a Lamb wave by a through hole in a plate. *The Journal of the Acoustical Society of America* **2002**, *111*, 1165-1170, doi:10.1121/1.1448338.

112. Cegla, F.B.; Rohde, A.; Veidt, M. Analytical prediction and experimental measurement for mode conversion and scattering of plate waves at non-symmetric circular blind holes in isotropic plates. *Wave Motion* **2008**, *45*, 162-177, doi:10.1016/j.wavemoti.2007.05.005.

113. Rajagopal, P.; Lowe, M.J. Short range scattering of the fundamental shear horizontal guided wave mode normally incident at a through-thickness crack in an isotropic plate. *The Journal of the Acoustical Society of America* **2007**, *122*, 1527, doi:10.1121/1.2764472.

114. Rajagopal, P.; Lowe, M.J. Scattering of the fundamental shear horizontal guided wave by a part-thickness crack in an isotropic plate. *The Journal of the Acoustical Society of America* **2008**, *124*, 2895-2904, doi:10.1121/1.2982410.

115. Rajagopal, P.; Lowe, M.J. Angular influence on the scattering of fundamental shear horizontal guided waves by a through-thickness crack in an isotropic plate. *The Journal of the Acoustical Society of America* **2008**, *124*, 2021-2030, doi:10.1121/1.2968697.

116. Böttger, W.; Schneider, H.; Weingarten, W. Prototype EMAT system for tube inspection with guided ultrasonic waves. *Nuclear Engineering and Design* **1987**, *102*, 369-376, doi:10.1016/0029-5493(87)90183-x.

117. Rose, J.L.; Ditri, J.J.; Pilarski, A.; Rajana, K.; Carr, F. A guided wave inspection technique for nuclear steam generator tubing. *NDT & E International* **1994**, *27*, 307-310, doi:10.1016/0963-8695(94)90211-9.

118. Mohr, W.; Holler, P. On Inspection of Thin-Walled Tubes for Transverse and Longitudinal Flaws by Guided Ultrasonic Waves. *IEEE Transactions on Sonics and Ultrasonics* **1976**, *23*, 369-373, doi:10.1109/t-su.1976.30893.

119. Alleyne, D.N.; Cawley, P. The Excitation of Lamb Waves in Pipes Using Dry-Coupled Piezoelectric Transducers. *Journal of Nondestructive Evaluation* **1996**, *15*, 11-20, doi:10.1007/BF00733822.

120. Lowe, M.J.S.; Alleyne, D.N.; Cawley, P. Defect detection in pipes using guided waves. *Ultrasonics* **1998**, *36*, 147-154, doi:10.1016/S0041-624x(97)00038-3.

121. Alleyne, D.N.; Cawley, P. Long range propagation of Lamb waves in chemical plant pipework. *Materials Evaluation* **1997**, *55*, 504-508.

122. Alleyne, D.N.; Cawley, P. The Effect of Discontinuities on the Long-range Propagation of Lamb Waves in Pipes. *Journal of Process Mechanical Engineering, Proceedings of the Institution of Mechanical Engineers, Part E* **1996**, *210*, 217-226, doi:10.1243/pime_proc_1996_210_316_02.

123. Mudge, P.J. Field application of the Teletest long range ultrasonic testing technique. *Insight* **2001**, *43*, 74-77.

124. Leinov, E.; Lowe, M.J.S.; Cawley, P. Investigation of guided wave propagation and attenuation in pipe buried in sand. *Journal of Sound and Vibration* **2015**, *347*, 96-114, doi:10.1016/j.jsv.2015.02.036.

125. Leinov, E.; Lowe, M.J.; Cawley, P. Investigation of guided wave propagation in pipes fully and partially embedded in concrete. *The Journal of the Acoustical Society of America* **2016**, *140*, 4528-4539, doi:10.1121/1.4972118.

126. Lowe, M.J.S.; Alleyne, D.N.; Cawley, P. The Mode Conversion of a Guided Wave by a Part-Circumferential Notch in a Pipe. *Journal of Applied Mechanics* **1998**, *65*, 649-656, doi:10.1115/1.2789107.

127. Cawley, P. Practical Long Range Guided Wave Inspection — Managing Complexity. *AIP Conference Proceedings* **2003**, *657*, doi:10.1063/1.157011.

128. Cawley, P.; Alleyne, D.N.; Chan, C.W. Inspection of pipes. 1994.

129. Aristégui, C.; Lowe, M.J.S.; Cawley, P. Guided waves in fluid-filled pipes surrounded by different fluids. *Ultrasonics* **2001**, *39*, 367-375, doi:10.1016/s0041-624x(01)00064-6.

130. Plona, T.J.; Sinha, B.K.; Kostek, S.; Chang, S.K. Axisymmetric wave propagation in fluid-loaded cylindrical shells. II: Theory versus experiment. *The*

Journal of the Acoustical Society of America **1992**, *92*, 1144-1155, doi:10.1121/1.404041.

131. Mu, J.; Rose, J.L. Guided wave propagation and mode differentiation in hollow cylinders with viscoelastic coatings. *The Journal of the Acoustical Society of Americ* **2008**, *124*, 866-874, doi:10.1121/1.2940586.

132. Lowe, M.J.; Cawley, P.; Galvagni, A. Monitoring of corrosion in pipelines using guided waves and permanently installed transducers. *The Journal of the Acoustical Society of America* **2012**, *132*, 1932, doi:10.1121/1.4755100.

133. Cawley, P.; Cegla, F.B.; Galvagni, A. Guided waves for NDT and permanently-installed monitoring. *Insight* **2012**, *54*, 594-601.

134. Herdovics, B.; Cegla, F. Long-term stability of guided wave electromagnetic acoustic transducer systems. *Structural Health Monitoring* **2018**, *19*, 3-11, doi:10.1177/1475921718805733.

135. Cegla, F.B.; Herdovics, B. Guided wave testing. 2021.

136. Wang, Y.; Wu, X.; Sun, P.; Li, J. Enhancement of the excitation efficiency of a torsional wave PPM EMAT array for pipe inspection by optimizing the element number of the array based on 3-D FEM. *Sensors* **2015**, *15*, 3471-3490, doi:10.3390/s150203471.

137. Furusawa, A.; Miwa, A.; Morikawa, A.; Kojima, F. Ultrasonic Guided Wave Testing System using Electromagnetic Acoustic Transducers and the Application in Steel Pipes with Inner Corrosion. *Journal of the Japan Society of Applied Electromagnetics and Mechanics* **2015**, *23*, 350-355, doi:10.14243/jsaem.23.350.

138. Herdovics, B. Torsional guided wave EMAT for pipeline monitoring. Imperial College London, London, 2018.

139. Herdovics, B.; Cegla, F. Structural health monitoring using torsional guided wave electromagnetic acoustic transducers. *Structural Health Monitoring* **2016**, *17*, 24-38, doi:10.1177/1475921716682688.

140. Ledesma, V.; Baruch, E.P.; Demma, A.; Lowe, M.J.S. Guided wave testing of an immersed gas pipeline. *Materials Evaluation* **2009**, *67*, 102-115.

141. Dobson, J.; Cawley, P. Independent Component Analysis for Improved Defect Detection in Guided Wave Monitoring. *Proceedings of the IEEE* **2016**, *104*, 1620-1631, doi:10.1109/jproc.2015.2451218.

142. Heinlein, S.; Cawley, P.; Vogt, T.; Burch, S.F. Structural health monitoring of a pipe using permanently installed guided wave sensors. *Material Evaluation* **2018**, *76*, 1118-1126.

143. Demma, A.; Cawley, P.; Lowe, M.; Pavlakovic, B. The Effect of Bends on the Propagation of Guided Waves in Pipes. *Journal of Pressure Vessel Technology* **2005**, *127*, 328-335, doi:10.1115/1.1990211.

144. Simonetti, F.; Cawley, P. On the nature of shear horizontal wave propagation in elastic plates coated with viscoelastic materials. *Proceedings of the Royal Society: Mathematical Physical and Engineering Sciences* **2004**, *460*, 2197-2221, doi:10.1098/rspa.2004.1284.

145. Achenbach, J.D. Quantitative nondestructive evaluation. *International Journal of Solids and Structures* **2000**, *37*, 13-27, doi:10.1016/s0020-7683(99)00074-8.

146. Wooh, S.-C.; Wang, J. Nondestructive characterization of defects using a novel hybrid ultrasonic array sensor. *NDT & E International* **2002**, *35*, 155-163, doi:10.1016/s0963-8695(01)00038-x.

147. Kak, A.C.; Slaney, M. *Principles of Computerized Tomographic Imaging*; Society for Industrial and Applied Mathematics: 2001.

148. Stepinski, T. An Implementation of Synthetic Aperture Focusing Technique in Frequency Domain. *IEEE Transactions on Ultrasonics, Ferroelectrics, and Frequency Control* **2007**, *54*, 1399-1408, doi:10.1109/tuffc.2007.400.

149. Hunter, A.J.; Drinkwater, B.W.; Wilcox, P.D. The Wavenumber Algorithm for Full-Matrix Imaging Using an Ultrasonic Array. *IEEE Transactions on Ultrasonics, Ferroelectrics, and Frequency Control* **2008**, *55*, 2450-2462, doi:10.1109/Tuffc.952.

150. Merabet, L.; Robert, S.; Prada, C. 2-D and 3-D Reconstruction Algorithms in the Fourier Domain for Plane-Wave Imaging in Nondestructive Testing. *IEEE Transactions on Ultrasonics, Ferroelectrics, and Frequency Control* **2019**, *66*, 772-788, doi:10.1109/TUFFC.2019.2895995.

151. Lu, J.-Y. 2D and 3D high frame rate imaging with limited diffraction beams. *IEEE Transactions on Ultrasonics, Ferroelectrics and Frequency Control* **1997**, *44*, 839-856, doi:10.1109/58.655200.

152. Stolt, R.H. Migration by Fourier Transform. *Geophysics* **1978**, *43*, 23-48, doi:10.1190/1.1440826.

153. Garcia, D.; Le Tarnec, L.; Muth, S.; Montagnon, E.; Poree, J.; Cloutier, G. Stolt's f-k migration for plane wave ultrasound imaging. *IEEE Transactions on*

Ultrasonics, Ferroelectrics, and Frequency Control **2013**, *60*, 1853-1867, doi:10.1109/TUFFC.2013.2771.

154. Leonard, K.R.; Hinders, M.K. Guided wave helical ultrasonic tomography of pipes. *The Journal of the Acoustical Society of America* **2003**, *114*, 767-774, doi:10.1121/1.1593068.

155. Bushberg, J.T.; Seibert, J.A.; Leidholdt Jr, E.M.; Boone, J.M. *The Essential Physics of Medical Imaging*, 3 ed.; Wolters Kluwer; Lippincott Williams & Wilkins: London, 2012.

156. Carson, P.L.; Meyer, C.R.; Scherzinger, A.L.; Oughton, T.V. Breast imaging in coronal planes with simultaneous pulse echo and transmission ultrasound. *Science* **1981**, *214*, 1141-1143, doi:10.1126/science.7302585.

157. Devaney, A. A filtered backpropagation algorithm for diffraction tomography. *Ultrasonic Imaging* **1982**, *4*, 336-350, doi:10.1016/0161-7346(82)90017-7.

158. Devaney, A.J. A computer simulation study of diffraction tomography. *IEEE Transactions on Biomedical Engineering* **1983**, *30*, 377-386, doi:10.1109/tbme.1983.325037.

159. André, M.P.; Janée, H.S.; Martin, P.J.; Otto, G.P.; Spivey, B.A.; Palmer, D.A. High-speed data acquisition in a diffraction tomography system employing large-scale toroidal arrays. *International Journal of Imaging Systems and Technology* **1998**, *8*, 137-147, doi:10.1002/(sici)1098-1098(1997)8:1<137::Aid-ima15>3.0.Co;2-#.

160. Moratal, D.; Valles-Luch, A.; Marti-Bonmati, L.; Brummer, M. k-Space tutorial: an MRI educational tool for a better understanding of k-space.

Biomedical Imaging and Intervention Journal **2008**, *4*, e15, doi:10.2349/biij.4.1.e15.

161. Simonetti, F.; Huang, L. From beamforming to diffraction tomography. *Journal of Applied Physics* **2008**, *103*, doi:10.1063/1.2927433.

162. Wolf, E. Three-dimensional structure determination of semi-transparent objects from holographic data. *Optics Communications* **1969**, *1*, 153-156, doi:10.1016/0030-4018(69)90052-2.

163. Simonetti, F.; Huang, L. Synthetic aperture diffraction tomography for three-dimensional imaging. *Proceedings of the Royal Society A: Mathematical, Physical and Engineering Sciences* **2009**, *465*, 2877-2895, doi:10.1098/rspa.2009.0163.

164. Born, M. Quantenmechanik der Stoßvorgänge [On the quantum mechanics of collision processes]. *Zeitschrift für Physik* **1926**, *38*, 803-827, doi:10.1007/bf01397184.

165. Huthwaite, P.; Simonetti, F. High-resolution guided wave tomography. *Wave Motion* **2013**, *50*, 979-993, doi:10.1016/j.wavemoti.2013.04.004.

166. Tant, K.M.; Mulholland, A.J.; Gachagan, A. A model-based approach to crack sizing with ultrasonic arrays. *IEEE Transactions on Ultrasonics, Ferroelectrics, and Frequency Control* **2015**, *62*, 915-926, doi:10.1109/TUFFC.2014.006809.

167. Chen, B.; Stamnes, J.J. Validity of diffraction tomography based on the first born and the first rytov approximations. *Applied Optics* **1998**, *37*, 2996-3006, doi:10.1364/ao.37.002996.

168. Huthwaite, P. Evaluation of inversion approaches for guided wave thickness mapping. *Proceedings of the Royal Society A: Mathematical, Physical and Engineering Sciences* **2014**, *470*, doi:10.1098/rspa.2014.0063.

169. Mueller, R.K.; Kaveh, M.; Wade, G. Reconstructive Tomography and Applications to Ultrasonics. *P Ieee* **1979**, *67*, 567-587, doi:Doi 10.1109/Proc.1979.11284.

170. Jin, D.; Zhou, R.; Yaqoob, Z.; So, P.T.C. Tomographic phase microscopy: principles and applications in bioimaging [Invited]. *The Journal of the Optical Society of America* **2017**, *34*, B64-B77, doi:10.1364/josab.34.000b64.

171. Velichko, A.; Wilcox, P.D. Post-processing of Guided Wave Array Data for High Resolution Pipe Inspection. *The Journal of the Acoustical Society of America* **2009**, *126*, 2973-2982, doi:10.1121/1.3257604.

172. Perfetto, S.; Wilder, J.; Walther, D.B. Effects of Spatial Frequency Filtering Choices on the Perception of Filtered Images. *Vision (Basel)* **2020**, *4*, 29, doi:10.3390/vision4020029.

173. Hutton, D.V. *Fundamentals of Finite Element Analysis*; Mc Graw Hill: New York, 2004.

174. Alleyne, D.N.; Cawley, P. The interaction of Lamb waves with defects. *IEEE Transactions on Ultrasonics, Ferroelectrics, and Frequency Control* **1992**, *39*, 381-397, doi:10.1109/58.143172.

175. Koshiba, M.; Karakida, S.; Suzuki, M. Finite-Element Analysis of Lamb Wave Scattering in an Elastic Plate Waveguide. *IEEE Transactions on Sonics and Ultrasonics* **1984**, *31*, 18-24, doi:10.1109/t-su.1984.31456.

176. Koshiba, M.; Hasegawa, K.; Suzuki, M. Finite-element solution of horizontally polarized shear wave scattering in an elastic plate. *IEEE Transactions on Ultrasonics, Ferroelectrics, and Frequency Control* **1987**, *34*, 461-466, doi:10.1109/t-uffc.1987.26967.

177. Moser, F.; Jacobs, L.J.; Qu, J. Modeling elastic wave propagation in waveguides with the finite element method. *NDT & E International* **1999**, *32*, 225-234, doi:10.1016/s0963-8695(98)00045-0.

178. Diligent, O.; Lowe, M.J.S. Reflection of the s0 Lamb mode from a flat bottom circular hole. *The Journal of the Acoustical Society of America* **2005**, *118*, 2869-2879, doi:10.1121/1.2074947.

179. Zhuang, W.; Shah, A.H.; Datta, S.K. Axisymmetric Guided Wave Scattering by Cracks in Welded Steel Pipes. *Journal of Pressure Vessel Technology* **1997**, *119*, 401-406, doi:10.1115/1.2842322.

180. Zhu, W. An FEM Simulation for Guided Elastic Wave Generation and Reflection in Hollow Cylinders With Corrosion Defects. *Journal of Pressure Vessel Technology* **2002**, *124*, 108-117, doi:10.1115/1.1428331.

181. Belytschko, T.; Hughes, T.J.R., (Eds.) *Computational Methods for Transient Analysis*. North-Holland: Amsterdam, NL, 1983; Volume 1.

182. Cook, R.D.; Malkus, D., S.; Plesha, M.E.; Witt, R.J. *Concepts and Applications of Finite Element Analysis*, 4th ed.; John Wiley & Sons: 2001.

183. Bathe, K.-J. *Finite Element Procedures*; Prentice Hall: Upper Saddle River, NJ, 1996.

184. Drozdz, M.B. Efficient Finite Element Modelling of Ultrasound Waves in Elastic Media. Imperial College of Science, Technology and Medicine, London, 2008.

185. Lowe, M.J.; Diligent, O. Low-frequency reflection characteristics of the s0 lamb wave from a rectangular notch in a plate. *The Journal of the Acoustical Society of America* **2002**, *111*, 64-74, doi:10.1121/1.1424866.

186. Lowe, M.J.; Cawley, P.; Kao, J.Y.; Diligent, O. The low frequency reflection characteristics of the fundamental antisymmetric Lamb wave a0 from a rectangular notch in a plate. *The Journal of the Acoustical Society of America* **2002**, *112*, 2612-2622, doi:10.1121/1.1512702.

187. Huthwaite, P. Accelerated finite element elastodynamic simulations using the GPU. *Journal of Computational Physics* **2014**, *257*, 687–707, doi:10.1016/j.jcp.2013.10.017.

188. Pettit, J.R.; Walker, A.; Cawley, P.; Lowe, M.J.S. A Stiffness Reduction Method for Efficient Absorption of Waves at Boundaries for Use in Commercial Finite Element Codes. *Ultrasonics* **2014**, *54*, 1868-1879, doi:10.1016/j.ultras.2013.11.013.

189. Israeli, M.; Orszag, S.A. Approximation of radiation boundary conditions. *Journal of Computational Physics* **1981**, *41*, 115-135, doi:10.1016/0021-9991(81)90082-6.

190. Castaings, M.; Bacon, C.; Hosten, B.; Predoi, M.V. Finite element predictions for the dynamic response of thermo-viscoelastic material structures. *The Journal of the Acoustical Society of America* **2004**, *115*, 1125-1133, doi:10.1121/1.1639332.

191. Castaings, M.; Bacon, C. Finite element modeling of torsional wave modes along pipes with absorbing materials. *The Journal of the Acoustical Society of America* **2006**, *119*, 3741-3751, doi:10.1121/1.2197807.

192. Ke, W.; Castaings, M.; Bacon, C. 3D finite element simulations of an air-coupled ultrasonic NDT system. *NDT & E International* **2009**, *42*, 524-533, doi:10.1016/j.ndteint.2009.03.002.

193. Berenger, J.-P. A perfectly matched layer for the absorption of electromagnetic waves. *Journal of Computational Physics* **1994**, *114*, 185-200, doi:10.1006/jcph.1994.1159.

194. Hastings, F.D.; Schneider, J.B.; Broschat, S.L. Application of the perfectly matched layer (PML) absorbing boundary condition to elastic wave propagation. *The Journal of the Acoustical Society of America* **1996**, *100*, 3061-3069, doi:10.1121/1.417118.

195. Skelton, E.A.; Adams, S.D.M.; Craster, R.V. Guided elastic waves and perfectly matched layers. *Wave Motion* **2007**, *44*, 573-592, doi:10.1016/j.wavemoti.2007.03.001.

196. Chua, C.A.; Cawley, P.; Nagy, P.B. Scattering of the Fundamental Shear Guided Wave From a Surface-Breaking Crack in Plate-Like Structures. *IEEE Transactions on Ultrasonics, Ferroelectrics, and Frequency Control* **2019**, *66*, 1887-1897, doi:10.1109/TUFFC.2019.2932227.

197. Galvagni, A.; Cawley, P. The reflection of guided waves from simple supports in pipes. *J Acoust Soc Am* **2011**, *129*, 1869-1880, doi:10.1121/1.3543958.

198. Smith, R.A. Ultrasonic Defect Sizing in Carbon-Fiber Composites - an Initial Study. *Insight* **1994**, *36*, 595-605.

199. O'Donnell, M. Coded excitation system for improving the penetration of real-time phased-array imaging systems. *IEEE Transactions on Ultrasonics, Ferroelectrics, and Frequency Control* **1992**, *39*, 341-351, doi:10.1109/58.143168.

200. Chiao, R.Y.; Hao, X. Coded excitation for diagnostic ultrasound: a system developer's perspective. *IEEE Transactions on Ultrasonics, Ferroelectrics, and Frequency Control* **2005**, *52*, 160-170, doi:10.1109/tuffc.2005.1406543.

201. Isla, J.A.; Cegla, F.B. Simultaneous transmission and reception on all elements of an array: binary code excitation. *Proceedings of the Royal Society A: Mathematical, Physical, and Engineering Sciences* **2019**, *475*, 20180831, doi:10.1098/rspa.2018.0831.

202. Goodman, J.M., M. *Introduction to Fourier Optics*, 3 ed.; McGrawHill Book Co Ltd: 2004.

203. Fong, J.; Pialucha, T. Quantitative Short Range Guided Wave System. In Proceedings of the 15th Asia Pacific Conference for Non-Destructive Testing, Singapore, 2017.

204. Wooh, S.C.; Shi, Y.J. Three-dimensional beam directivity of phase-steered ultrasound. *Thr Journal of the Acoustical Society of America* **1999**, *105*, 3275-3282, doi:Doi 10.1121/1.424655.

205. Lee, J.H.; Choi, S.W. A parametric study of ultrasonic beam profiles for a linear phased array transducer. *IEEE Transactions on Ultrasonics, Ferroelectrics, and Frequency Control* **2000**, *47*, 644-650, doi:10.1109/58.842052.

206. Wooh, S.C.; Shi, Y.J. Optimum beam steering of linear phased arrays. *Wave Motion* **1999**, *29*, 245-265, doi:10.1016/S0165-2125(98)00039-0.

207. Isla, J.; Cegla, F. EMAT phased array: A feasibility study of surface crack detection. *Ultrasonics* **2017**, *78*, 1-9, doi:10.1016/j.ultras.2017.02.009.

This page intentionally left blank

List of Publications

[P1] Szlaszynski, F.; Lowe, M.J.S.; Huthwaite, P. Short Range Pipe Guided Wave Testing Using SH0 Plane Wave Imaging for Improved Quantification Accuracy. *Sensors* **2022**, *22*

[P2] Szlaszynski, F.; Lowe, M.J.S.; Huthwaite, P. Synthetic Focusing Imaging in Pipe Guided Wave Testing Using a Partial Circumferential Array for Inspection of Inaccessible Locations. *IEEE Transactions on Ultrasonics, Ferroelectrics, and Frequency Control* **2023**. [**Submitted - In Review**]